POLITECNICO
MILANO 1863

SCUOLA DI INGEGNERIA INDUSTRIALE
E DELL'INFORMAZIONE

Modelling of Ultrasound Enhanced Espresso Coffee Extraction Using Biot's Theory

TESI DI LAUREA MAGISTRALE IN
FOOD ENGINEERING

Authors: **Giovanni Correra, Davide Damiani**

Student ID: 10609665, 10667707
Advisor: Maurizio Masi
Co-advisor: Marco Marinsalta
Academic Year: 2025-2026

Abstract

Espresso coffee extraction is a solid–liquid mass transfer operation in a compacted granular bed whose yield is governed by the interplay of intraparticle diffusion, external film resistance, and convective transport driven by the Darcy flow. The decision to introduce ultrasound was taken with the objective of intensifying the process and improving extraction; however, the vast majority of the literature on the application of ultrasound to coffee is conducted in free-immersion or suspension configurations, geometries fundamentally different from the compacted pressurised bed of espresso extraction, leaving the behaviour of the system substantially uncharacterised from a modelling standpoint.

This thesis addresses these gaps by developing a mathematical model that couples acoustic propagation in a poroelastic medium with caffeine extraction kinetics in a compacted espresso bed. The acoustic field is computed by solving the Biot poroelastic equations for the coffee bed, coupled to the linear elastic equations for the AISI 304 steel basket, in COMSOL Multiphysics®; the divergence of the Reynolds stress tensor, derived from this field, is used as a volumetric body force in the Brinkman equations to compute the acoustic streaming velocity. The latter is superimposed on the axial Darcy flow and enters the external mass transfer coefficient of a one-dimensional convection–diffusion model for caffeine in a bimodal packed bed, solved in MATLAB®. Inertial cavitation is physically excluded on the basis of experimental evidence on bubble collapse dynamics near granular and porous boundaries. This shows that, at inter-particle void fractions typical of a compacted espresso coffee bed, collapse anisotropy is substantially attenuated relative to the rigid-wall case, indicating acoustic streaming as the only physically consistent enhancement mechanism in this geometry.

The extraction model is consistent with experimental caffeine kinetics reported in the literature, producing a cup concentration of 2.1 mg/ml and a total caffeine mass of 61.56 mg per standard espresso shot, both within the ranges reported for a well-executed espresso extraction, with a mass conservation error below 0.3%. A parametric study over basket thickness (0.4–0.7 mm) and applied acoustic power (50–200 W) in the frequency range 20–40 kHz demonstrates that streaming generation is governed by the spatial distribution of the acoustic velocity field as well as its magnitude, with the maximum caffeine extraction enhancement consistent with the physically motivated estimate of approximately 10% expected for this geometric configuration.

Key-words: espresso coffee extraction, ultrasonic intensification, poroelastic modelling, acoustic propagation in porous media.

Abstract in italiano

L'estrazione del caffè espresso è un'operazione di trasferimento di massa solido-liquido in un letto granulare compatto la cui resa è governata dall'interazione tra diffusione intraparticellare, resistenza del film esterno e trasporto convettivo indotto dal flusso di Darcy. La decisione di introdurre gli ultrasuoni è stata presa con l'obiettivo di intensificare il processo e migliorare l'estrazione; tuttavia, la grande maggioranza della letteratura riguardante l'applicazione di ultrasuoni al caffè è condotta in configurazioni a immersione libera o a sospensione, geometrie fondamentalmente diverse dal letto compatto in pressione dell'estrazione espresso, lasciando il comportamento del sistema sostanzialmente non caratterizzato dal punto di vista modellistico.

Questa tesi affronta queste lacune sviluppando un modello matematico che accoppia la propagazione acustica in un mezzo poroelastico con la cinetica di estrazione della caffeina in un letto espresso compatto. Il campo acustico è calcolato risolvendo le equazioni poroelastiche di Biot per il letto di caffè, accoppiate alle equazioni elastiche lineari per il cestello in acciaio AISI 304, in COMSOL Multiphysics®; la divergenza del tensore degli sforzi di Reynolds, derivata da questo campo, viene utilizzata come forza volumetrica nelle equazioni di Brinkman per calcolare la velocità di acoustic streaming. Quest'ultima si sovrappone al flusso assiale di Darcy ed entra nel coefficiente di trasferimento di massa esterno di un modello monodimensionale di convezione-diffusione della caffeina in un letto bimodale, risolto in MATLAB®. La cavitazione inerziale è fisicamente esclusa grazie alle evidenze sperimentali raccolte sulla dinamica di collasso in prossimità di bordi granulari e porosi. Questo dimostra che, per frazioni di vuoto interparticellare tipiche di un letto di caffè espresso compatto, l'anisotropia del collasso è sostanzialmente attenuata rispetto al caso di parete rigida, indicando l'acoustic streaming come unico meccanismo fisicamente possibile in questa geometria.

Il modello di estrazione è coerente con i valori riportati in letteratura dalle cinetiche sperimentali sulla caffeina, producendo una concentrazione nella tazza di 2.1 mg/ml e una massa totale di caffeina di 61.56 mg per singola dose di espresso da bar, entrambe all'interno degli intervalli riportati per un'estrazione di espresso ben eseguita, con un errore di conservazione della massa inferiore allo 0.3%. Uno studio parametrico su spessore del basket (0.4–0.7 mm) e potenza acustica applicata (50–200 W) nell'intervallo di frequenze 20–40 kHz dimostra che la generazione di streaming è

governata dalla distribuzione spaziale del campo di velocità acustica oltre che dalla sua ampiezza, con il massimo miglioramento dell'estrazione di caffeina coerente con la stima fisicamente motivata di circa il 10% attesa per questa configurazione geometrica.

Parole chiave: estrazione di caffè espresso, intensificazione ultrasonica, modellazione poroelastica, propagazione acustica in mezzi porosi.

Contents

Abstract ..... **i**

Abstract in italiano ..... **iii**

Contents ..... **v**

1. Introduction **9**

1.1. Coffee as a Subject of Scientific Inquiry 9

1.2. The Chemistry and Organoleptic Architecture of Coffee 11

1.3. Coffee Extraction as a Solid–Liquid Mass Transfer Operation 15

1.4. Key Variables Governing Extraction Performance 16

1.5. The Porous Structure of Roasted Coffee and its Role in Extraction 20

1.6. Mathematical Modelling of Coffee Extraction: State of the Approach 21

1.7. The Need to Intensify Coffee Extraction Processes 22

1.8. Ultrasound-assisted Extraction: Physical Principles 23

1.9. Ultrasound-Assisted Extraction Applied to Coffee: Literature Evidence 24

2 State of the Art **30**

2.1. Overview 30

2.2. Particle-Scale Structure: Pore Geometry, Transport Properties, and Dynamic Evolution 30

2.3. Governing Equations for Multi-Component Extraction in a Packed Coffee Bed 34

2.4. Fluid Dynamics in Packed Coffee Beds: The Darcy Framework and its Extensions 39

2.5. Ultrasound-Assisted Extraction: Mechanistic Depth and Quantitative Model 42

2.6. Ultrasound-Assisted Extraction of Coffee: A Critical Assessment of the Evidence 45

3 Research Objectives and Thesis Structure **49**

3.1. Identification of Research Gaps and Formulation of Objectives 49

3.2. Organisation of the Thesis 51

4 Theoretical Development 54
4.1. Process Description 54
4.2. System Setup 55
4.2.1. Basket Geometry and Configuration 55
4.2.2. Modelling Assumptions 56
4.2.3. Inertial Cavitation near Granular and Porous Boundaries 57
4.3. Model Subdivision 61
4.4. Initial Considerations 62
4.4.1. Reynolds Decomposition 62
4.4.2. Frequency Domain 63
4.4.3. Stress Tensor Definition 64
4.5. Porous Flow Model and Bed Properties 65
4.5.1. Brinkman Equations 65
4.5.2. Darcy Equation 66
4.5.3. Permeability and Tortuosity Coefficients 66
4.6. Extraction Model 67
4.6.1. Governing Equations 67
4.6.2. Mass Transfer Coefficients 69
4.6.3. Initial Conditions 70
4.6.4. Boundary Conditions 71
4.6.5. Cup Concentration 71
4.7. Ultrasound Model 71
4.7.1. Biot Poroelastic Theory 71
4.7.2. Acoustic Velocity 78
4.7.3. Solid Mechanics 78
4.7.4. Linear Elastic Material's Wave Speeds 78
4.7.5. Basket Boundary Conditions 79
4.8. Acoustic Streaming 80
4.8.1. Reynolds Stress Tensor Definition 80
4.8.2. Volumetric Force 2D Complex Derivation 81
4.8.3. Acoustic Streaming Flow 82
4.8.4. Boundary Condition 82
4.9. Model Closure 82
5 Model Parameters and Material Properties 84
5.1. Operative Parameters 84
5.2. Coffee Bed Properties 84

5.2.1. Drained Matrix Properties 84
5.2.2. Derivation of Bed Properties From PSD 85
5.2.3. Derivation of Roasted Coffee Poisson's Module 86
5.2.4. Coffee Properties from References 86
5.2.5. Coffee Properties from PSD 87
5.3. AISI 304 Steel Properties 89
5.4. Water Properties 89
5.5. Geometric Properties 90
6 Parametric Study and Numerical Approach 91
6.1. Extraction Model Numerical Solution 91
6.1.1. Equations Discretization 91
6.1.2. Error Evaluation 92
6.1.3. Meshing 93
6.1.4. Matlab® Code 93
6.1.5. PC Specs and Computing Time 93
6.2. Ultrasound Model Numerical Approach 94
6.2.1. Symmetry 94
6.2.2. Meshing Limits 95
6.2.3. Meshing 97
6.2.4. Solvers Configuration 98
6.2.5. PC Specs and Computing Time 99
7 Results and Discussion 100
7.1. Intermediate Results 100
7.2. Espresso Extraction 101
7.3. Parametric Ultrasonic Fields Study 104
7.3.1. Model validity based on wavelengths 104
7.3.2. Thickness Influence on Velocities 106
7.3.3. Laminar Flow Assumption Validity 110
7.3.4. Boundary Horn Power Influence on Velocities 110
7.4. Ultrasound-Assisted Extraction of Espresso Coffee 113
8 Conclusion and Future Developments 117
8.1. Conclusions 117
8.2. Future Developments 119
Bibliography 121
A Appendix A 130

B Appendix B 133
C Appendix C 134
List of symbols 139
8.3. Latin letters 139
8.4. Greek letters 142

1. Introduction

1.1. Coffee as a Subject of Scientific Inquiry

Coffee is one of the most widely consumed beverages on the planet, with a global production that exceeds 170 million 60-kg bags per year and consumption in the everyday routine of billions of people all over the world [1]. Its economic weight is also capital: coffee is one of the most traded agricultural products in the world, sustaining the lives of millions of smallholder farmers and hiding a really intricate international supply chain. Table 1.1 illustrates the trajectory of the global coffee economy, showing how fast production and trade value have grown over the past twenty years [2].

Table 1.1: Key indicators of the global coffee economy, 2000–2022/23 [2].

indicator	~2000	~2010	~2020	~2022/23
Global production (million 60-kg bags)	111	133	175	~178
Global consumption (million 60-kg bags)	~105	~130	~167	~177
Arabica share of production (%)	~66	~65	~57	~57-60

Export value (billion USD)	~5	~15	~22	~34
Countries producing coffee	>70	>70	>75	>75

Beyond its social and economic relevance, coffee is an exceptional subject of scientific study, a system in which a simple act, such as preparing a hot beverage, consists of a sequence of physical, chemical, and biological processes of enhanced sophistication.

Over the past two decades, the scientific literature has paid increasing attention to coffee not only as a consumer product but also as a model system for problems in process engineering, food science, and mass transport. Coffee is the perfect subject for studying the connection between physical and chemical phenomena: roasting deeply modifies the bean's microstructure, grinding defines the particle-size distribution, and the extraction stage translates these structural features into a final profile of dissolved compounds [3][4]. The reproducibility of each processing step strongly affects the quality of the brew, and ensuring such reproducibility is one of the most challenging aspects of coffee science in both household and manufacturing contexts [4].

Coffee fits perfectly into interdisciplinary studies. Its quality depends deeply on botanical and geographical origin, agronomic conditions, post-harvest treatments, roasting profile, and brewing technique [3]. The beverage that comes out at the end is not the product of a single processing stage but the outcome resulting from an entire chain of transformations. Given this information, the study of the extraction step cannot be conducted in isolation; it must be considered within a wider framework which includes the raw material's complexity and the system's sensitivity to operating parameters.

Looking at the global supply chain from a botanical perspective, it is possible to notice that coffee is dominated by two species: Coffea arabica (Arabica) and Coffea canephora (Robusta), which together cover more than 98% of world production [2]. Arabica beans, that are approximately the 57–60% of global production, are grown

at higher altitudes (900–2,000 m above sea level) and lead with a higher market price due to their in general more particular and delicate cup quality, while Robusta beans, cultivated at lower altitudes in more tropical climates, are much more hardier producing a harsher, more full-bodied and thick beverage with a characteristic woody or rubbery note [5]. The two species differ substantially in chemical composition, as will be discussed in detail in Subchapter 1.2, and these differences have a fundamental impact on extraction behaviour and beverage profile. The present thesis focuses on Arabica as the reference matrix, inherent with most of the mechanistic extractions present in literature, though the modelling framework developed is applicable and scalable to both species.

Coffee science has been the protagonist of several changes in recent years, moving from a mainly empirical, sensory-driven field toward an increasing integration of mathematical modelling and experimental measurement. Studies that integrate first-principles descriptions of flow and mass transfer with hands-on testing are now widely diffused in literature, allowing not only the understanding of existing brewing processes but also the rational design of new extraction setups and the application of unexplored intensification technologies [6]. The present thesis is firmly situated within this developing paradigm.

1.2. The Chemistry and Organoleptic Architecture of Coffee

To better understand coffee extraction, it is necessary to start by focusing on the chemical complexity of the substrate. Roasted coffee is among the most compositionally intricate matrices encountered in food science. Its chemical composition is the cumulative product of the genetic make-up of the plant, the growing environment, post-harvest processing, and — most consequentially — the roasting process, which triggers a dense network of thermally induced reactions which transform a biologically active green seed into a complex, porous, aromatic solid [3][7].

The principal chemical classes of interest in roasted coffee can be broadly organised according to their dominant sensory roles, their solubility profiles, and their known physiological activities. Table 1.2 summarises the main compound classes, their typical concentrations in roasted Arabica and Robusta coffee, their primary sensory contributions and biological activities, and their relative extraction rates.

Table 1.2: Principal chemical classes in roasted Arabica and Robusta coffee, with typical dry-weight concentrations, primary sensory roles and activities, and relative extraction rates [5][3][7][8][9][10][11][12].

Compound Class	Arabica (% d.w.)	Robusta (% d.w.)	Primary sensory contribution and activity	Relative extraction rate
Caffeine	1.0-1.7	1.7-3.5	Bitterness; central nervous system stimulant (adenosine receptor antagonist)	Fast (high water solubility)
Chlorogenic acids (CGAs)	1.0-4.0	3.0-7.0	Acidity, astringency; antioxidant, anti-inflammatory activity	Moderate (size-limited diffusion)
Trigonelline	0.6-1.0	0.3-7.0	Mild bitterness, sweetness; niacin (vitamin B3) precursor	Slow (high MW, strong matrix interaction)
Melanoidins	Up to 25	Up to 25	Colour, body, mouthfeel; antioxidant, antimicrobial, prebiotic activity	Slow (high MW, strong matrix interaction)
Organic acids	1.0-3.0	0.5-2.0	Perceived acidity, brightness; modulate overall flavour balance	Moderate to fast
Diterpenes (cafestol, kahweol)	0.5-1.5	~0.2	Body, richness; raise LDL cholesterol (cardiovascular risk at high intake from	Slow (lipophilic;

			unfiltered brews); kahweol shows chemopreventive activity in vitro	filtration-dependent)
Volatile aroma compounds	trace–1.0	trace–1.0	Aroma complexity (roasted, fruity, floral, smoky); primary sensory quality determinant	Fast release; susceptible to evaporative loss

Caffeine (1,3,7-trimethylxanthine) is the most significant alkaloid component of coffee and one of the most accessible to analyse. It is present in concentrations of 1.0–1.7% by dry weight in Arabica and 1.7–3.5% in Robusta. Caffeine contributes to the sensory profile with its characteristic bitter flavour and plays a well-documented role as a central nervous system stimulant through competitive antagonism at adenosine receptors [3][8]. Chemically, caffeine is a methylxanthine, a compound characterised by a high water solubility over a wide temperature range. This makes caffeine one of the most readily extracted components of the coffee matrix; it is often used as a reference compound for estimating overall extraction efficiency [8].

Chlorogenic acids (CGAs) form the largest group of polyphenolic compounds in coffee and are among the most relevant in nutritional terms. Green Arabica beans contain between 5% and 10% CGAs by dry weight, but a relevant fraction is degraded during roasting via hydrolysis, isomerisation, and Maillard-type reactions. These processes leave a residual content of roughly 1–4% in the roasted product, depending on the degree of roast [7][9]. Green Robusta beans retain especially higher CGA concentrations (7–12% d.w.) [5]. The most significant species are 5-caffeoylquinic acid (5-CQA), 3-CQA, and 4-CQA, along with di-caffeoylquinic and feruloylquinic acid isomers. CGAs are responsible for the perceived acidity in coffee; this is caused by the progression of hydrolysis during extraction, which releases caffeic and quinic acids, modifying coffee's sensory profile. CGAs also have potent antioxidant powers with documented anti-inflammatory activity [9].

Trigonelline (N-methyl nicotinic acid) is a quaternary alkaloid present at 0.6–1.0% in green Arabica and 0.3–0.7% in Robusta. During roasting, a considerable fraction is demethylated to niacin (vitamin B3), while the rest participates in Maillard-type

reactions, forming pyridine and pyrrole aroma compounds [3][7]. The residual concentration in the cup has the function of a chemical marker to better assess roast intensity.

Melanoidins are brown polymers, containing nitrogen and characterised by a high molecular weight. They are produced during roasting through the Maillard reaction, a thermally driven, non-enzymatic browning process between reducing sugars and amino acids that consists of multiple intermediate stages, including the formation of Amadori rearrangement products, Strecker degradation compounds, and, ultimately, highly condensed, cross-linked macromolecular structures [13]. Alongside the Maillard reaction, caramelisation — the thermal degradation and recombination of sugars in the absence of amino acids — concedes additional colour and flavour compounds, including furans, diacetyl, and various furanones with caramel and buttery-sensory descriptors [14]. Melanoidins characterise the 25% of the dry weight of the roasted bean and are mainly responsible for its characteristic brown colour. Their extraction yield has a greater extension in terms of diffusion than that of small molecules, and they contribute to body and mouthfeel while providing antioxidant, antimicrobial, and prebiotic activities [7][9].

Organic acids — including caffeic acid, quinic acid, citric acid, malic acid, acetic acid, formic acid, and lactic acid — are the main contributors to the perceived acidity of the cup. Their relative proportions in the final product depend on roast degree and bean origin [10]. Lighter roasts preserve more organic acids, having brighter, fruitier profiles, while darker roasts shift the balance, obtaining heavier, more bitter notes.

Lipids, like diterpenes (cafestol and kahweol) and chlorogenic acid esters of fatty acids, represent 10–18% of the green bean dry weight in Arabica and a little bit lower in Robusta (approximately 7–10% d.w.) [3][5]. Their partitioning into the brew depends mostly on filtration conditions. The diterpenes cafestol and kahweol raise LDL cholesterol at high intakes from unfiltered preparations by inhibiting cytochrome P450 enzymes; kahweol also reveals chemopreventive activity in vitro models [3].

The volatile fraction of roasted coffee includes over 1,000 chemical compounds, like pyrazines, furans, pyrroles, thiophenes, ketones, aldehydes, phenols, and terpenes [11][15]. Their formation is the net result of Maillard reactions and Strecker degradation pathways, caramelisation, lipid oxidation, and thermal pyrolysis of amino acids during roasting [13][14]. Lighter roasts are mainly characterised by fruity and floral notes from aldehydes and esters, while darker roasts show increasing contributions from pyrazines and furans [11][15].

Every interaction between these chemical classes is important: many of the sensory qualities of coffee come from synergistic or antagonistic relationships between compound families. For example, the bitter taste of coffee is not only a function of caffeine concentration but also of compounds such as CGAs, melanoidins, diketopiperazines, and oxidised phenols, which contribute in ways that depend on their relative concentrations and individual consumers' taste physiology [12]. For a better understanding and optimisation of coffee extraction, it is fundamental to consider the system's multi-component nature and the interdependence of extraction yields across compound classes.

1.3. Coffee Extraction as a Solid–Liquid Mass Transfer Operation

From an engineering perspective, coffee extraction can be described as a solid–liquid operation in which water serves as a selective solvent for the solid matrix. The coffee matrix is not an inert, homogeneous solid; on the contrary, it has a porous, geometrically complex configuration whose characteristics, such as structural and transport properties, develop during the process [4][6].

The phenomenological process starts with the imbibition of particles by the advancing solvent front. Water penetrates the interparticle void space and enters the intraparticle pore network. It is a process managed via the interaction among capillary forces, the applied pressure driving convective flow through the bed, and the porosity architecture of the roasted coffee particle [4][6].

When the solvent contacts the solid matrix at the pore wall level, dissolution and desorption of soluble species begin. The transport phenomenon that carries dissolved compounds from the inner section of the particle toward its outer surface is controlled by intraparticle diffusion. It depends on the molecular diffusivity of the species in the aqueous phase, the effective diffusivity inside the particle (reduced relative to free-solution diffusivity by the tortuosity and constrictivity of the pore network), and the local concentration gradient[4]. It depends on the molecular diffusivity of the species in the aqueous phase, the local concentration gradient and the effective diffusivity inside the particle. This last effect reflects the reduction, compared to free-solution diffusivity, due to the tortuosity and constrictivity of the pore network, a factor that account for the constriction of the pore diameter relative to the solute dimension, representing an additional resistance to the particle that diffuses in a tighter pore than its diameter [4].

For large, polar molecules such as melanoidins, intraparticle diffusion is rate-limiting; whereas for smaller species such as caffeine, the resistance of the external liquid film becomes equally important. For large, polar molecules such as melanoidins, intraparticle diffusion is rate-limiting; whereas for smaller species, such as caffeine, the resistance of the external liquid film becomes equally important. Mass transfer in the liquid film surrounding each particle is governed by convection and molecular diffusion. In coffee brewing configurations, advective transport in the inter-particle space dominates over diffusion as the principal mechanism for compound transport along the bed length [16]; while the external film resistance, secondary to intraparticle resistance for slowly diffusing species, is non-negligible for rapidly extracted compounds such as caffeine, whose intraparticle diffusion path is short [4].

The dissolved compounds are then moved through the inter-particle void space by a combination of advection (driven by the net pressure gradient) and axial dispersion. In other words, real coffee beds show considerable heterogeneity, characterised by variations in particle size, packing density, and preferential flow channels, each of which contributes to non-uniform extraction [6].

The resulting extraction kinetics derive from an intricate relation involving different transport resistances: intraparticle diffusion, interfacial transfer, and bed-level convection and dispersion. The particular operating conditions of the process, such as the physical properties of the desired compound and the morphological characterisation of the coffee particles, modify the rate-controlling step. This divergence in controlling mechanisms explains why multi-scale, physically motivated descriptions are fundamental to punctual prediction.

1.4. Key Variables Governing Extraction Performance

The extraction performance of a coffee brewing system is exposed to a wide set of operational and physicochemical variables. Table 1.3 summarises the principal variables, their mechanistic effects on extraction kinetics and yield, and their effects on beverage quality.

Table 1.3: Principal process variables in coffee extraction [1][6][10].

Variable	Effect on extraction kinetics and yield	Effect on beverage quality
Water temperature (Arabica: 90–96°C; Robusta: 88–93°C)	↑ solubility, ↑ diffusivity, ↓ viscosity → faster extraction	Risk of over-extraction, aroma loss at high T
Particle size	↓ size → ↑ surface area, ↓ diffusion path, ↓ bed permeability	Finer grind → higher extraction but risk of channelling
Liquid-to-solid ratio (espresso 1:2–1:3; filter 1:15–1:17; cold brew 1:10–1:12)	↑ ratio → sustained concentration gradient → ↑ extraction yield, ↓ TDS	Determines brew strength and body
Contact time	Longer → more slow-extracting species mobilised	Sets balance of early vs. late extracting compounds
Water consumption	Ca^{2+}/Mg^{2+} influence CGA complexation and extraction rate	Hardness affects taste, mouthfeel, mineral balance

Water temperature is one of the most important variables, and its effects are visible on multiple fronts at the same time. It defines the equilibrium solubility of dissolved species, the diffusivity of the species present in the aqueous phase (which varies roughly with absolute temperature according to the Stokes–Einstein relation), the viscosity of the solvent (which decreases with increasing temperature, lowering flow resistance), and the kinetics of thermally activated release reactions at the solid surface [1][10]. It defines the equilibrium solubility of dissolved species, the diffusivity of the species present in the aqueous phase (which varies roughly with absolute temperature according to the Stokes–Einstein relation [16]), the viscosity of the solvent (which decreases with increasing temperature, lowering flow resistance), and the kinetics of thermally activated release reactions at the solid surface [1][10]. Higher temperatures usually accelerate extraction and increase total dissolved solids yield, but in this case, they can further improve the extraction of compounds, coupled with harsh, over-extracted notes, and cause losses of thermally sensitive volatile aroma compounds.

Particle size distribution is the key variable responsible for the extraction performance through different coupled mechanisms. One of them is that reducing the mean particle diameter increases the specific surface area available for solvent contact and shortens the characteristic intraparticle diffusion length. However, at the same time, a finer grind reduces the permeability of the packed bed, raising the pressure drop and decreasing the flow rate, which in turn extends the contact time between water and coffee grounds and generates a greater proportion of very fine particles through attrition mechanisms during grinding [17]. Figure 1.1 shows how the most commercial and domestic grinding devices produce a broad, approximately bimodal distribution consisting of a coarse primary fraction and a population of sub-100-micrometre fines [17].

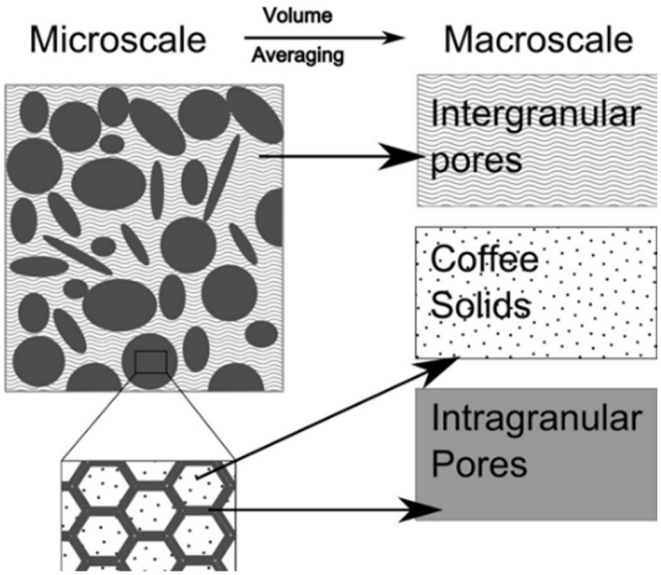

Figure 1.1 — Schematic representation of the two spatial scales of the coffee extraction problem. At the microscale (left), roasted coffee particles contain inter-particle pores (wavy lines) and intra-granular pores (dots in the zoom inset). Volume averaging yields the macroscale continuum description (right) with three homogenised phases: intergranular pores, coffee solids, and intragranular pores [4].

Fine particles, with their short diffusion paths and high surface-to-volume ratio, reach near-complete extraction within the first seconds of contact with the solvent and preferentially release early-extracting compounds — caffeine, trigonelline, and the more soluble organic acids — at concentrations substantially higher than the bed-average value. Coarser particles could instead remain partially unextracted throughout the brewing cycle. The result is a beverage that contains both over-extracted compounds from fines (increased bitterness and harshness) and under-extracted compounds from coarse fragments (flat, cereal-like notes) [6][17]. This heterogeneity is obtained by the habit of fines to segregate inside the bed and create zones of high resistance, inducing preferential flow channelling around them and further lowering effective contact between solvent and coarse particles [6].

The liquid-to-solid ratio is an essential element of the mass transfer driving force, thanks to its effect on the liquid-phase concentration. A high ratio leads to a larger concentration gradient and facilitates continued extraction, whereas a low ratio is more likely to reach saturation earlier, reducing the driving force.

Contact time determines how far the extraction proceeds along the kinetic trajectory of every compound class: because different compound families exhibit different

extraction rates, contact time precisely determines the relative proportions of extracted species and the beverage's sensory balance [1].

Another parameter that can influence the extraction performance is the chemical composition of the water used for the operations. Water hardness, characterised by the concentrations of calcium and magnesium ions, influences the extraction of chlorogenic acids and other polar compounds through ion-exchange and complexation mechanisms, impacting taste and mouthfeel through strong interactions with taste-active compounds [10].

1.5. The Porous Structure of Roasted Coffee and its Role in Extraction

The roasted coffee particle is a structurally intricate porous material whose architecture is central to determining extraction kinetics. During roasting, the thermal decomposition of carbohydrates and proteins generates large amounts of CO_2 and water vapour that expand within the bean cell structure, creating an interconnected network of macropores superimposed on the pre-existing cell wall microporosity. The final pore design is structured in several length scales: macro-pores of tens to hundreds of micrometres arising from cellular disruption, micropores of tens to hundreds of nanometres within the cell wall material, and a continuum of pore sizes in between [7][18].

This stratified pore structure has several important consequences for extraction. The effective diffusivity of solutes within the particle is substantially lower than their diffusivity in free aqueous solution, due to the tortuosity of the diffusion pathway and the constrictivity of the narrower pore channels. Experimental estimations from packed-bed extraction data set the ratio D_{eff}/D in the range of 0.01–0.1 for roasted coffee particles [4][18].

An additional complication results from the active evolution of the pore structure during extraction. As soluble compounds are progressively leached from the solid matrix, the effective porosity of the particle increases in a process that has been quantified by tracking the residual mass and swelling behaviour of coffee particles at successive extraction stages [18]. This increase in porosity alters both the intraparticle diffusivity and the mechanical stiffness of the particle. Furthermore, the swelling of coffee particles upon contact with water, going from the hydration and plasticisation of the polysaccharide and protein network, as documented by time-resolved micro-CT experiments [19], modifies the inter-particle packing geometry and can lead to effective changes in bed permeability during extraction.

These progressive structural changes motivate the presence of time-varying transport parameters in physically extended extraction models.

The characterisation of the pore structure has been advanced by several complementary experimental techniques. Mercury intrusion porosimetry and nitrogen gas uptake yield pore size distributions averaged over large granule populations. X-ray micro-computed tomography (micro-CT) allows non-destructive three-dimensional imaging of the pore network at the single-particle level [19]. Scanning electron microscopy has provided qualitative evidence of cell wall disruption and pore enlargement after consecutive extraction steps [18]. These studies prove that the structural heterogeneity of the coffee particle, both within individual particles and between particles of different sizes, is a dominant source of variability in extraction performance.

1.6. Mathematical Modelling of Coffee Extraction: State of the Approach

The complexity of coffee extraction has motivated the development of mathematical models spanning a wide range in sophistication, from simple first-order kinetic models to totally resolved, multi-scale computational structures. The evolution of this modelling literature highlights the growth in availability of computing resources and the expansion of an acknowledgement that empirical, curve-fitting approaches are insufficient to capture the mechanistic richness of the process.

The earliest quantitative descriptions utilised lumped-parameter kinetics, typically characterising the rate of compound release from the solid phase by fitting a single differential equation to experimental concentration–time data [41]. These models can describe the main features of extraction kinetics considering a fixed set of conditions, but they lack predictive power over different operating parameters and cannot distinguish among the contributions of intraparticle diffusion, interfacial transfer, and bed-level transport. An important improvement was achieved with the introduction of the ‘rapid and slow’ extraction framework, in which the total extractable mass is divided into a rapidly extracting surface fraction and a slowly extracting interior fraction. This dual-component model punctually represents the characteristic biphasic shape of experimental extraction kinetics and guarantees a more physically interpretable parameterisation, while remaining a lumped description that does not explicitly resolve spatial concentration gradients [4].

The multi-scale modelling approach pioneered by Moroney Et al. [4] represents the current state of the art in mechanistic coffee extraction modelling. In this scheme,

the bed is treated as a one-dimensional porous continuum through which water flows under an applied pressure gradient, while the extraction kinetics at the particle level are described by combined differential equations for the solid-phase and liquid-phase concentrations. This structure, mathematically equivalent to models of fixed-bed adsorbers and chromatographic columns, enables the independent identification of transport parameters from experimental data, rather than global lumped fitting.

More recently, fully three-dimensional computational flow dynamics simulations resolving the inter-particle flow geometry at the pore scale have been applied to study the flow field inside the coffee bed and its influence on extraction uniformity, revealing the importance of flow channelling and preferential pathways [6]. These in-depth simulations are computationally heavy and not suitable for daily process design, but they provide essential mechanistic insight that informs the production about lower-dimensional models.

1.7. The Need to Intensify Coffee Extraction Processes

Despite decades of empirical advances and, more recently, scientific investigation, conventional coffee extraction processes still have essential limitations that motivate the search for intensification strategies.

From a yield standpoint, conventional brewing processes do not extract the full quantity of soluble compounds present in the coffee matrix. The degree of extraction, defined as the fraction of the total soluble mass transferred from the ground coffee to the beverage, is usually kept between 18% and 22% in well-executed conventional brewing [54]. Below this range, the beverage is characterised by flatness, sourness, and an incomplete flavour profile linked with under-extraction; above it, the progressive mobilisation of slower-extracting species — particularly high-molecular-weight melanoidin fragments, diketopiperazines, and bitter quinides from chlorogenic acid degradation — degrades cup quality, enhancing excessive bitterness, astringency, and a dry, hollow aftertaste [1]. A suitable practical prospect could be intensification methods that increase compound production while remaining within the acceptable extraction window, or those that use a more precise control to preferentially extract compound classes.

The selectivity of conventional extraction is also limited because temperature, pressure, and contact time act on all compound classes at the same time. This makes it harder to tune the extraction yields of different compound families one by one. A technique able to selectively improve mass transfer or accelerate extraction without requiring more aggressive process conditions would represent a significant advancement. Reproducibility is a further challenge. Process intensification

technologies that stabilise the extraction dynamics or reduce sensitivity to slight disturbances in operating conditions would be worthwhile.

Luckily, there is growing interest in the valorisation of the full chemical potential of the coffee matrix for the recovery of bioactive compounds (polyphenols, diterpenes, melanoidins) for nutritional and functional food applications. Intensification technologies that improve recovery from the solid matrix are of direct practical interest [20][21].

1.8. Ultrasound-assisted Extraction: Physical Principles

Ultrasound-assisted extraction (UAE) has emerged over the past two decades as one of the most promising process intensification technologies for solid–liquid extraction in the food and pharmaceutical sectors. The term 'ultrasound' refers to mechanical pressure waves transmitting at frequencies above the upper limit of human audibility (20 kHz), with the frequencies most relevant to food processing generally falling in the range of 20–100 kHz [20][21]. At these relatively low frequencies and at the power densities used in extraction applications, the dominant physical mechanism is acoustic cavitation.

Acoustic cavitation is the nucleation, growth, and probably violent collapse of microscopic gas-filled bubbles in a liquid phase, driven by the alternating pressure cycles of the ultrasonic wave. During the rarefaction phase, dissolved gas and vapour accumulate in pre-existing nucleation sites, forcing the bubbles to grow. During the successive compression phase, if the acoustic pressure amplitude is greater than a critical threshold, the bubble collapse is inertial and extremely rapid. The implosion causes highly localised events of extreme temperature (measured in thousands of Kelvins within the bubble), extreme pressure (hundreds of megapascals), and high-velocity microjets directed toward adjacent solid surfaces [20]. These conditions, though restricted to a microscopic volume, can have dramatic effects on the surrounding solid–liquid system.

In this kind of configuration, ultrasonic irradiation increases mass transfer through two physically different mechanisms that, although often co-occurring, differ systematically in their origins and ways of action. The first is acoustic streaming, a steady, pressure-driven bulk flow provoked by the nonlinear attenuation of the acoustic wave in the fluid, which produces macroscale convective currents that improve bulk mixing and reduce concentration gradients throughout the extraction vessel; this phenomenon is treated in detail in Chapter 4. Then the second one is acoustic cavitation, whose consequences for mass transfer are the following. First, the liquid microjets generated by bubble collapse near solid surfaces create intense

local shear and turbulence, extremely improving the external mass transfer coefficient by disrupting the stagnant boundary layer at the solid–liquid interface. Second, mechanical energy delivered to solid particles can cause surface erosion, fragmentation, and pore enlargement. These effects expand the available surface area and reduce the practical diffusion path length, favouring intraparticle mass transfer [20][21]. Third, cavitation phenomena, by disrupting cell walls and membrane structures, would release intracellular compounds that otherwise would be inaccessible to the solvent on the timescale of conventional extraction. These mechanisms have been predominantly characterised in the context of solid particles freely suspended in a large, unconstrained aqueous volume, a configuration that differs radically from the compacted packed-bed geometry of espresso extraction, as will be shown in Chapter 4.

The resultant effect of this system is a considerable increase in both external and internal mass transfer coefficients, obtaining faster extraction kinetics and, depending on the system, better ultimate extraction yields. The quantitative magnitude of these increases depends on ultrasonic frequency, acoustic power density, reactor geometry, and the construction traits of the solid matrix [20][21].

UAE, differently by intensification strategies, can be performed at or near ambient temperature, avoiding the thermal degradation of heat-sensitive compounds. This quality is specifically advantageous when objective compounds contain thermally labile volatiles or bioactive species [20].

1.9. Ultrasound-Assisted Extraction Applied to Coffee: Literature Evidence

The application of ultrasound to coffee extraction has attracted increasing research attention in recent years. Growing experimental evidence indicates that acoustic assistance leads to measurable improvements in extraction efficiency across different compound categories.

Cold brew coffee is obtained by immersing ground coffee in cold water (typically 4–20°C) at a coffee-water ratio of about 1:10–1:12 by mass, allowing extraction for 12–24 hours without applied pressure. In this setup, ultrasound treatment reduces the conventional preparation time to 30–90 minutes while maintaining or improving the concentrations of fundamental compounds [22][23]. Detailed physicochemical analyses have shown yield increments for caffeine of up to 54.7%, for chlorogenic acids of up to 67.4%, and for trigonelline of up to 26.8% relative to non-sonicated configuration under optimised conditions [24]. These values, however, regard a dilute immersion geometry (coffee-water ratio 1:10–1:12) and should not be compared directly to espresso-style extraction, which operates at a

ratio of 1:2–1:3 under 9 bar of applied pressure over a contact time of 25–30 seconds, using forced convective flow through a compacted packed bed.

Studies on standard hot water coffee extraction have also demonstrated beneficial effects. Under a factorial experimental design varying coffee concentration, temperature, and sonication time, increases in the extraction of caffeine, triglycerides, and various key volatile aroma compounds were documented relative to conventional brewing controls [25]. The observation of contemporary improvement across chemically diverse compound classes — from small, polar alkaloids to larger lipophilic triglycerides to highly volatile aroma species — suggests that acoustic energy acts especially on the mass transfer resistance of the system, compatible with the cavity-driven enhancement of both external and intraparticle transport.

The mechanistic basis for the acoustic enhancement of caffeine extraction from Arabica beans has been directly investigated by Huamaní-Meléndez & Darros-Barbosa [26], who mapped D_{eff} as a joint function of temperature and ultrasonic intensity (Figure 1.2), characterising through response surface methodology how ultrasonic intensity and temperature jointly affect caffeine recovery and effective intraparticle diffusivity. Effective caffeine diffusion coefficients in the range of 8.9–10.6 × 10^{-11} m^2 s^{-1} were measured under optimal sonication conditions. These values, showing a magnitude of two orders above those of conventional cold brew extraction at comparable temperatures, stay two orders of magnitude below the free-solution diffusivity of caffeine at 90 °C (D = 2.6 × 10^{-9} m^2 s^{-1}), underlining that the improved values reported in [26] correspond uniquely to cold brew, low-temperature systems where diffusion is strongly reduced. These findings demonstrate unambiguously that acoustic cavitation increases mass transport within the coffee particle itself, not merely in the bulk liquid phase.

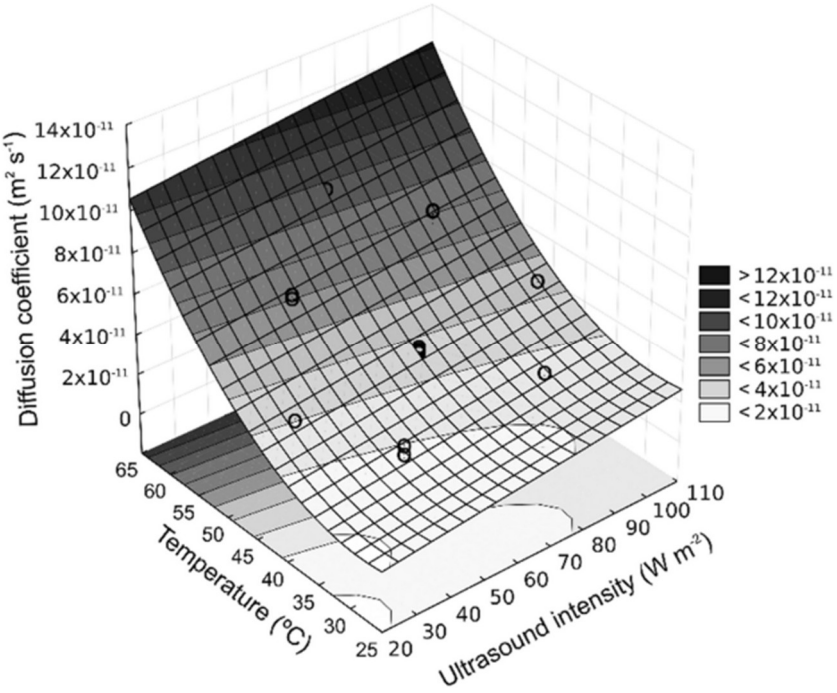

Figure 1.2: Effective caffeine diffusion coefficient D_{eff} ($m^2\ s^{-1}$) as a function of temperature (°C) and ultrasonic intensity ($W\ m^{-2}$) in roasted coffee under UAE conditions. D_{eff} increases monotonically with both temperature and acoustic intensity, reaching a maximum of ~$10.6 \times 10^{-11}\ m^2\ s^{-1}$ under optimal sonication. These values correspond to cold brew conditions (25–65°C) and cannot be extrapolated to espresso temperatures [26].

In Table 1.4 are reported the compound yield improvements found in the literature for key coffee compounds under UAE conditions, relative to conventional non-sonicated controls. It's important to underline that all studies were conducted in cold brew immersion (ratio 1:10–1:12) or suspension configurations; only one study — Chiu et al. [23] — has applied UAE to a packed-bed-like cold brew configuration, providing the closest available analogue to espresso-style extraction and serving as the primary experimental benchmark for the present work.

Table 1.4: Reported compound yield improvements under ultrasound-assisted extraction conditions, relative to conventional extraction controls [23][24][25][26][27].

Target compound	Yield increase (%)	Conditions	Reference
Caffeine	+54,7	Cold brew, 90% amplitude, 15 min, 20 °C	Lee & Lee (2025) [24]
Chlorogenic acids	+67,4	Cold brew, 90% amplitude, 15 min, 20 °C	Kim et al. (2024) [24]
Trigonelline	+26.8	Cold brew, 90% amplitude, 15 min, 20 °C	Kim et al. (2024) [24]
Caffeine + triglycerides + volatiles	Significant	Hot brew, factorial design	Zamanipoor et al. (2020) [25]
Caffeine (intraparticle diffusivity)	1-2 orders of magnitude in D_{eff}	Aqueous extraction, Arabica beans	Huamaí-Meléndez & Darros-Barbosa (2018) [26]

Polyphenols (spent grounds)	~+33	UAE vs. conventional, reduced energy	Beaudor et al. (2023) [27]
Overall extraction yield	+122% (15.1% → 33.4%)	Packed-bed sonoreactor, 100 W, 3 min, cold brew (BLP = 33%)	Chiu et al. (2024) [23]
Caffeine concentration	+103% (0.91 → 1.84 mg/mL)	Packed-bed sonoreactor, 100 W, cold brew (BLP = 67%)	Chiu et al. (2024) [23]

Despite this accumulating experimental record, the mechanistic understanding of ultrasound-assisted coffee extraction remains substantially incomplete. The literature experimental work is conducted almost entirely in free-suspension or batch-immersion configurations, systems in which the solid is dispersed in a large, unconstrained aqueous volume, conditions that are very divergent from the compacted packed-bed geometry of espresso extraction. In these designs, acoustic energy propagates through a free liquid phase, bubble nucleation occurs without geometric constraint, and the acoustic field distribution bears no resemblance to that in a compacted granular bed, where pore geometry, permeability, and acoustic impedance all impact wave propagation and attenuation. None of the existing studies uses the acoustic streaming velocity, the cavitation probability, or the effective intraparticle diffusivity improvement as functions of bed packing density or permeability, which are the exact quantities needed to extend the experimental findings to a packed-bed model. The single partial exception in the literature, and the study most directly relevant to the present thesis, is that of Chiu et al. [23]. Rather than using a free-suspension bath, Chiu et al. designed a packed-bed system where ground Arabica coffee is compacted inside a cylindrical cartridge, and water

is forced through under pressure while sonication is applied to the basket wall. They systematically varied the basket loading percentage (BLP), defined as the mass of coffee loaded relative to the filtering basket's maximum capacity. At BLP = 33% and 100 W of acoustic power, the total extraction efficiency grew from 15.1% to 33.4% (+122% compared to the non-sonicated cold-brew control), while the brewing time decreased from 24 hours to less than 3 minutes. Caffeine concentration at BLP = 67% doubled from 0.91 to 1.84 mg/mL (+103%).

The Chiu et al. study constitutes the most mechanistically relevant benchmark in the existing UAE coffee literature for the modelling framework developed here, and its experimental dataset acts as a key reference against which the present model can be compared.

2 State of the Art

2.1. Overview

This chapter builds a critical review of the scientific literature describing the present thesis along four main axes: the physicochemical and structural characterisation of the roasted coffee particle and its features for extraction transport; the mathematical description of the governing equations and interacting relationships in coffee extraction models; the fluid dynamics of flow through packed coffee beds; and the mechanistic basis and documented performance of ultrasound-assisted extraction in coffee and related systems. The treatment goes beyond the introductory survey provided in Chapter 1 to engage with the quantitative specifics of each area — equations, parameter values, experimental methods, and modelling choices — that directly inform the development of the model presented in subsequent chapters.

2.2. Particle-Scale Structure: Pore Geometry, Transport Properties, and Dynamic Evolution

The roasted coffee particle is a structurally complex, hierarchically porous solid whose internal architecture reflects the superposition of three distinct structural processes. The first is the pre-existing cellular organisation of the green coffee bean, which consists of thick-walled parenchyma cells from approximately 14 to 25 μm surrounded by intercellular spaces [19]. The second is the modification of this cellular architecture induced by roasting: as the bean temperature rises during roasting, thermally generated CO_2 and water vapour pressurise the cell lumen, causing continuous expansion of individual cells, rupture of cell walls at crack points, and the coalescence of adjacent cells into connected macro-pore channels. The third process, relevant primarily to grinding, is the mechanical fracture of the roasted cellular matrix along planes of weakness, which exposes interior surfaces and creates a population of fine particles rich in broken-cell material that is immediately accessible to the solvent [18].

The quantitative evolution of bean porosity during roasting has been characterised in several dedicated case studies using X-ray micro-computed tomography (micro-CT). Al-Shemmeri et al. [29] tracked individual Kenyan Arabica beans through

sequential roasting stages in a pilot-scale spouted bed roaster, achieving a spatial resolution of 3.65 μm per voxel. Their micro-CT reconstructions demonstrated that total porosity increased by up to 60% from green bean to the fully roasted state. Consistent with this, as shown in Figure 2.1, Pittia et al. [28] — using synchrotron X-ray microtomography on Arabica beans — quantified intraparticle porosity as increasing from approximately 4% in the green bean to approximately 40% in the fully roasted grain.

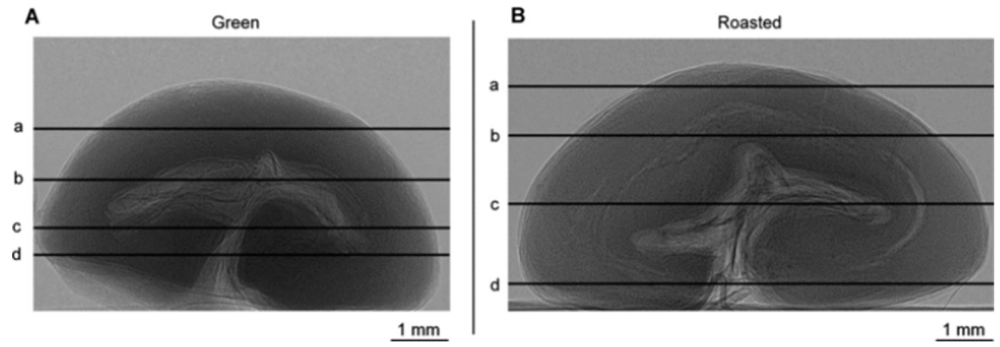

Figure 2.1: Synchrotron X-ray microtomography cross-sections of a single Arabica coffee bean in the green (A) and roasted (B) states. The macropore network expands dramatically during roasting: total porosity increases from ~4% in the green bean to ~35–40% in the roasted bean as CO_2 released during pyrolysis inflates the cellular structure. Scale bar: 1 mm [28].

At the sub-micron scale, Schenker et al. [18] described the cell wall pore structure of roasted coffee using mercury intrusion porosimetry mixed with cryo-scanning electron microscopy, proving that roasted beans contain a bimodal pore size distribution: a macropore population originating from cell wall disruption (diameters of tens to hundreds of micrometres) and two distinct micropore populations within the intact cell wall material, with average diameters of approximately 100 nm and 10 nm respectively, forming what they described as an ink-bottle pore structure in which wider micropore chambers are accessible only through narrow necks.

High-temperature, short-time roasting profiles were found to produce larger micropores and significantly higher total pore volumes than low-temperature, extended-time profiles at the same roast degree — a structurally important result because larger micropores facilitate solute diffusion from the cell wall matrix into the macropore network, while narrower micropores create additional diffusional resistance. These two micropore populations are therefore directly relevant to the

compound-class dependence of intraparticle diffusivity: small, highly soluble molecules like caffeine can diffuse through both populations, whereas larger species such as melanoidin fragments may be effectively excluded from the narrower population.

The two porosity scales relevant to solute diffusion — the intraparticle macroporosity (the void fraction internal to the particle accessible to the aqueous solvent) and the micropore volume within the cell walls — differ essentially in their roles. Macropores act as the primary conduits for solvent infiltration and for the transport of dissolved species toward the particle surface. Micropores within the cell wall matrix host much of the extractable soluble material and govern the ultimate step of solute desorption and diffusion into the macropore network. On the other hand, the interparticle bed porosity, described as the void fraction outside the particles inside the packed bed, governs the bed's hydraulic permeability and the convective transport of dissolved compounds along the bed length via the Darcy momentum equation. These two porosities play very different roles in extraction and must not be confused: intraparticle porosity defines how rapidly solute can migrate within a particle, while inter-particle bed porosity determines how rapidly the mobile phase carries dissolved compounds through the bed [30].

The ratio of effective intraparticle diffusivity to free-solution diffusivity, D_{eff}/D, is equivalently characterised through the hindrance factor H_f =D/D_{eff}, which combines the effects of both porosity levels and of the tortuosity and constrictivity of the pore network. Values of H_f in the range of 10–260 have been reported for roasted coffee particles depending on roast degree, particle size, and the specific solute, corresponding to D_{eff}/D ratios of 0.004–0.1 [4][19]. These values are substantially lower than those predicted by porosity alone, indicating the combined effects of pore tortuosity and constrictivity. Regarding large macromolecular species such as melanoidins, constrictivity effects are quite marked, and intraparticle diffusion is correspondingly slower, explaining the observed biphasic extraction kinetics in which caffeine is rapidly extracted in the initial phase while large-molecular-weight species are extracted over much longer timescales.

The pore structure is not static during extraction. As soluble material is leached from the solid matrix, the intraparticle porosity increases, reducing tortuosity and increasing D_{eff} over time. Simultaneously, the absorption of water by the polysaccharide and protein network causes particle swelling, which modifies the inter-particle packing geometry and changes the bed permeability. Swelling of coffee particles during extraction has been investigated and quantified using micro-CT at successive extraction time points [19], and independent gravimetric measurements have accounted for the progressive mass reduction of individual particles as extraction goes on [18]. Mo et al. [19] specifically used SPH simulations

built from micro-CT structural data to show that the post-extraction porosity profile along the filtration direction is heterogeneous, with finer particles and lower-porosity zones concentrated at the filter exit end as a result of pressure-driven compaction, fines migration and erosion, a finding that directly links the dynamic structural development of the bed to its hydraulic resistance history. The coupling between these structural dynamics, as well as the hydraulic and mass transfer properties of the bed, represents one of the most challenging aspects of physically complete coffee extraction modelling, and has motivated the development of mesoscopic simulation approaches in which individual particles are tracked as deformable objects within the flow field [31].

The particle size distribution of ground coffee is a critical structural variable that connects particle-scale properties to bed-scale performance. Experimental studies conducted on ground coffee, from a burr grinder, show a bimodal distribution: a primary coarse fraction around 100–1000 μm and a secondary fine fraction below 100 μm, with the relative proportions of the two populations depending on grinder type, burr geometry, grind setting, and operating speed [32]. A systematic experimental study by Guerra et al. [33] on espresso extraction, whose two-population geometry is illustrated in Figure 2.2, quantified the dominant role of the fine fraction, showing that the parameter $Q_3(100\mu m)$ — the cumulative mass fraction of particles passing a 100 μm sieve — was the strongest predictor of extraction time and pressure dynamics throughout a large set of grind conditions: increasing $Q_3(100\mu m)$ from 10% to 40% nearly doubled the extraction time at a fixed pressure, reduced bed permeability by over an order of magnitude, and substantially increased the early-eluting compound concentrations in the cup.

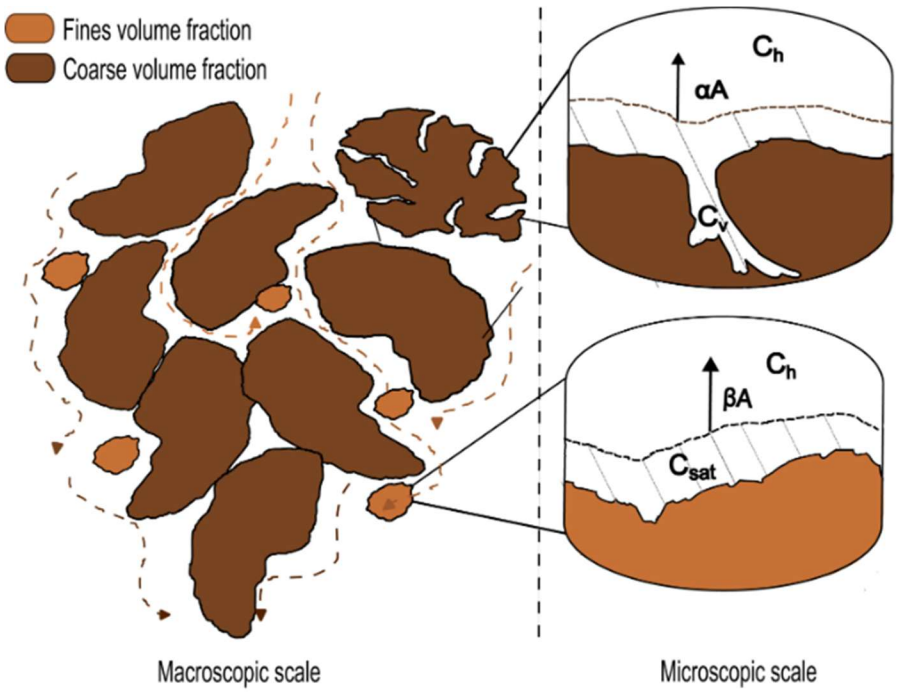

Figure 2.2: Two-population (coarse + fines) model schematic showing macroscopic particle distribution (left) and microscopic extraction mechanism for each population (right) [34].

Vaca Guerra et al. [33] demonstrated experimentally that, for coarse fractions at the same mean size, distributions with lower size uniformity (wider spread) yielded lower bed porosities under axial compression than more uniform distributions, indicating that particle shape heterogeneity — not just mean size — is a determinant of bed packing density and hence permeability. This two-population behaviour motivates the dual-particle-class modelling framework described in the following section.

2.3. Governing Equations for Multi-Component Extraction in a Packed Coffee Bed

The mathematical description of coffee extraction in a packed bed involves three coupled sets of principal equations: a momentum balance for the flow of the aqueous phase through the inter-particle void space; a mass balance for each extractable compound in the liquid phase; and a depletion equation for each compound class in the solid phase. In contrast to Chapter 1, which surveyed the historical development of extraction frameworks, the present section focuses on the

mathematical design of the multi-scale model, the constitutive equations required for its closure, and the experimental data from coffee-specific case studies that anchor the numerical values of the key parameters.

The solid-phase depletion of each extractable compound is governed by a mass balance on an individual particle, in which the driving force for transfer is the deviation of the particle's volume-averaged solid-phase concentration from its local equilibrium value. This linear driving force (LDF) formulation allows the reduction of the intraparticle diffusion problem into a single lumped equation per particle class, with a total mass transfer coefficient that includes the combined resistance effects of intraparticle diffusion and interfacial film transport [4]. This formulation, mathematically equivalent to driving-force models used in fixed-bed adsorption and chromatographic columns, was first verified for coffee extraction by Moroney et al. [4] applied to two particle classes (coarse and fine), correctly representing the biphasic concentration behaviour checked experimentally.

The liquid-phase mass balance at the bed scale counts on three contributions: advective transport of dissolved compounds through the bed axis by the Darcy flow, accumulation in the inter-particle void space, and the source from solid-phase release among each particle species. When axial dispersion is non-negligible, a diffusive term proportional to the axial dispersion coefficient D_{ax} is included. Vaca Guerra et al. [34] essentially measured D_{ax} using tracer pulse experiments at consecutive extraction steps (Figure 2.3) and found an increase of approximately 3–7 × 10^{-7} $m^2 \cdot s^{-1}$ during embryonal filling to up to 15 × 10^{-7} $m^2 \cdot s^{-1}$ at steady-state flow; incorporating this time-varying D_{ax} particularly strengthened agreement using experimental concentration profiles for caffeine, trigonelline, and 5-CQA.

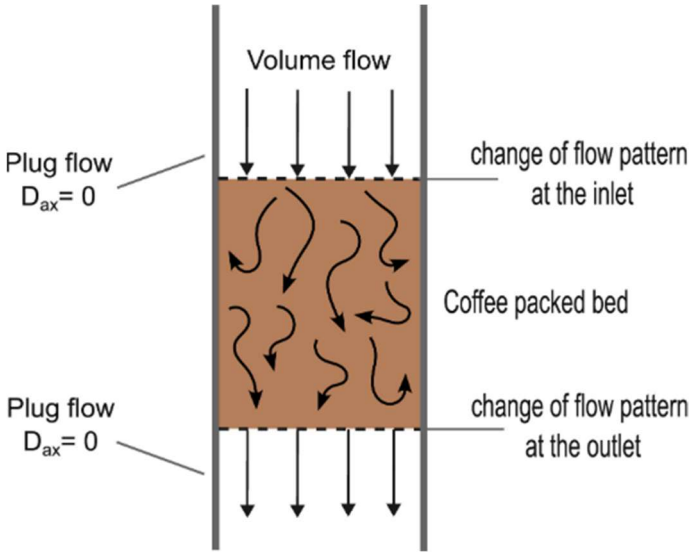

Figure 2.3: Schematic of axial dispersion within the espresso packed bed. Tortuous inter-particle pathways generate hydrodynamic mixing characterised by D_{ax}; inlet and outlet are approximated as plug flow (D_{ax} = 0) [34].

The overall mass transfer coefficient combines two resistances in series: the external liquid film surrounding every particle and the intraparticle diffusion path inside it. Their relative importance is quantified by the Biot number; for caffeine under usual espresso conditions, this ends in the range 1–5 [4], pointing out that both resistances are comparable. This is consistent with the experimental observation that caffeine extraction responds effectively to changes in flow velocity — i.e. to the external film coefficient — whereas melanoidins, for which intraparticle diffusion completely controls the rate, show no dependence on flow rate. In coffee-specific simulations at 90°C, Vaca Guerra et al. [34] estimated external film coefficients of 1.4×10^{-4} m·s^{-1} for caffeine and 2.0×10^{-4} m·s^{-1} for trigonelline, with variations between every compound reflecting the molecular diffusivity entering through the Schmidt number.

The effective intraparticle diffusivity D_{eff} is not determined by pore geometry alone: it reflects the combined effect of tortuosity, constrictivity, and direct molecular interactions between the diffusing solute and the solid matrix. It is characterised through the hindrance factor H_f= D/D_{eff}, which measures how much slower diffusion is inside the particle compared to free aqueous solution; $H_f > 1$ always and increases with molecular size and strength of solute–matrix interactions. For caffeine in roasted coffee, Spiro, Toumi & Kandiah [35] evaluated the hindrance factor via infusion experiments on solute-free wet particles at 80°C and found $H_f \approx$ 14, implying D_{eff} around 14-fold lower than in free water. Spiro & Chong [36] measured the same configuration at 25.5°C and found substantially higher H_f

values, reflecting stronger caffeine–chlorogenic acid complexation and matrix adsorption at lower temperatures — a result that helps explain why cold brew needs many hours to reach yields that espresso achieves in seconds. At espresso temperature (90°C) the free-solution diffusivity of caffeine in water is approximately D = 2.6 × 10^{-9} m^2 s^{-1}; at cold brew temperatures (4–20°C) it falls to roughly 0.3–1 × 10^{-9} m^2 s^{-1} — almost one order of magnitude lower [70]. The effective intraparticle diffusivity is further reduced below the free-solution value by the hindrance factor H_f = D/D_{eff}, which is also larger at lower temperatures due to stronger caffeine–matrix interactions. The combination of a lower D and a higher H_f at cold brew conditions amplifies the timescale of extraction far beyond what temperature alone would predict.

Mineral ions — Mg^{2+}, Mn^{2+}, K^+, and $H_2PO_4^-$ — show a different hindrance pattern. Jaganyi, Vanmare & Clark [37] measured H_f for these species in roasted Kenyan Arabica at 80°C, finding values in the range 10–25, with Mn^{2+} the most strongly hindered. In the comparative multi-origin study by Jaganyi & Madlala [38], H_f for caffeine was consistently lower than for mineral ions across all origins tested. Beverly et al. [39] reported H_f = 204–262 for coffee aroma compounds, around one to two orders of magnitude higher than for caffeine or mineral ions, showing steric exclusion and strong adsorptive interactions in the cell wall matrix. The resulting hierarchy — caffeine ($H_f \approx 14$) < mineral ions ($H_f \approx 10–25$) ≪ aroma compounds ($H_f \approx 200–260$) — directly determines the order of extraction in time, a sequence often observed across all brewing methods [40].

The effective intraparticle diffusivity D_{eff} is the most critical and most uncertain parameter in the extraction model. A consistent set of experimental values for caffeine, particularly, is available in the literature and constitutes an important benchmark. Early work by Spiro and Selwood [41], who performed extraction experiments on sieved coffee fractions and fitted a diffusion-out-of-sphere model, reported caffeine diffusivity measures of approximately 1.73 × 10^{-10} m^2 s^{-1} at 84.1 °C. Zanoni et al. [42] adopted the same procedure for packed-bed extraction experiments with fractions of 130–138 μm, 247–255 μm, and 554–600 μm particles at 90 °C, obtaining D_{eff} values in the range 0.23 × 10^{-12} to 4.24 × 10^{-12} m^2 s^{-1}, with larger particles yielding lower apparent D_{eff} — consistent with the longer diffusion path and lower accessible porosity fraction in coarser particles. Rodrigues et al. [43] fitted a non-steady-state diffusion model to caffeine extraction data at 90 °C and reported D_{eff} = 3.209 × 10^{-10} m^2 s^{-1}. For coffee aroma compounds (predominantly volatile esters and aldehydes, molecular weight 50–200 Da), Beverly et al. [39] used a multi-scale model that resolved both the particle-scale and bed-scale transport and obtained D_{eff} = 6.0 × 10^{-12} m^2 s^{-1} for a monodisperse particle size and 4.7 × 10^{-12} m^2 s^{-1} for a bidisperse distribution, with corresponding hindrance factors H_f = 204 and

262 respectively. These values — substantially higher than the H_f = 9–48 range reported for caffeine and mineral ions in more dilute extraction conditions — reflect the additional steric hindrance and molecular interactions present when the particle retains a high concentration of dissolved solids, as occurs in the early stages of brewing. The spread of D_{eff} values across these case studies (more than three orders of magnitude between the most and least hindered conditions) underscores the critical importance of independently characterising this parameter for the specific system under study rather than borrowing values from dilute or model systems.

Multi-component extension of the framework has been experimentally validated for caffeine and trigonelline in espresso extraction by Kuhn et al. [40], who demonstrated that the same model equations with compound-specific values of D_{eff}, m, and $q_{i,0}$— the initial mass of each extractable compound per unit volume of solid — can simultaneously describe the extraction kinetics of two chemically distinct species across a range of particle sizes and tamping pressures. They found that caffeine — with its higher water solubility and lower molecular weight — extracted faster than trigonelline under all conditions tested, and that the ratio of the two extraction rates was primarily governed by the ratio of their intraparticle diffusivities. This result directly supports the multi-compound modelling approach adopted in the present thesis. A further multi-compound case study by Vaca Guerra et al. [34] extended the framework to include caffeine, trigonelline, and 5-CQA simultaneously, fitting lumped mass transfer coefficients and saturation concentrations to experimental HPLC data: the fitted k_c values showed a clear dependence on solute polarity, with the most polar compound (5-CQA) showing the highest fitted mass transfer coefficient, consistent with its stronger partitioning to the aqueous phase and its higher mobility in the intraparticle water film. A further, more computationally intensive multi-compound validation was performed by Cameron et al. [44], who used the extraction model framework coupled with an optimisation routine to identify grind and flow parameters that maximise extraction quality for espresso, demonstrating that model-guided process design can identify non-intuitive parameter combinations — in particular, that using a coarser grind with a higher water-to-coffee ratio and a longer extraction time can yield a more uniform extraction than the conventional approach — which were successively confirmed experimentally.

Initial and boundary conditions conclude the mathematical formulation. At t = 0, the solid-phase concentration is set to $q_{i,0}$. At the bed inlet (z = 0), the entering liquid concentration corresponds to zero for clean water: C (t, 0) = 0 for t > 0. The advancing solvent front, which divides the wetted from the unwetted region of the initially dry bed and introduces a sharp discontinuity in the liquid-phase concentration field,

has been analysed experimentally by Foster et al. [45]. They used time-resolved micro-CT to follow the infiltration of water into a dry espresso bed and found that the wetting front progresses non-uniformly, with saturation times ranging from around 5 to 9 seconds depending on bed permeability. Their one-dimensional unsaturated porous medium flow model, containing Darcy's law and a capillary suction pressure at the wetting front, reproduced the observed front dynamics with good agreement, delivering a precise description of the initial filling stage.

2.4. Fluid Dynamics in Packed Coffee Beds: The Darcy Framework and its Extensions

The momentum balance for flow through the coffee bed is a fundamental part of any physically grounded extraction model. In the Darcy regime, valid at low pore-scale Reynolds values, the pressure gradient and superficial velocity are related linearly:

$$\nabla p = -\left(\frac{\mu}{k}\right) \cdot u \tag{2.4.1}$$

where μ is the dynamic viscosity of the liquid phase and k [m²] is the Darcian bed permeability. The first quantitative experimental determination of k for roasted coffee packed beds was performed by Corrochano et al. [30], who developed a dedicated methodology based on fitting steady-state flow rate versus pressure drop data to Darcy's equation. Thanks to their measurements on four bimodal particle size distributions of roasted Arabica coffee, at distinct bed bulk densities, it was possible to evaluate that permeability fell in the range of $k = 10^{-13}$–10^{-14} m², with $R^2 > 0.97$ for all linear fits. A critical finding was that the Kozeny–Carman equation basically underestimated the hydraulic resistance of compressed coffee beds: the values of permeability measured by experiments was fundamentally lower than the Kozeny–Carman prediction computed from dry particle size distributions. This happens because bed consolidation under the applied pressure gradient reduces the effective bed porosity below the dry-packing value by up to 31% in the most compressible distributions. This result proves that bed consolidation, not particle size alone, is the prevailing factor of coffee bed permeability under brewing conditions.

For packed beds, the Kozeny–Carman equation provides a theoretical relationship between permeability and structural parameters such as porosity, particle sphericity and tortuosity. Corrochano et al. [30] derived a modified form correcting for the porosity-dependent tortuosity of the bimodal coffee packing, which achieved significantly better agreement with experimental data than the standard equation, reducing the relative prediction error from up to 300% to within

experimental uncertainty. This modified correlation, incorporating the consolidation-corrected bed porosity and measured sphericity values (0.71–0.80), forms the basis for the permeability estimation adopted in the present thesis.

At the pore-scale Reynolds numbers typical of espresso extraction — of order 10^{-2} to 10^{-1} — the Darcy equation provides a physically sound and widely validated description of flow through the compacted bed. Experimentally, however, a persistent inconsistency has been observed in the coffee engineering literature: permeability values measured by different research groups under different applied pressures disagree significantly, even for beds of nominally identical composition. Mo et al. [19] resolved this inconsistency using micro-CT reconstructions of real ground coffee samples combined with SPH simulations of Stokes flow through the reconstructed pore network. As shown in Figure 2.4, a key finding was that the apparent permeability decreased with increasing pressure gradient even in simulations using a static, non-deformable bed — demonstrating that the pressure-dependence of permeability is not solely attributable to bed compaction, but arises partly from inertial effects in the inter-particle flow.

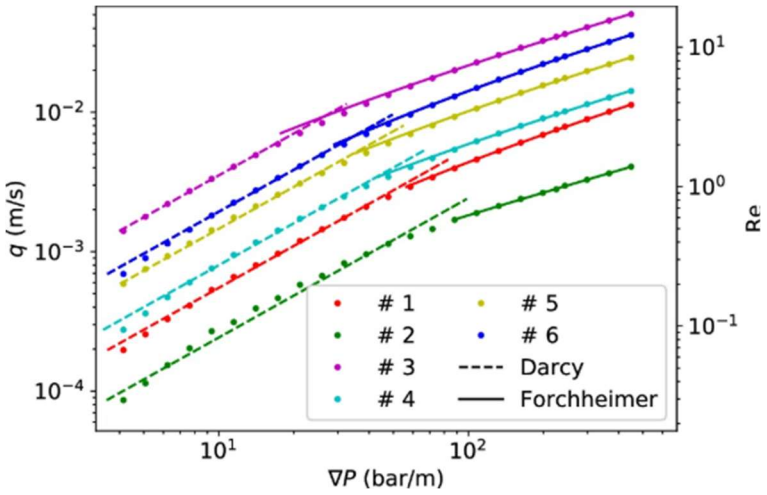

Figure 2.4: Superficial velocity q versus pressure gradient ∇P for six coffee powder samples (#1–#6) from SPH simulations on micro-CT reconstructed pore networks. Dashed lines: Darcy fits; solid lines: Forchheimer fits. The systematic upward deviation of the data from the Darcy prediction at high ∇P demonstrates the onset of inertial effects. Reynolds numbers (right axis) reach order 1–10 at typical espresso operating pressures [19].

The SPH-fitted values were $k = 8.0 \times 10^{-13}$ m² and $k_1 = 2.17 \times 10^{-13}$ m ,whit this last parameter representing the inertial permeability appearing in the Forchheimer

extension of Darcy's law, responsible for the quadratic inertial pressure losses at higher flow rates through the term $\varrho v^2 / k_1$.

This assesses that, at high flow rates or steep pressure drops, the linear Darcy relation underestimates the actual pressure drop, and that the Forchheimer equation — which adds a quadratic inertial term — is needed for numerically accurate flow prediction under those conditions.

At higher flow velocities, or in beds with complex pore spaces, the Forchheimer modification accounts for acceleration effects through a quadratic pressure-velocity term:

$$\nabla P = -\left(\frac{\mu}{k}\right) \cdot u - F \cdot \rho \cdot |u| \cdot \frac{u}{\sqrt{k}} \tag{2.4.2}$$

where F is the dimensionless Forchheimer coefficient and ρ is the fluid density [46]. The onset and magnitude of non-Darcian behaviour is characterised by the Forchheimer number Fo [46]:

$$F_0 = F \cdot \rho \cdot u \cdot \frac{\sqrt{k}}{\mu} \tag{2.4.3}$$

For the SPH-computed flow field of Mo et al. [19], Fo values on the order of 10–25 were estimated in typical espresso flow conditions, confirming the relevance of inertial contributions. A complementary analysis by the Royal Society Open Science permeability model [47], that adopted lattice-Boltzmann simulations of fluid flow through micro-CT-reconstructed coffee packs at 11 different grind setups, found that the Forchheimer number criterion correctly predicted the onset of non-Darcian behaviour along all the range of grind sizes and flow rates tested, and that the inertial permeability k_1 could be evaluated from the Darcian permeability k through the relationship $k_1 \propto \sqrt{k}$, consistent with the dimensional form of the Elsanoose correlation [48].

A particularly important and complex feature of coffee bed fluid dynamics is the time evolution of bed structure — and hence of both k and F — during extraction. This evolution occurs through three coupled mechanisms, each characterised in dedicated experimental studies. The first is fines migration: Ellero and Navarini [31] used SPH mesoscopic simulations at the grain scale to show that sub-100 μm particles are mobilised by hydrodynamic drag within the first 4–5 seconds of extraction (phase 1b), migrating downward through the bed in the flow direction and accumulating near the filter exit, creating a progressively more compacted, low-permeability layer that dominates the hydraulic resistance during the subsequent steady-state phase. The second mechanism is swelling: Mo et al. measured the effect of particle swelling on bed permeability, demonstrating that 10–30% volume increases in individual particles upon water absorption translated into concrete reductions in bed permeability over the 20–60-second timescale of extraction. The

third mechanism is poroelastic compaction: Skotnicki et al. [50] built up a poroelastic model of the coffee bed that included the elastic deformation of the granular matrix under the applied pressure, and found that at brewing pressures above around 9 bar, the predicted flow rate saturated and became essentially independent of further pressure increase — a behaviour coherent by experimental observations by espresso practitioners and validated against time-resolved TDS measurements. These three case studies demonstrate that the momentum balance for coffee extraction is intrinsically transient and structurally coupled, and that any model that assumes constant k and F will incorrectly predict both the fluid flow and the extraction kinetics, especially in the first 10–30 seconds of the brewing process.

The initial wetting phase, where the solvent front advances through the dry bed before steady-state percolation starts, has been characterised experimentally by Foster et al. [45] using time-resolved micro-CT with a frame rate sufficient to track the advancing waterfront in the portafilter. Their investigations showed that the saturation time ranged from about 5 to 9 seconds depending on bed permeability, and that the front velocity reduced as the headspace air above the bed was compressed. Their unsaturated porous medium model, which adopted Darcy's law in the wetted region and a capillary suction pressure at the front, basically agrees with the experimental dynamics. This result is directly relevant to extraction modelling because the period before the bed is fully wetted is precisely when the largest concentration gradients exist between the freshly contacted particles and the entering solvent, and when the highest extraction rates — and the greatest risk of spatial non-uniformity — occur.

2.5. Ultrasound-Assisted Extraction: Mechanistic Depth and Quantitative Model

The mechanistic framework introduced in §1.8 is here extended to address the quantitative relationships between acoustic parameters and mass transfer enhancement — relationships that are directly relevant to the modelling of UAE in a packed-bed context and that define the constitutive parameterisation which will be adopted in Chapter 4.

Acoustic cavitation is categorised into two regimes: stable cavitation, where bubbles oscillate periodically over several acoustic cycles without collapsing, and inertial (transient) cavitation, where bubbles grow rapidly during a single rarefaction half-cycle and collapse violently during the successive compression half-cycle [20]. The shift between these two regimes — guided by the Blake threshold pressure, a

function of bubble size, surface tension, and dissolved gas content — marks the onset of the most energetically intense cavitation events and the associated microjet formation [20]. In food extraction applications, the acoustic intensity must be sufficient to reach the inertial cavitation regime — generally requiring power densities above approximately 1 W cm^{-2} at 20–40 kHz — for the physical effects on solid surfaces and intraparticle transport to be significant [20].

The cavitation configuration depends on the frequency of the ultrasonic wave. At lower frequencies (20–40 kHz), the longer rarefaction half-cycle gives more time for bubble nucleation and growth, resulting in larger bubble radii at collapse and, correspondingly, more energetic implosion events. This is highlighted by higher erosion rates on adjacent surfaces and higher effective microjet velocities at low frequency compared to high frequency for the same applied power density [21]. Conversely, high-frequency ultrasound (100 kHz to MHz range) forms more numerous but smaller, less energetic cavitation events, which may be better suited to surface cleaning than to increasing bulk extraction. For solid–liquid extraction from food matrices, frequencies in the range of 20–40 kHz set the greatest improvements in yield and kinetics [20][21].

Acoustic streaming, the time-averaged bulk fluid motion influenced by the propagation of an absorbing ultrasonic wave through the liquid, is a mechanism different from cavitation and contributes independently to mass transfer enhancement. Eckart streaming, bulk streaming driven by the absorption of acoustic energy inside the fluid volume, and Rayleigh–Nyborg–Westervelt (RNW) streaming, local streaming at acoustic boundaries, together decrease the effective boundary layer thickness at solid surfaces even in configurations where cavitation is suppressed [20]. In free liquid, streaming velocities of 0.1–1 m s^{-1} have been evaluated at typical food processing power densities [20]. In a porous medium, however, the governing espressions for acoustic streaming diverge fundamentally. Raghavan [51] demonstrated that in Darcy-limited porous media, the streaming velocity decreases with the hydraulic conductivity of the medium and is several orders of magnitude lower than in free liquid for the same acoustic input power. In the densely packed coffee bed (permeability 10^{-13}–10^{-15} m^2, porosity 0.12–0.33 [30]), bulk acoustic streaming at bed scale is strongly suppressed. However, at intraparticle level two local mechanisms remain incisive: acoustic pumping through the macropore network and microstreaming driven by bubble oscillation in larger macropores.

Inside the solid particle, the mechanisms of acoustic enhancement differ from those in the bulk liquid. Cavitation within the pore network is usually limited to the largest macropores, where enough space exists for bubble nucleation and growth. The primary mechanisms of intraparticle enhancement under sonication are

therefore: (i) acoustic pressure-driven oscillatory flow through the pore network (sometimes termed sponge effect or acoustic pumping), where the alternating pressure of the ultrasonic field guides periodic solvent flow in and out of the pore channels, convectively transporting dissolved species toward the particle surface; and (ii) microstreaming within large macropores created by the oscillation of any bubbles present [20][50]. Both mechanisms impact the diffusion path, reducing the effective tortuosity and increasing D_{eff} beyond what would be predicted from the porosity alone, consistent with the order-of-magnitude increases in effective caffeine diffusivity evaluated under sonication [26].

The spatial distribution of acoustic intensity within a packed bed diverges deeply from that in a free liquid or a dilute suspension. In a packed bed, acoustic waves are attenuated by deflection at particle surfaces and by viscous absorption inside the inter-particle liquid. The attenuation coefficient depends on the particle size relative to the acoustic wavelength, the acoustic impedance mismatch between the solid particles and the liquid, and the packing density. At 20 kHz, the acoustic wavelength in water is approximately 75 mm, which is much larger than usual coffee particle diameters (0.1–1 mm), placing the system in the Rayleigh scattering regime where attenuation scales with the fourth power of particle diameter.

The probability and vigour of inertial cavitation near a granular boundary are essentially reduced compared to a rigid wall — a finding having direct implications for the dominance of acoustic streaming over cavitation in a compacted coffee bed, as will be developed quantitatively in Chapter 4. Sieber, Preso & Farhat [52] and Andrews, Fernández Rivas & Peters [53] provide the key experimental and conceptual models. Sieber et al. showed that a granular boundary differentiates bubble collapse into three regimes as a function of the stand-off parameter γ, defined as the distance between the initial bubble center and the granular surface normalised by the maximum bubble radius. For $\gamma > 1.3$, the dynamics approach those near a rigid wall; for $0.6 < \gamma < 1.3$, a granular mound cushions the rebound; for $\gamma < 0.6$, the collapse energy is absorbed into the porous medium rather than forming the directional microjet responsible for mass-transfer enhancement near rigid walls. Andrews et al. extended this to porous plates, showing that bubble displacement and rebound radius collapse onto universal curves against the anisotropy parameter $\zeta = g(\varphi)\gamma^{-2}$, where $g(\varphi)$ decreases from 0.195 at $\varphi = 0$ to 0 at $\varphi = 1$. At the inter-particle void fraction of a compacted espresso bed, ζ falls into the regime where inertial collapse is suppressed. The extended quantitative argument will be developed in Chapter 4.

Therefore, acoustic intensity decreases with depth from the transducer face, and the spatial distribution of cavitation activity — and of the associated extraction

enhancement — is highly non-uniform within the bed. This fundamental feature of UAE in packed-bed configurations has no equivalent in conventional brewing and represents the primary physical challenge in translating the per-particle enhancement documented in suspension experiments to the bed-scale extraction performance relevant to practical coffee brewing.

The quantitative parameterisation of UAE enhancement effects in extraction models has been approached through two strategies in the literature. The first is a phenomenological enhancement factor approach, in which acoustic enhancement is incorporated by multiplying the baseline transport parameters by dimensionless factors E_{ext} and E_{int}, for external and intraparticle enhancement respectively, calibrated from experimental extraction data at specific acoustic conditions [20]. The second is a more mechanistic approach, in which the acoustic power density and streaming velocity are used as inputs to modify Sherwood number correlations or to adjust effective diffusivity expressions derived from pore-scale acoustic field calculations [21]. Both approaches require experimental calibration data for each specific system, and neither has been applied to coffee extraction in a packed-bed geometry.

2.6. Ultrasound-Assisted Extraction of Coffee: A Critical Assessment of the Evidence

The experimental literature on UAE coffee extraction, surveyed at a descriptive level in Subchapter 1.9, is here assessed analytically describing: what the available data actually establish, what are the methodological restrictions that constrain their interpretation, and what quantitative information is and is not available for mechanistic modelling.

The most robustly established finding across UAE coffee studies is that acoustic treatment consistently produces statistically relevant increases in the aqueous concentrations of caffeine, chlorogenic acids, and trigonelline relative to non-sonicated controls conducted under matching conditions of time, temperature, and liquid-to-solid ratio [22][23]24]. These yield increments are replicable across independent laboratories and across several brewing configurations (cold brew immersion, hot water flow-cell), and they correlate positively with acoustic amplitude in all studies that have varied this parameter [22][23]. The underlying physical mechanism — enhancement of mass transfer coefficients by acoustic cavitation and streaming — is well established in the general UAE literature [20][21] and is qualitatively consistent with the observed concentration increases in coffee.

Among the available UAE coffee studies, the work of Chiu et al. [23] stands apart from all others by virtue of its geometry: as introduced in Subchapter 1.9, it is the

only study that places coffee in a compacted packed bed rather than free suspension. The substantial yield improvements (summarized in Table 1.3) result from the compacted geometry forcing acoustic energy through the porous bed, activating streaming in the inter-particle space. SEM imaging of the particle surface before and after sonication (Figure 2.5) showed a progressive disruption of the cell wall structure: intact, occluded surfaces in the unsonicated control gave way to partially opened geometry under water exposure alone, and to fully exposed honeycomb cell structure under joined water and sonication. This morphological variation confirms that acoustic treatment physically opens the intraparticle pore network, consistent with the D_{eff} enhancement mechanism described in Subchapter 2.5. Notably, the authors attributed the acoustic enhancement to cavitation-driven mechanisms, operating in a cavitating fluid regime; the geometric suppression of cavitation within the compacted bed — and the effects for the relative dominance of streaming versus inertial cavitation — is the subject of the quantitative analysis developed in Chapter 4 of the present thesis. The quantitative results of Chiu et al. represent the most mechanistically relevant benchmark available for the UAE model developed in Chapter 4, and their configuration is the closest analogue to a packed-bed espresso extraction in the existing UAE coffee literature.

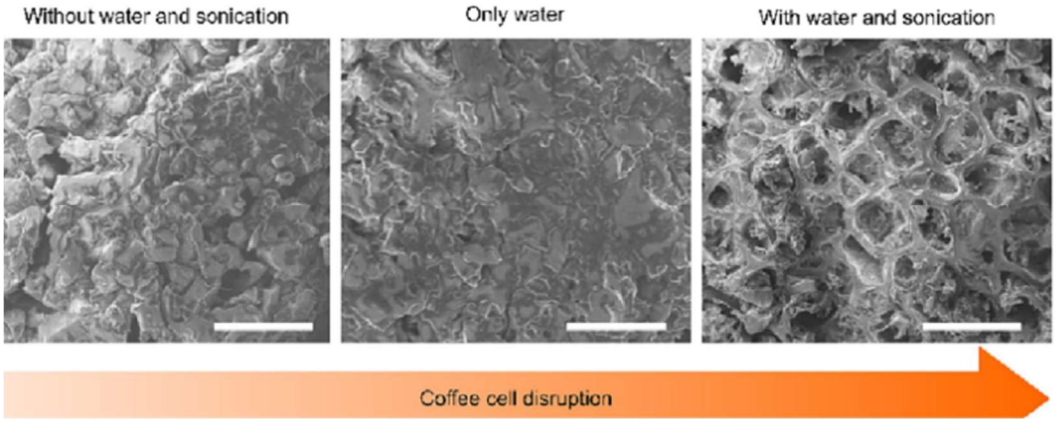

Figure 2.5: SEM images of coffee particle surfaces under three conditions: without water or sonication (left), with water only (centre), and with water and sonication (right). Progressive disruption of the cell wall structure from intact to fully open honeycomb geometry provides direct morphological evidence of acoustic enhancement of intraparticle mass transport [23].

However, the available data have important quantitative limitations. First, the relationship between the rated output power of the ultrasonic probe or bath and the actual acoustic power density delivered to the extraction medium — measured calorimetrically by the standard temperature-rise method — is inconsistently

reported across studies [20]. Without knowledge of the actual power density, it is not possible to compare results across studies or to use published data as inputs to predictive models. Second, no published UAE coffee study has independently varied acoustic frequency and power density to separate their respective contributions — a limitation that partly reflects the practical constraint that, in resonant transducer systems, frequency and power are coupled by the resonance condition of the transducer–vessel assembly, making independent variation technically non-trivial. Since cavitation configuration, bubble size at collapse, and microjet velocity strongly depend on frequency in ways that are theoretically well understood [20][21], this experimental lack prevents attributing observed yield increments to specific physical processes. Third, all studies that have reported sensory evaluation alongside physicochemical analysis have used untrained or semi-trained panels [22][23], limiting the resolution of sensory data relative to the component differences detected analytically. A study using a trained panel and a specific compound threshold analysis would be needed to determine whether the UAE-induced compositional changes fall within or exceed the acceptable sensory window.

The most mechanistically informative data available for modelling purposes come from studies that report a transport coefficient — specifically an effective diffusivity — as a primary output, rather than only compound concentrations. The only published study of this type for coffee is that of Huamaní-Meléndez and Darros-Barbosa [26], who fitted an intraparticle diffusion model to caffeine extraction kinetics at different ultrasonic intensities and temperatures, extracting D_{eff} as a function of these parameters. Their values of D_{eff} in the range 8.9–10.6 × 10^{-11} m^2 s^{-1} under optimal sonication represent the improvement by one to two orders of magnitude over free-solution diffusivity, qualitatively consistent with the acoustic pumping and microstreaming mechanisms described in Subchapter 2.5. However, the study was conducted in a dilute suspension of beans (not a packed bed), at a single frequency (24 kHz), and for a single compound (caffeine). The dependence of D_{eff} enhancement on particle size, bed packing density, acoustic frequency, and compound molecular weight — all parameters relevant to the multi-compound, packed-bed model developed in this thesis — remains uncharacterised.

The evidence from UAE extraction of coffee-derived matrices provides indirect but useful complementary information. When ultrasound-assisted extraction was benchmarked against a conventional reference for polyphenol recovery from spent coffee grounds, the yield improvement of 33% documented alongside a measurable reduction in specific energy consumption [27] ended within the 15–40% range reported for UAE polyphenol extraction from plant matrices more broadly [20][21], and is consistent with the enhancement values reported for primary coffee brewing.

This proves that the behaviour of coffee matrices in the presence of acoustic treatment is reproducible across compound classes, while pointing out that absolute magnitudes are configuration-specific and cannot be extrapolated between geometries.

Taken together, these observations validate that the existing UAE coffee literature, while establishing the existence and approximate magnitude of acoustic enhancement, does not provide the mechanistic parameter values needed for quantitative prediction in new configurations — in particular, the packed-bed configuration relevant to real brewing and to the model developed in this thesis. The specific gaps identified — the absence of frequency-dependence and compound-class-dependence data for D_{eff} enhancement, the limitation of all studies to non-packed-bed geometries, the inconsistent reporting of actual acoustic power density, and the lack of training-panel sensory data for the acoustically modified brew — define the experimental and modelling programme required to bring UAE coffee extraction to the level of mechanistic understanding already achieved for conventional brewing.

3 Research Objectives and Thesis Structure

3.1. Identification of Research Gaps and Formulation of Objectives

The review of the state of the art presented in Chapters 1 and 2 exhibits a consistent and specific gap in the scientific literature on coffee extraction. On the conventional side, multi-scale extraction models able to predict the concentration–time profiles of individual compound classes in a packed bed have been developed and experimentally validated [4][6], and the fluid dynamics of flow through the bed within the Darcy framework are well characterised [19][30]. The transition from single-compound to multi-component models has been demonstrated for caffeine and trigonelline [40], and a model-guided optimisation approach for espresso quality has been developed [44]. The structural heterogeneity of the roasted coffee particle — including the progressive evolution of porosity and permeability during extraction and the central role of fines dynamics in bed hydraulics — has been experimentally documented and computationally investigated [19][30][31]. The mechanistic framework for conventional packed-bed extraction is therefore substantially mature.

On the ultrasound-assisted side, by contrast, the situation is fundamentally different. A substantial body of experimental work has established that acoustic assistance boosts the extraction of caffeine, chlorogenic acids, trigonelline, and volatile compounds from coffee [22][23][24][26], and the intraparticle diffusivity enhancement for caffeine has been directly measured under optimised sonication conditions [26]. However, as far as the literature indicates, no mechanistic model connecting acoustic operating parameters to the transport coefficients of the extraction system has been developed for coffee. No UAE study has been conducted in a packed-bed configuration under a pressure gradient. Actual acoustic power density is rarely reported with sufficient precision to enable quantitative comparison between studies [27]. And the question of how UAE performance — in

terms of both yield and selectivity across compound classes — depends on the association between acoustic parameters and bed structural properties remains entirely unaddressed in the literature.

Furthermore, the acceptable extraction window — defined by the Specialty Coffee Association as a total dissolved solids yield of 18–22% of the total soluble mass — constrains the pragmatic utility of any intensification strategy [54]. Acoustic intensification that increases extraction indiscriminately across all compound classes may push the system into the over-extraction regime, in which the mobilisation of high-molecular-weight melanoidin fragments, diketopiperazines, and bitter chlorogenic acid degradation products degrades cup quality through excessive bitterness and astringency [55]. An effective UAE strategy must therefore be capable of increasing yield selectively — preferentially improving the extraction of target compounds such as caffeine while limiting the disproportionate mobilisation of species responsible for over-extraction. This degree of selectivity can be assessed using a modelling configuration that tracks the extraction kinetics of individual compounds; in the present work, the extraction model is limited to caffeine, given its established role as a benchmark for overall extraction efficiency in the literature.

The dual-population mass transfer model — which separately describes coarse particles and fines, each with their own characteristic diffusion length, surface concentration, and mass transfer coefficient — is the natural extension of the single-population approach for representing the heterogeneous extraction dynamics of real coffee beds. The quantitative differences between fines and coarse particles in their response to acoustic enhancement cannot be assessed from single-particle or suspension experiments and requires a packed-bed model for its evaluation.

The present thesis directly responds to these gaps. The first step is to develop and validate a physically grounded, multi-scale mathematical model of coffee extraction — first under conventional conditions and subsequently extended to account for ultrasonic intensification — incorporating the Darcy momentum balance, coupled solid- and liquid-phase mass balances for multiple compound classes with physically motivated mass transfer coefficients, and a finite difference discretisation with an implicit backward-Euler scheme. The extended UAE model includes acoustic enhancement of the external mass transfer coefficient in a mechanistically justified and independently parameterised manner, obtained from the granular-column mass transfer coefficient correlation, through the bulk fluid velocity improvement computed from the Biot poroelastic model.

Three specific objectives derive from this overarching aim. The first is to build and validate the multi-scale model for conventional coffee extraction, independently estimating each transport parameter from literature correlations and experimental

structural data. The second is to extend the model to the UAE case. To frame this objective it is necessary to distinguish between the two principal configurations studied in the UAE coffee literature. Cold brew extraction is an immersion process where coarsely ground coffee is steeped in cold water (4–20°C) at a coffee-to-water proportion of around 1:10–1:12 for 12–24 hours without any applied pressure; in this scenario, published UAE studies report caffeine yield improvements of 25–55% relative to non-sonicated controls [23][25], because the long contact time and dilute geometry concede ample opportunity for acoustic cavitation and streaming to enhance diffusion throughout the bulk of the liquid. Espresso extraction, by contrast, is a pressurised percolation process in which hot water (80–96 °C) is forced at 7–9 bar through a compacted packed bed of finely ground coffee at a ratio of 1:2–1:3 in only 25–30 seconds, and it is precisely this configuration that is adopted in the present thesis. In this configuration, the contact time is two to three orders of magnitude shorter, the coffee-water ratio is four to six times higher, convective transport already dominates mass transfer due to the forced pressure gradient, and — critically — acoustic cavitation is strongly suppressed within the compact bed while streaming is Darcy-limited, as established in Subchapter 2.5. These fundamental differences mean that the yield increments achievable by UAE in espresso-style packed-bed extraction are expected to be substantially lower than those reported for cold brew. A conservative estimate, grounded in the physical suppression of both cavitation and streaming in a dense packed bed, suggests caffeine yield increments on the order of approximately 10% — an estimate consistent with the acoustic streaming suppression in the compacted bed and anchored to the packed-bed-like configuration studied by Chiu et al. [24] under realistic sonication conditions, compared to the 25–55% reported for cold brew suspension configurations. Any quantitative target must therefore be treated as a working hypothesis requiring model-based validation instead of a direct extrapolation from the cold brew literature. The last objective of this thesis is therefore to use the developed model to identify the conditions under which a meaningful — but physically realistic — improvement in caffeine extraction yield can be achieved in the espresso packed-bed configuration, and to assess how this compares with the cold brew baseline reported in the literature.

3.2. Organisation of the Thesis

The thesis is organised into eight chapters, each addressing a distinct aspect of the overall research programme.

Chapter 1 (Introduction) introduces the scientific and practical context of the work. It describes the chemical composition of the coffee matrix, providing a basic explanation of how solid-liquid mass transfer operates in espresso extraction. It describes the central variables of the extraction process and introduces the porous architecture of roasted coffee bed particles. It then introduces the choice to apply ultrasound to intensify coffee extraction, motivated by research and reviews on the topic.

Chapter 2 (State of the Art) provides the background literature on the main experimental models that can be readily referred to and compared with the model developed in the present work. It focuses on reviewing how the principal experimental features are analysed in likely experimental model types in the literature, such as pore structure and its evolution during extraction, and the mechanistic basis for ultrasonic improvement of solid-liquid mass transfer.

Chapter 3 (Research Objectives and Thesis Structure) states the thesis's modelling objectives, identifies the research gaps outlined in the preceding chapters, and presents its structure.

Chapter 4 (Theoretical Development) develops the entire mathematical model. It gives an initial process description, including system geometry and overall process assumptions. After motivating the exclusion of cavitation, it derives equations for solid- and liquid-phase transport and mass-transfer fundamental relationships, for both conventional and ultrasound sub-problems, comprising the Biot poroelastic acoustic model, the solid mechanics of the steel basket, and the acoustic streaming formulation using the Brinkman equations. At the end of it all, model parameters and their estimation from literature correlations are reported.

Chapter 5 (Model Parameters and Material Properties) includes the operating parameters of the espresso extraction process, the coffee bed properties derived from the particle-size distribution and the physical properties of the steel basket, water, and system geometry. All values are taken from the literature or estimated from experimental structural data through the correlations adopted in Chapter 4.

Chapter 6 (Parametric Study and Numerical Approach) describes the numerical implementation of both sub-problems. It presents the finite difference discretisation and implicit time-stepping scheme for the extraction model, and the COMSOL Multiphysics meshing strategy, solver configuration, and convergence criteria for the acoustic–poroelastic model.

Chapter 7 (Results and Discussion) presents and analytically discusses the simulation results. Here firstly the conventional extraction model is validated against an experimental caffeine kinetics from literature, then a parametric study further investigate the behaviour of acoustic velocity and acoustic streaming fields,

under the influence of a certain basket thickness (0.4-0.7), ultrasonic power (50-200W) over a frequency range of 20-40 kHz. After verifying the validity of the modelling assumptions, the coupling of the acoustic streaming velocity to the extraction model yields caffeine matches the enhancement predictions across all parametric configurations, which are compared with those reported in literature.

Chapter 8 (Conclusions and Future Developments) summarises the main findings, offers final considerations on the modelling assumptions, their limitations, and the final results, and outlines directions for future experimental and modelling work

4 Theoretical Development

4.1. Process Description

From a modelling perspective, coffee extraction can be seen as a solid-liquid extraction in a granular column, where the granular media is the coffee grind and the extraction liquid is the hot, pressurized water. This is a convection-diffusion problem [33], the solutes diffuse through the coffee particles and are then transported by the bulk fluid. Espresso machines use water at 90 ± 5 ℃ with head pressures up to $9 \pm 2\ bar$ [3]. The extraction set-up is pretty much standardized across all machines, with extraction times in the range of $30 \pm 5\ s$ [3]. The coffee bed properties, such as porosity, permeability and roasting degree, are directly dependent on multiple factors. They are mainly the origin, the roasting degree and the grinding size, while tamping force characterizes the degree of compaction of the puck, consequently affecting also bed porosity and hydraulic resistance.

The application of ultrasound to an espresso-type machine impacts on the extraction with only one mechanical effect: acoustic streaming, the formation of a steady fluid flow due to the second order terms of the acoustic velocity appearing in the Reynolds stress tensor. The description of the acoustic field and the streaming forces generated will be examined in dept in Subchapter 4.7 through the Biot poroelastic theory. Successively, the Reynolds stress tensor, obtained by derivation from this field, is utilised as a volumetric body force input for the Brinkman equations, from which the acoustic streaming velocity is obtained. Ultimately the acoustic velocity field and the modified mass transfer coefficients are used to determine the enhanced caffeine concentration.

On the contrary, inertial cavitation , despite being the dominant mechanism in configurations adopting UAE water-free suspension systems, is excluded from the model because of geometric suppression inside the compacted espresso bed, as will be explained in Subchapter 4.2.3.

4.2. System Setup

4.2.1. Basket Geometry and Configuration

The set-up is a standard single-dose espresso portafilter basket: a cylindrical coffee chamber of 4.6 cm internal diameter and 1 cm height, made of food-grade AISI 304 stainless steel. The basket thickness ranges from 0.4 to 0.7 mm. The single physical modification respect to a standard espresso extraction configuration is the attachment of the horn to the outer lateral wall. It covers ¼ of the side surface uniformly (total height) because the chamber is locked inside of the machine, with the exception for the side where the horn is placed. Figure 4.1 constitutes the closest available example to the packed-bed geometry modelled in the present work.

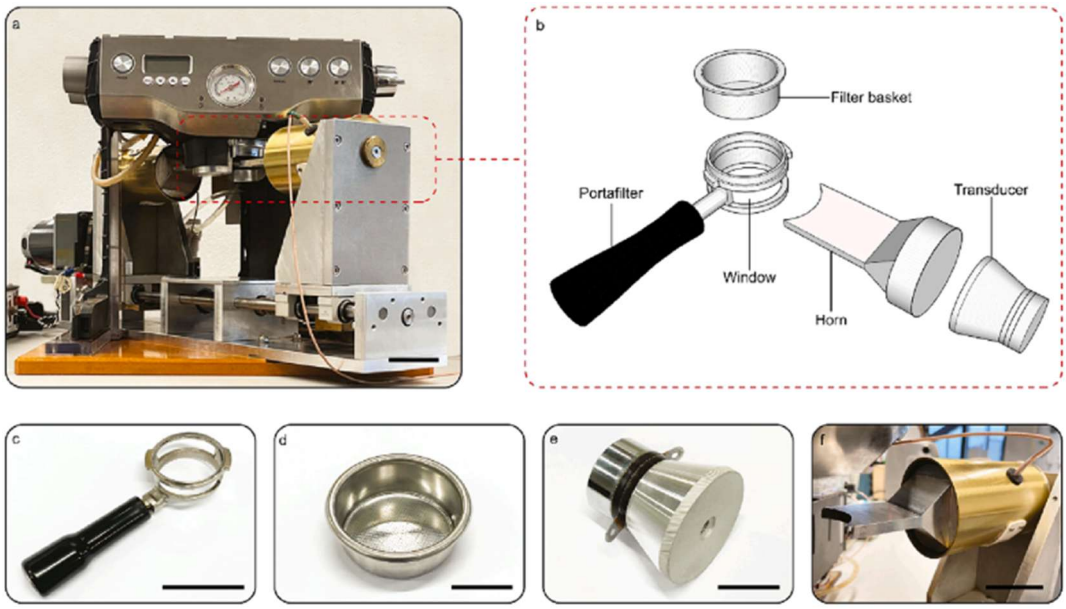

Figure 4.1: Customised ultrasonic coffee brewing machine. a) Photograph of the machine. b) Schematic of the parts for the ultrasound transmission into the coffee basket. c-f), Photographs of the portafilter (with corresponding window), filter basket, transducer, and the horn, respectively. (scale bar: 4 cm). [23]

4.2.2. Modelling Assumptions

The proposed model rests on a set of assumptions and simplifications that are motivated by the physics of the system and by practical modelling considerations. The first concerns the structure of the porous medium: Biot's poroelastic model assumes the material to be homogeneous and isotropic **(a)**, which requires that the pore size of the porous matrix be significantly smaller than the wavelength of the slowest acoustic wave [79], i.e. the one with the smallest wavelength. The second concerns the temporal separation of scales between the acoustic and extraction dynamics: transient times for acoustic field instauration are in the range of milliseconds [64][78], while the extraction process operates on a range of $25 - 35\ s$ as discussed in Subchapter 4.2.1; this separation justifies the assumption of steady-state conditions for the acoustic field **(b)**. Both the porous coffee matrix and the steel basket are treated as linear elastic isotropic materials **(c)**, a standard assumption in poroelastic modelling that avoids the additional complexity of anisotropic constitutive relations. The flow regime within the bed is laminar **(d)**: the extremely low permeability of compacted espresso coffee matrices generates slow fluid velocities and low Reynolds numbers ($Re_P < 10$ with pore diameter as characteristic length [84]), allowing neglecting inertial terms [33][30]. Water is treated as an incompressible fluid **(e)** over the pressure and temperature range of interest. Since no information on the actual pore geometry is available, cylindrical pores are assumed **(f)**, consistent with Biot's original formulation [79]. To avoid complications coming from the partial saturation transient, the initial condition of the system is taken to be a coffee matrix already saturated with pure water, with no pre-infusion phase considered. This is an assumption that resembles the realistic implementation system perfectly because the ultrasonic horn would not be activated if water were not completely saturated in the coffee bed. Therefore, coffee particles are assumed to be already swollen **(g)**. At the horn–basket boundary, the acoustic excitation is represented as a time-harmonic plane wave **(h)**, which avoids the need to model the horn and sonicator geometry explicitly — a common and well-established simplification in acoustic boundary-value problems [65]. Consistent with the geometric suppression arguments developed in the preceding sections and with the critical analysis deeply developed in the next Subchapter 4.2.3 , cavitation is neglected entirely **(i)**: in low-porosity media the phenomenon is strongly damped if not completely absent, and its omission is therefore physically justified rather than merely expedient. The extraction model is one-dimensional **(j)**, resolved along the axial flow direction z. The ultrasonic propagation model is two-dimensional **(k)**: since the horn is applied to the lateral surface of the basket rather than along the axis of symmetry, no axisymmetric simplification is available. However, because the horn is applied uniformly over the full height of the cylinder and the main flow is perpendicular to the acoustic field, a 2D formulation captures the essential

physics at manageable computational cost, and can be extended to 3D if required, albeit at significantly higher expense. Except for the horn-facing surface, all lateral walls are treated as immobile **(l)**, reflecting the constraint imposed by the espresso machine housing. The system is assumed to be isothermal **(m)**: given the high thermal conductivity of water, the liquid phase is taken to equilibrate immediately to the inlet temperature. The porous matrix is assumed to move coherently with the steel chamber walls **(n)**, grains do not shrink when losing solute **(o)**.The only ultrasonic effect considered in the extraction process is the enhancement of external mass transfer because of the presence acoustic streaming velocity **(p)**.

4.2.3. Inertial Cavitation near Granular and Porous Boundaries

Acoustic cavitation, together with acoustic streaming, is the main mechanism used to explain the extraction yield enhancement in free-suspension systems adopting UAE. However, in a different type of bed geometry, like that of an espresso compacted bed described in this present work, its effects are deeply limited. When a cavitation bubble forms near a granular or porous boundary, the collapse is substantially altered with respect to a rigid-wall case, as will be examined in the following two sections.

4.2.3.1. Geometric Suppression

Sieber, Preso & Farhat [53] performed a systematic experimental study of laser-induced single cavitation bubbles near water-saturated sand beds of varying grain size, parameterising the dynamics employing the stand-off parameter $\gamma = s/R_{max}$, the distance between the bubble centre and the granular surface normalised by the maximum bubble radius. Their central finding is that a granular boundary systematically attenuates inertial cavitation relative to a rigid wall, and that this attenuation is organised into three distinct collapse regimes as function of γ. For $\gamma > 1.3$ the bubble collapses with characteristics qualitatively comparable to those near a rigid wall, but with a notably shorter lifetime and decreased centroid displacement, because the granular surface can absorb part of the collapse energy through grain rearrangement. As shown in Figure 4.2(a) for coarse sand, the bubble still generates a recognisable asymmetric rebound attributable to a residual downward jet, but both the centroid displacement and the rebound radius are sensibly reduced compared to the rigid-wall sequence (d). For $0.6 < \gamma < 1.3$ a mound of sand develops beneath the bubble during the expansion phase and forces a conical collapse morphology; the mound acts as a compliant cushion that absorbs the rebound and reduces the rebound radius, eliminating the secondary collapse. In Figure 4.2(b) the medium-sand sequence at comparable γ shows this transition: the

rebound bubble is visibly smaller than in the rigid case and any conical vapour hull, the optical signature of a coherent microjet, is no longer discernible. For $\gamma < 0.6$ the bubble develops a bell shape, generates anomalously fast micro-jets (v_{jet} > 1000 m·s^{-1}) directed away from the boundary, and triggers granular jets from the sand surface. The progression across grain sizes is illustrated in Figure 4.2: in the rigid-wall case (d), the rebound in frames 5–6 is dominated by a conical vapour hull travelling toward the surface — the direct optical evidence of the downward microjet that pierces the bubble surface at collapse — which eventually disintegrates into a ring of secondary microbubbles visible in frame 6.

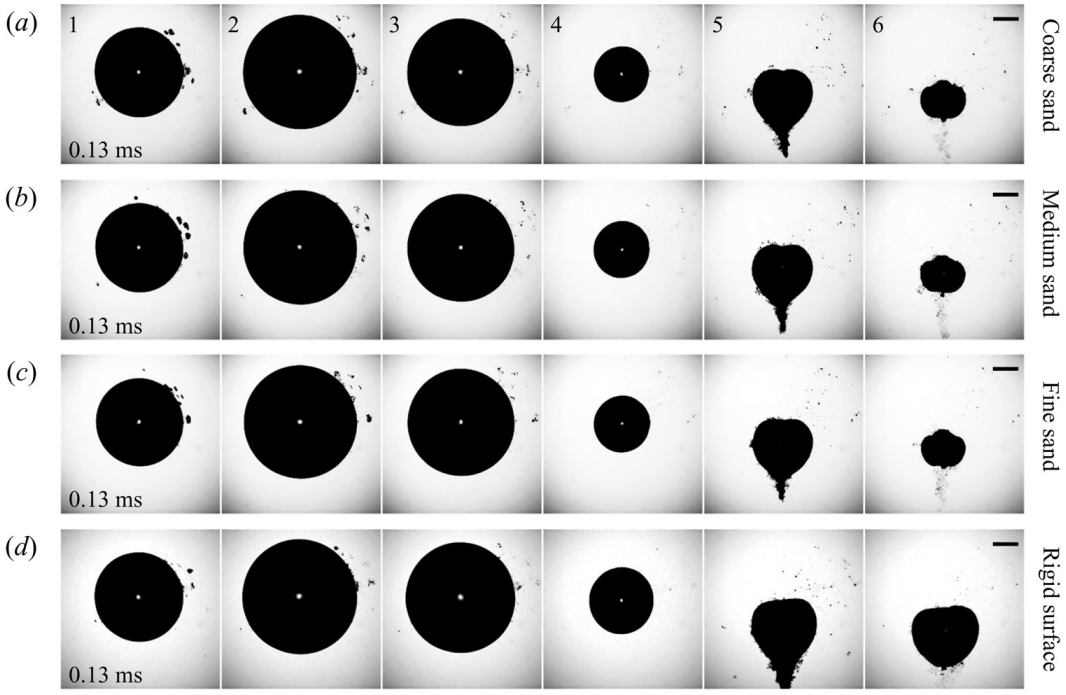

Figure 4.2: Selected instants of the bubble dynamics near the different investigated boundaries at $\gamma \approx 2.6$:(a) coarse sand (dg = 350μm), (b) medium sand (dg = 200μm), (c) fine sand (dg = 90μm) and (d) rigid boundary. All image sequences are initiated 0.13ms after the bubble generation and the time interval between successive images is 0.22 ms. The black line indicates the 2mm scale [53].

Crucially, the fine-sand sequence in Figure 4.2(c) at $\gamma \approx 2.6$ — the case most relevant to the espresso bed geometry, given that espresso fines ($d_2 \approx 26$ μm) are finer than the smallest granularity tested by Sieber et al. (90 μm), so that suppression effects are expected to be at least as pronounced — shows a conical vapour hull and a secondary rebound that are both measurably reduced relative to the rigid-wall case (d), consistent with the shorter oscillation period and smaller centroid displacement documented for all granular boundaries at $\gamma > 1.3$. At smaller stand-off distances,

which are more representative of inter-particle bubble nucleation within the compacted bed, the granular boundary swallows the bubble in the final instants of collapse, so that the resulting microjet energy — despite reaching velocities between 1083 and 1138 m/s near fine sand at $\gamma \approx 0.5$ —is dissipated inside the granular medium rather that delivered as an impulsive pressure load to a rigid surface. This is the reason why in the presence of granular geometry, the effects of inertial cavitation cannot be comparable to those affecting a rigid-walled system in free-suspension studies.

4.2.3.2. Void-Fraction Attenuation of Collapse Anisotropy

Andrews, Fernández Rivas & Peters [54] addressed the complementary problem: the collapse of laser-induced bubbles near rigid porous plates of controlled void fraction φ, ranging experimentally from non-porous, $\varphi = 0$, to $\varphi = 59.4$ %, with $\varphi = 1$ representing the theoretical limit of zero anisotropy inside the numerical model. Using fixed plates rather than granular beds, this study isolated the pure geometric effect of boundary porosity on failure behaviour, independent of grain mobility and cohesion. The primary observables, the normalised bubble displacement at collapse (how far the bubble centroid migrates toward the plate before collapsing, normalised by its maximum radius) and the rebound size ratio (how large the bubble is when it re-expands after the first collapse, as a fraction of its original size), carry a direct physical meaning : a large displacement means the bubble is hardly pulled toward the surface and will generate a coherent microjet upon collapse, while a large rebound ratio translate into a large quantity of energy surviving the first collapse and available for a damaging secondary event. Andrews et al. showed that both displacement and rebound radius depend deeply on standoff distance γ and decrease uniformly with increasing void fraction φ, with the gradient remaining essentially constant across all void fractions. The central finding is that, for plates with dimensionless tessellation area $A < 1.5$ or hole size $W/R_0 < 1$, the shape and size of the holes become negligible, and displacement and rebound radius each collapse onto single curves when plotted against ζ — with the collapse being particularly clean when ζ is estimated by fitting displacement data to the non-porous plate reference curve. The observables were shown to depend on γ and φ, and when expressed through the anisotropy coefficient ζ, they each fall onto single universal curves independent of pore geometry and size. Figure 4.3 shows these results. All four panels share ζ as the abscissa, but ζ is computed in two different ways: in panels (a) and (b), it is predicted by the boundary-element numerical model, whereas in panels (c) and (d), it is estimated by fitting the displacement data to the non-porous plate curve. In both cases the data, coloured by φ and spanning all hole shapes and sizes, converge onto single master curves for Δ/R_0 (a, c) and R_1/R_0 (b, d). The collapse is particularly clean in (c) and (d), where the grey

background points from Andrews & Peters (2022) and the colour data all lie on the same trend; in panel (d) the Supponen et al. (2018) rigid-wall rebound correlation differs from the porous-plate data, though Andrews et al. note that differences among experimental methodologies may additionally contribute to this variation. Panel (c) also shows the two fitted power-law correlations $\Delta/R_0 = 8.72\zeta^{0.70}$ (dashed) and $\Delta/R_0 = 4.54\zeta^{0.51}$ (dot-dash), which link the data nearly across three decades of ζ.

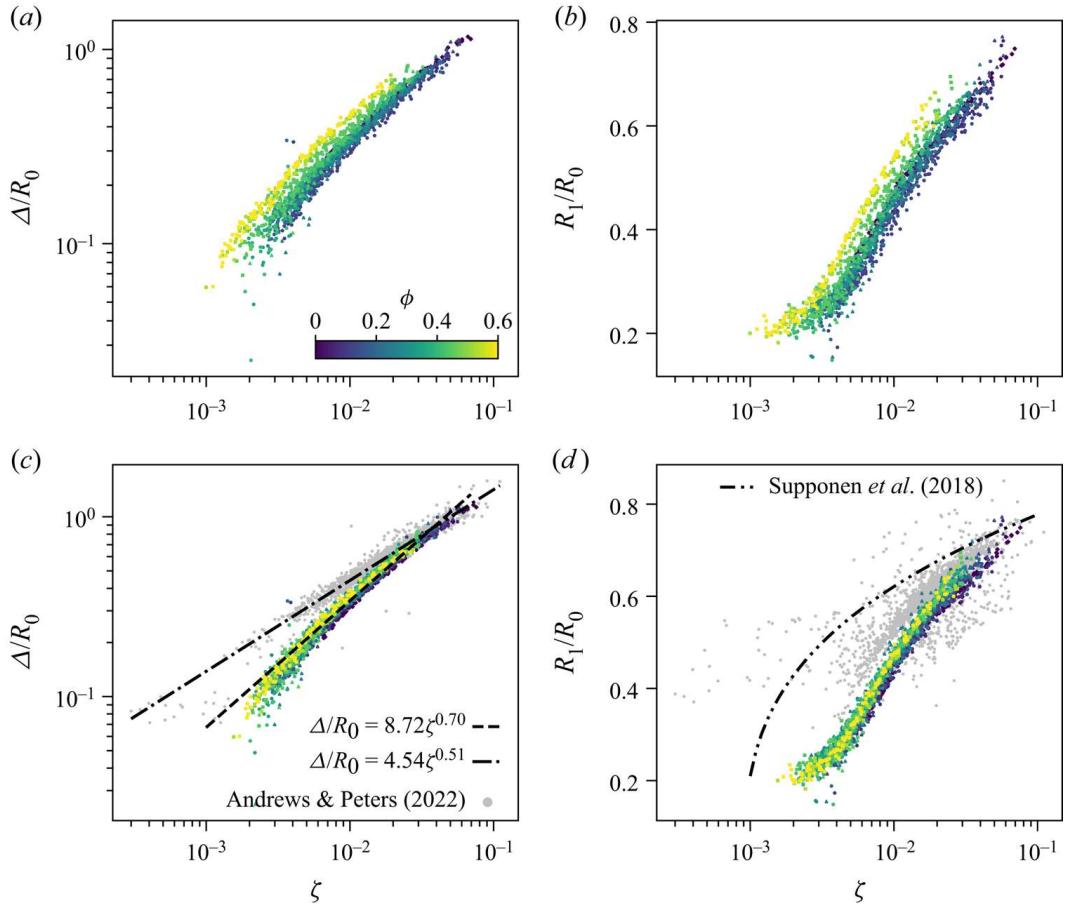

Figure 4.3: (a) Normalised displacement and (b) rebound radius ratio plotted against the anisotropy parameter magnitude ζ predicted by the numerical model. (c) Normalised displacement and (d) rebound radius ratio plotted against the anisotropy parameter magnitude ζ estimated by fitting displacement data to the non-porous plate data. Data are coloured by void fraction φ. The grey data points in (c) and (d) are from Andrews & Peters (2022) The black dashed line is a curve fit to the porous plates data. The black dash-dotted line is the curve fit from Andrews & Peters (2022). The black dash-dot-dotted line is derived from the curve fit of Supponen et al. (2018) [54].

The anisotropy coefficient was extended to porous boundaries through:

$$\zeta = g(\varphi)\,\gamma{-}2 \tag{4.2.1}$$

where the term g(φ) decreases monotonically from g (0) = 0.195 (non-porous plate, the classical rigid-wall result) to g (1) = 0 (fully open boundary). The gradient of g(φ) is steepest at low void fractions, so even modest porosity produces a disproportionate reduction in ζ and hence in the energy available for microjet formation. Applying equation (5.4) from Andrews et al. paper, with φ = 0.18 gives $g(0.18) = 0.195(1 - 0.18^{0.5}) \approx 0.112$, compared with g(0) = 0.195 for a non-porous plate — a reduction of approximately 43% at fixed γ, placing the operating point essentially below the rigid-wall measurement, confirming quantitatively that collapse anisotropy is substantially attenuated in the espresso bed geometry. The evidence obtained in this paper, coupled with the Sieber et al. finding that granular boundaries absorb collapse power, supports the exclusion of inertial cavitation as a possible enhancement mechanism in the UAE system analysed in this work. Acoustic streaming, which requires no bubble nucleation and scales directly with bed permeability through the Brinkman relation, is therefore the sole mechanistically consistent acoustic enhancement mechanism in this geometry.

4.3. Model Subdivision

The model used for ultrasound propagation in porous media saturated with fluid is Biot's poroelastic theory. This, coupled with solid mechanics for the steel basket, generates the acoustic variables field. Acoustic streaming, as already described in Chapter 1 and 2, generates from the acoustic velocity field, originating a volumetric force. Said force is then used as input to simplified Brinkman equations for fluid flow in porous media to determine the streaming velocity. Axial velocity is determined using Darcy's porous flow model. A convection-diffusion model is then developed to evaluate solutes extraction. When the ultrasonic horn is applied, both axial and streaming velocity contribute to the mass transfer parameter. The sequential structure of the model, with its two sub-problems and the unidirectional coupling from the acoustic field to the extraction model, is represented in Figure 4.4. The two sub-problems are solved independently: the acoustic-poroelastic model, generation of volumetric force and acoustic streaming porous flow in COMSOL Multiphysics® and the extraction model in MATLAB®.

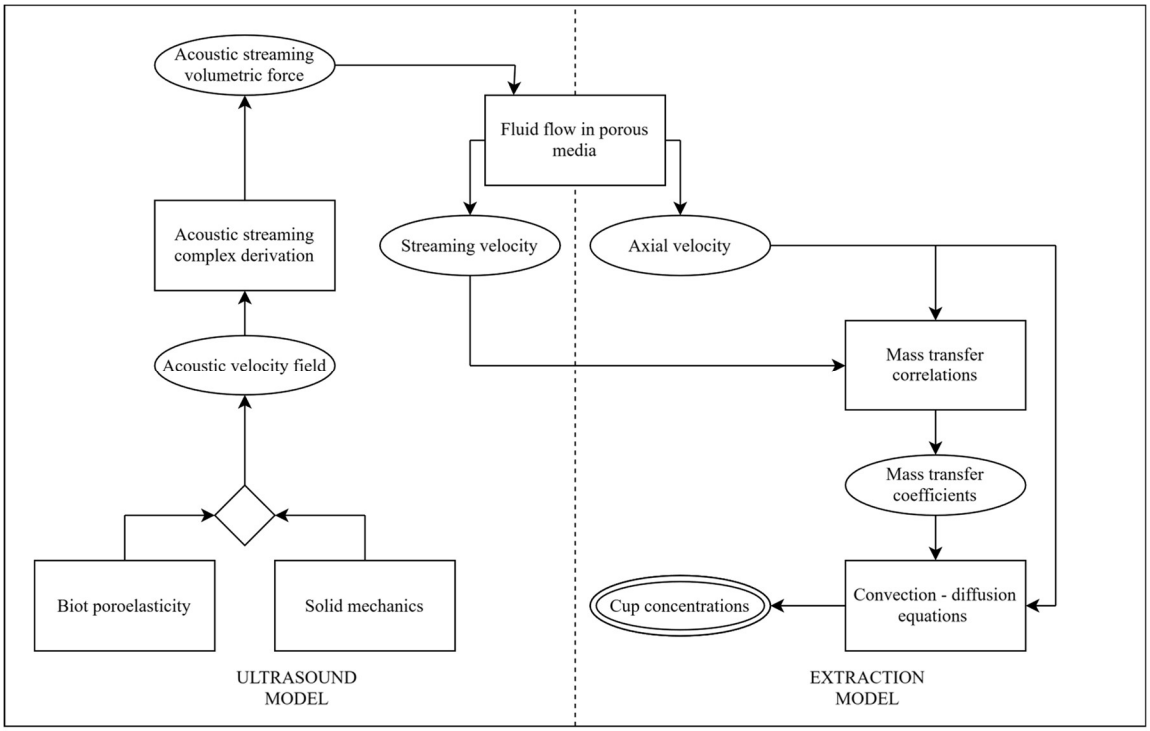

Figure 4.4: Model flowchart

4.4. Initial Considerations

This section collects equations and correlations that recur throughout the analysis of the ultrasonic acoustic field. They are reported here for convenience and will be referenced in the following chapters whenever required, avoiding unnecessary repetition.

4.4.1. Reynolds Decomposition

Reynolds decomposition is a fundamental tool for ultrasound modelling. Instantaneous flow properties, such as velocity and pressure, can be decomposed into time average and fluctuating components. Using u as a generic variable:

$$u = \bar{u} + u' \tag{4.4.1}$$

With $\bar{u}$ being the time average and u' being the first-order fluctuation. In this work all acoustic properties are oscillating with respect to the average underlying non-sonicated stationary value thus having the same nature of u'.

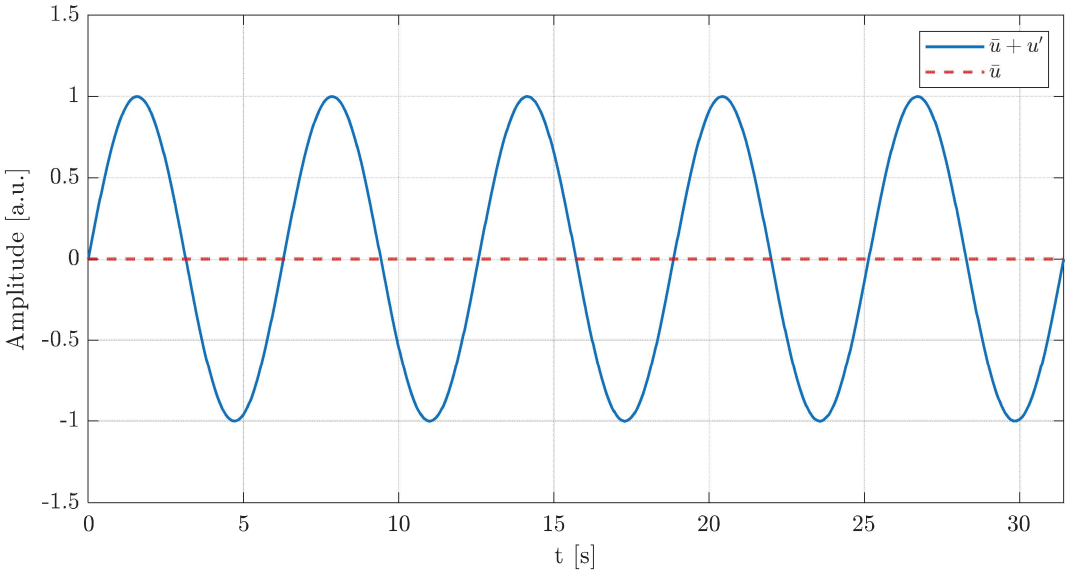

Figure 4.5: Representation of the Reynolds decomposition of a sine wave

4.4.2. Frequency Domain

Since the system operates at a fixed frequency originally imposed by the sonicator, acoustic and mechanical fields can be treated as time-harmonic quantities. In this way all oscillating variables reach a steady periodic regime characterized by the same angular frequency ω $[rad/s]$ imposed originally by the transducer. With a being a generic variable:

$$\omega = 2\pi f \tag{4.4.2}$$

$$a(x,t) = a(x)e^{i\omega t} \tag{4.4.3}$$

This complex number notation allows the representation of the real physic quantity, described by the real part and the signal phase information, carried by the imaginary part:

$$a(x)e^{i\omega t} = a(x)\cos(\omega t) + ia(x)sin(\omega t) \tag{4.4.4}$$

A fundamental property of time-harmonic quantities represented by sine waves is that the time-average of said quantity in the span of a wave period is zero:

$$\frac{1}{\mathrm{T}}\int_0^{\mathrm{T}} \cos(\omega t)dt = 0 \tag{4.4.5}$$

$$\frac{1}{\mathrm{T}}\int_0^{\mathrm{T}} \sin(\omega t)\,dt = 0 \tag{4.4.6}$$

Under the assumption of steady state (Subchapter 4.2.2 - b), the frequency domain formulation can be applied, transforming time derivatives into algebraic terms:

$$\frac{\partial a}{\partial t} = i\omega a(x)e^{i\omega t} \tag{4.4.7}$$

$$\frac{\partial^2 a}{\partial t^2} = -\omega^2 a(x)e^{i\omega t} \tag{4.4.8}$$

4.4.3. Stress Tensor Definition

For both the porous matrix and the steel basket, mechanical deformations can be represented by the strain tensor $\varepsilon(u)$ (second order), representing both normal and shear deformations:

$$\varepsilon(u) = \frac{1}{2}(\nabla u + (\nabla u)^{T}) - \varepsilon_0 \tag{4.4.9}$$

Where, u is the displacement vector field and ε_0 is a possible initial strain, which from now on will be assumed as zero.

Remembering the assumption of linear elastic materials (Subchapter 4.2.2 - c), the stress tensor is related to the strain tensor by Hooke's law:

$$\sigma = c_{el} : \varepsilon(u) \tag{4.4.10}$$

The term c_{el} is the tensor (fourth order) containing the elastic properties of the material, while : stands for the double-dot product between the two terms (Appendix A, 9). Under the assumption of isotropic elastic material (Subchapter 4.2.2 - c), c_{el} can be represented in Voigt notation by the following 6 × 6matrix [58]:

$$c_{el} = \frac{E}{(1+\upsilon)(1-2\upsilon)}\begin{bmatrix} 1-\upsilon & \upsilon & \upsilon & 0 & 0 & 0 \\ \upsilon & 1-\upsilon & \upsilon & 0 & 0 & 0 \\ \upsilon & \upsilon & 1-\upsilon & 0 & 0 & 0 \\ 0 & 0 & 0 & \frac{1-2\upsilon}{2} & 0 & 0 \\ 0 & 0 & 0 & 0 & \frac{1-2\upsilon}{2} & 0 \\ 0 & 0 & 0 & 0 & 0 & \frac{1-2\upsilon}{2} \end{bmatrix} \tag{4.4.11}$$

Where, E and υ are the material's Young's elastic modulus and Poisson's ratio respectively.

4.5. Porous Flow Model and Bed Properties

4.5.1. Brinkman Equations

For a porous bed, fluid flow is described by Brinkman's continuity (first equation) and momentum (second equation) equations [63]:

$$\frac{\partial}{\partial t}(\phi\rho_f) + \nabla\cdot(\rho_f v) = Q_m \tag{4.5.1}$$

$$\frac{\rho_f}{\phi}\left(\frac{\partial v}{\partial t} + (v\cdot\nabla)\frac{v}{\phi}\right) =$$

$$= -\nabla p + \nabla\cdot\left[\frac{1}{\phi}\left\{\mu_f(\nabla v + (\nabla v)^T) - \frac{2}{3}\mu_f(\nabla\cdot v)I\right\}\right] - \left(\frac{\mu_f}{k} + \frac{Q_m}{\phi^2}\right)v + \mathbb{f} \tag{4.5.2}$$

Where, v is the resulting superficial fluid velocity field, ϕ is the bed porosity, ρ_f is the fluid density, μ_f is the fluid's dynamic viscosity, p is the fluid pressure, k is the granular bed's permeability, I is the identity matrix, Q_m is an internal mass source/sink term and $\mathbb{f}$ is an external volumetric force.

At steady state (Subchapter 4.2.2 - b) all time derivatives are neglected:

$$\frac{\partial}{\partial t}(\phi\rho_f) = 0 \tag{4.5.3}$$

$$\frac{\partial v}{\partial t} = 0 \tag{4.5.4}$$

In this model the extracted mass is negligible when compared to the water mass:

$$Q_m = 0 \tag{4.5.5}$$

For an incompressible fluid (Subchapter 4.2.2 - e) the continuity equation then becomes:

$$\rho_f\nabla\cdot v = Q_m \tag{4.5.6}$$

$$\nabla\cdot v = 0 \tag{4.5.7}$$

In a system where viscous forces predominate (Subchapter 4.2.2 - d) the inertial term can be neglected:

$$(v\cdot\nabla)\frac{v}{\phi} = 0 \tag{4.5.8}$$

The final momentum equation is:

$$-\nabla p + \nabla\cdot\left[\frac{1}{\phi}\{\mu_f(\nabla v + (\nabla v)^T)\}\right] - \left(\frac{\mu_f}{k}\right)v + \mathbb{f} = 0 \tag{4.5.9}$$

4.5.2. Darcy Equation

In the more specific case of non-sonicated coffee extraction, the 1D model (Subchapter 4.2.2 - j) requires the linearized form of Darcy's law along the z-axis [33]:

$$v_{ax} = \frac{k}{\mu_f}\frac{\Delta p}{L} \tag{4.5.10}$$

Where, Δp is the pressure difference between the inlet and the outlet of the column and L is the height of the column.

In this case, the Forchheimer extension reported in Subchapter 2.4, the addition of a quadratic term representing a non-linear pressure-velocity behaviour, is not considered. This is a consequence of the fact that, at pore-scale, the Reynolds numbers in classical espresso extraction are well underneath the Darcy-valid regime, with values in the range of 10^{-2} to 10^{-1} as confirmed by Corrochano et.al. [30]. Mo et al.[19], in their paper, document a Forchheimer inertial effect, but only at the highest espresso pressure ratios. These conditions represent an upper limit on operating range; in fact, among most coffee extractions, Darcy's law is the sole one widely used. The reported limit for the exclusion of inertial terms of pore Reynolds number is $Re_P < 10$ [84].

4.5.3. Permeability and Tortuosity Coefficients

One of the most important parameters to describe fluid flow in porous media is the permeability k, the measure of the capability of allowing porous fluid flow under an applied pressure gradient in a porous bed.

The standard Kozeny-Carman formulation assumes a packed bed of all equal, uncompressed particles. Indeed, this equation does not include, in its theory, the bimodal particle-size distribution characteristic of ground coffee, or the decrease in porosity induced by axial compression during brewing. Also, Corrochano et al. [30] demonstrate that the basic equation was inadequate for calculating the hydraulic resistance of coffee beds, resulting in errors of up to 300%. These are the main reasons why, for consolidated coffee beds, Vaca Guerra, M. et al. derived the following correlation as a modified Kozeny-Carman equation [33]:

$$k = \frac{(\psi d_{3,2})^2 \phi^{4.3} \beta_{coarse}^{0.43}}{72\lambda_p^2(1-\phi)^2} \tag{4.5.11}$$

Where, ψ is the particle sphericity, $d_{3,2}$ is the Sauter diameter of the distribution, β_{coarse} is the Rosin-Rammler beta parameter for the coarse part and λ_p is an empiric parameter with value of 7.5.

Tortuosity is another key parameter for porous media flow which does not appear explicitly in the permeability correlation shown before. It measures the fraction difference between the length of the actual flow through the pore network of the coffee bed and the total length of the bed geometry and can be found with an empirical correlation for tightly packed beds, where [30]:

$$\tau = \left(\frac{1}{\phi}\right)^{0.5} \tag{4.5.12}$$

It affects the model in the formulation that leads from the superficial velocity of Darcy's law to that in the real flow through the channels' pores.

4.6. Extraction Model

4.6.1. Governing Equations

In the extraction model the derivation of two mass transfer equations for both the solids and the liquid phase are required. Due to the bimodal nature of coffee grind highlighted in Section 3, solids equations for both coarse and fine parts will be developed. The model is based on a mono-dimensional assumption as stated in Subchapter 4.2.2 - j.

Starting from the solid phase the balance equation for a generic particle size can be written as:

$$n_{part} V_{part} \frac{\partial q}{\partial t} = n_{part} A_{part} k_c (q_{sup} - q) \tag{4.6.1}$$

Where n_{part} is the number of selected particles, V_{part} is the particle volume, A_{part} is the particle surface area, k_c is the total mass transfer coefficient expressed in $[m/s]$, q and q_{sup} are the concentration in the bulk of the grain and the concentration on the surface boundary of the grain respectively, expressed in $\left[kg_{solute}/m^3_{coffee}\right]$.

The equation is independent of the number of particles as the two terms can be simplified out of the equation. The area-to-volume ratio is related to the particle diameter and sphericity:

$$a = \frac{A_{part}}{V_{part}} = \frac{6\psi}{d} \tag{4.6.2}$$

$$\frac{\partial q}{\partial t} = a k_c (q_{sup} - q) \tag{4.6.3}$$

On the liquid side the initial form of the balance equation can be written by considering a small longitudinal section $\Delta V = S\Delta z$ inside of the system and determining the inlets/outlets and the source/sink terms:

$$\phi S\Delta z\frac{C|_{t+\Delta t} - C|_t}{\Delta t} = -v_{ax}S(C|_{z+\Delta z} - C|_z) - (1-\phi)S\Delta z\left[ak_c\left(q_{sup} - q\right)\right] \quad (4.6.4)$$

Where, S is the surface normal to the z-axis, Δz is the considered height portion and C is the bulk liquid concentration expressed in $[kg_{solute}/m^3_{water}]$.

Fluid occupies only the ϕ fraction of the considered volume, while the solids occupy the $(1-\phi)$ fraction. The fluid enters in z and leaves in $z+\Delta z$, hence the minus sign in front of the convective first part of the right-hand side of the equation. The second part of the right-hand side of the equation is the volumetric source term.. Its sign is opposite to that in the solid-phase balance equation, reflecting the conservation of mass: any solute released by the solid phase is simultaneously transferred to the liquid phase.

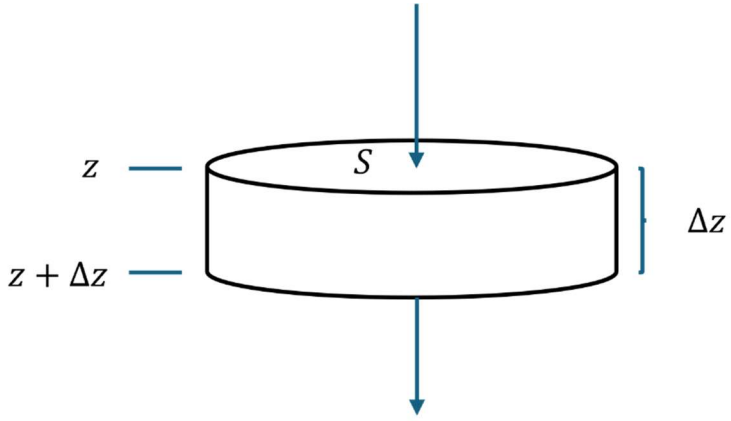

Figure 1.6: Small volume representation

The surface can then be simplified and the equation divided by Δz:

$$\phi\frac{C|_{t+\Delta t} - C|_t}{\Delta t} = -v_{ax}\left(\frac{C|_{z+\Delta z} - C|_z}{\Delta z}\right) - (1-\phi)\left[ak_c\left(q_{sup} - q\right)\right] \quad (4.6.5)$$

Setting the limits for $\Delta t,\ \Delta z \to 0$ the partial derivative equation is obtained:

$$\phi\frac{\partial C}{\partial t} = -v_{ax}\frac{\partial C}{\partial z} - (1-\phi)ak_c\left(q_{sup} - q\right) \quad (4.6.6)$$

To close the two equations with two incognita the equilibrium between the surface concentration and the fluid concentration must be used:

$$q_{sup} = \frac{C}{m} \quad (4.6.7)$$

The m equilibrium term is a volumetric partition term expressed in $[m^3_{coffee}/m^3_{water}]$. This is a linear equilibrium; a common simplification used for coffee extraction modelling [43].

Finally, the mass transfer equations can be generalized for any particle size partition by introducing the volume fraction of the considered i-partition $\theta_i = V_i / \sum V_i$

$$\frac{\partial q_i}{\partial t} = a_i k_{c,i}\left(\frac{C}{m} - q_i\right) \qquad \forall i \tag{4.6.8}$$

$$\phi \frac{\partial C}{\partial t} = -v_{ax}\frac{\partial C}{\partial z} - (1-\phi)\sum_i \theta_i a_i k_{c,i}\left(\frac{C}{m} - q_i\right) \tag{4.6.9}$$

4.6.2. Mass Transfer Coefficients

Mass transfer coefficient k_c is what determines the diffusion rate of the system. It can be seen as two separate parts in series: mass transfer inside of the particles and mass transfer inside of the bulk of the fluid. For a series of mass transfer coefficients,

$$\frac{1}{k_c} = \frac{1}{k_{external}} + \frac{1}{k_{internal}} \tag{4.6.10}$$

4.6.2.1. External Mass Transfer

The external coefficient can be retrieved from correlations for fluid flow inside of granular columns. Clusser E. L. reports the following formula [16]:

$$k_{external} = 0.0051\left(\frac{v}{a\nu_f}\right)^{0.67}\left(\frac{\mathcal{D}}{\nu_f}\right)^{0.5}(ad)^{0.4}\left(\frac{1}{\nu_f g}\right)^{-\frac{1}{3}} \tag{4.6.11}$$

Where, v is the total superficial velocity inside the column, ν_f is the kinematic viscosity of the fluid, d is the particle diameter, g is the gravitational acceleration and $\mathcal{D}$ is the chemical diffusivity of the solute in the free fluid.

4.6.2.2. Internal Mass Transfer

Internal mass transfer can be modeled through the diffusion equation inside a sphere:

$$\frac{\partial q}{\partial t} = \frac{\mathcal{D}}{r^2}\frac{\partial}{\partial r}\left(r^2\frac{\partial q}{\partial r}\right) \tag{4.6.12}$$

The initial, symmetry and boundary conditions are:

$$q|_{t=0} = q_0 \qquad \frac{\partial q}{\partial r}|_{r=0} = 0 \qquad q|_{r=R} = q^*$$

Alopaeus, V. [67] proposed a polynomial approximation of the exact solution to this problem for a fluid sphere with immobile surface. The equations stay the same for a solid particle, with the only difference being that the considered diffusivity should be corrected to account for intra-particle porosity, intra-particle tortuosity and solute dimensions with respect to the intra-particle pore size. All of this is condensed into what is called the 'hindrance factor' h:

$$\mathcal{D}_{eff} = \frac{\mathcal{D}}{h} \tag{4.6.13}$$

The polynomial approximation is based on the definition of the Fourier number, already used by the exact solution:

$$Fo = \frac{\mathcal{D}_{eff} t}{r^2} \tag{4.6.14}$$

As already mentioned, the solution is conceived for spherical fluid particles, so a Sherwood number is introduced. For the solids case it works as a correction to the lumped model which would assume $k_{internal} = \mathcal{D}_{eff}/d$. During diffusion, concentration gradients develop inside the particle, and the actual mass transfer rate differs from this simplified estimate. The Sherwood number accounts for these transient intra-particle concentration gradients, providing a correction factor that allows the diffusion equation solution to be represented by an equivalent mass transfer coefficient.

$$k_{internal} = Sh \frac{\mathcal{D}_{eff}}{d} \tag{4.6.15}$$

The proposed polynomial solution is:

$$Sh = \frac{a_0}{\sqrt{\pi Fo}} + \frac{a_1\sqrt{Fo} + a_2 Fo + \frac{2\pi^2}{3} a_5 Fo^{1.5}}{1 + a_3\sqrt{Fo} + a_4 Fo + a_5 Fo^{1.5}} \tag{4.6.16}$$

Where:

$$a_0 = 2, \quad a_1 = 117.346, \quad a_2 = 39.696, \quad a_3 = 62.166, \quad a_4 = 31.169, \quad a_5 = 337.258$$

4.6.3. Initial Conditions

The initial conditions must reflect the assumption made in Subchapter 4.2.2 - g about the absence of pre-infusion phase. Initially water has not extracted solutes from the coffee, so:

$$C|_{t=0} = 0 \tag{4.6.17}$$

$$q_i|_{t=0} = \rho_{bean}\, \Gamma_0 \tag{4.6.18}$$

Where Γ_0 is the initial mass fraction of solute inside of the bean expressed in $[kg_{solute}/kg_{bean}]$, while ρ_{bean} is the effective bean density, dependent on the solid density and intra-particle porosity:

$$\rho_{bean} = \rho_{intrinsic}(1 - \phi_{intra}) \tag{4.6.19}$$

4.6.4. Boundary Conditions

The boundary condition imposed on the extraction model is straightforward: the inlet fluid must be water with no coffee extracts present.

$$C|_{z=0} = 0 \tag{4.6.20}$$

4.6.5. Cup Concentration

The scope of the extraction model is to determine the final cup concentration of solute. The mass exiting the system, passing through the bed outlet $z = L$, and accumulating in the cup over the extraction period can be defined as:

$$m_{cup} = v_{ax} S \int_0^{t_{tot}} C(t, z = L)\, dt \tag{4.6.21}$$

The total volume of fluid collected (at axial velocity v_{ax} over cross-section S for time t_{tot}) and the resulting cup concentration are:

$$V_{cup} = v_{ax} S t_{tot} \tag{4.6.22}$$

$$C_{cup} = \frac{\int_0^{t_{tot}} C(t, z = L)\, dt}{t_{tot}} \tag{4.6.23}$$

4.7. Ultrasound Model

4.7.1. Biot Poroelastic Theory

Biot developed his theory for modelling the mechanical and acoustical behaviour of poroelastic materials between 1956 and 1962 [79], with the main assumption of homogeneous porous media (Subchapter 4.2.2 - a). A poroelastic material is defined as a solid porous matrix filled with a fluid; its distinctive feature is the bidirectional coupling between the solid skeleton's deformation and the pore-fluid pressure, which enhances the wave propagation behaviour in ways that are essentially different from those of a single-phase elastic solid.

In normal media the sound travels as a single longitudinal compressional P-wave (P standing for Primary). Biot predicted the existence of a second, slower P-wave in 1956, and its observation was confirmed experimentally only in 1980 [76]. The fast and slow waves are called P1 and P2 waves respectively and correspond to the cases

when the porous matrix and the fluid are nearly in or out of phase. In the first case, the solid frame and pore fluid move together in the same direction (phase difference of 0°), and the wave behaves like a standard sound wave in a linear elastic solid. In the second case, the fluid essentially gets squeezed back and forth relative to the moving solid skeleton (phase cancelation, difference of 180°). This motion creates high viscous drag, making the slow wave travel much slower and heavily attenuating it, to the point that it is observable only in highly permeable media or at very low frequencies.

4.7.1.1. Biot Wave Equations: Solid and Fluid Displacement Formulation

The Biot poroelastic formulation describes the dynamic behaviour of a fluid-saturated porous medium by treating the solid skeleton and the pore fluid as two interpenetrating continua. The governing equations are obtained by applying the balance of linear momentum separately to the solid matrix (first equation) and to the fluid phase (second equation), while accounting for their interaction through viscous drag, pressure coupling, and inertial effects. The key variables are the displacement of the porous matrix u and the displacement of the fluid with respect to the porous matrix w.

$$\rho_{av}\frac{\partial^2}{\partial t^2}u + \rho_f\frac{\partial^2}{\partial t^2}w - \nabla\cdot\sigma = 0 \tag{4.7.1}$$

$$\rho_f\frac{\partial^2}{\partial t^2}u + \frac{\mu_f}{k}\frac{\partial}{\partial t}w + \frac{\tau}{\phi}\rho_f\frac{\partial^2}{\partial t^2}w + \nabla p_f = 0 \tag{4.7.2}$$

Where τ is the bed tortuosity, p_f is the fluid pressure, σ is the stress tensor of the poroelastic material and ρ_{av} is the porosity-weighted average of the solid and fluid densities:

$$\rho_{av} = \rho_{bean}(1-\phi) + \rho_f\phi \tag{4.7.3}$$

The frequency domain can be applied to the Biot's equations as discussed in Subchapter 4.4.1:

$$-\rho_{av}\omega^2 u - \rho_f\omega^2 w - \nabla\cdot\sigma = 0 \tag{4.7.4}$$

$$-\rho_f\omega^2 u - \omega^2\rho_c(\omega)w + \nabla p_f = 0 \tag{4.7.5}$$

With ρ_c being defined as a complex density which accounts for the presence of the solid matrix, considering porosity, tortuosity and viscous drag:

$$\rho_c(\omega) = \frac{\tau}{\phi}\rho_f + \frac{\mu_f}{i\omega k} \tag{4.7.6}$$

At low frequencies the velocity profile inside of the pores is Poiseuille-like [57]. At high frequencies a correction must be introduced but first the separation between the high and low frequency regime must be set.

A reference frequency f_R that determines the limit between the low frequency range ($f \ll f_R$) and the high frequency range ($f \gg f_R$) can be introduced. It is determined by observing that the transition between the two ranges happens when the viscous forces equal the inertial ones. This happens when the viscous penetration is equal to the radius of the pore [57]:

$$\delta_v = \sqrt{\frac{\mu_f}{2\pi f_R \rho_f}} = r_{pore} \tag{4.7.7}$$

In the actual system, with assumption made in Section 5-f, the hydraulic pore radius is [56, 79]:

$$r_H = \sqrt{\frac{2\tau k}{\phi}} \tag{4.7.8}$$

$$r_{pore} = 2r_H \tag{4.7.9}$$

The correction to the fluid viscosity originally introduced by Biot is [57] :

$$\mu_c(f) = \mu_f F_c\left(\sqrt{\frac{f}{f_R}}\right) \tag{4.7.10}$$

Where the function F_c is defined as:

$$F_c(\varphi) = \frac{1}{4}\left(\frac{\varphi T(\varphi)}{1 + 2iT(\varphi)/\varphi}\right) \tag{4.7.11}$$

Where, $T(\varphi)$ is related to the Kelvin functions $Ber(\varphi)$ and $Bei(\varphi)$:

$$T(\varphi) = \frac{Ber'(\varphi) + iBei(\varphi)}{Ber(\varphi) + iBei(\varphi)} \tag{4.7.12}$$

$$T(\varphi) = \frac{-\sqrt{-i}\, J_1(\sqrt{-i}\varphi)}{J_0(\sqrt{-i}\varphi)} \tag{4.7.13}$$

Where, J_1 and J_0 are Bessel functions of the first kind.

Finally, the stress tensor of the poroelastic material is:

$$\sigma(u, p_f) = \sigma_d(u) - \alpha_B p_f I \tag{4.7.14}$$

Where $\sigma_d(u)$ is the drained matrix stress tensor and α_B is the Biot-Willis coefficient.

$$\alpha_B = 1 - \frac{K_d}{K_s} \tag{4.7.15}$$

K_d is the drained matrix bulk modulus while K_s is the solid's bulk modulus.

The identity matrix I appears because the normal stress associated with the fluid pressure is isotropic. Pressure does not generate shear stress.

4.7.1.2. Reduction to u, p_f Formulation

This section could be already completed but from a numerical viewpoint it is better to convert the u, w system into a u, p_f system [57]. Although the original Biot formulation is expressed in terms of the solid displacement u and the relative fluid displacement w, this representation is not the most convenient from a numerical standpoint. Both u and w are vector quantities, meaning that in a three-dimensional finite element model each node has six unknown displacement components. For this reason, using a mixed displacement–pressure formulation in which the relative fluid displacement is replaced by the pore pressure is much more convenient. Since p_f is a scalar variable, the number of unknowns per node is reduced from six to four in three-dimensional problems. Mathematically, the transformation is possible because the second Biot equation $eq.$ (4.7.5) provides an explicit relation between u, w, and the pressure gradient. Therefore, w does not need to be treated as an independent unknown and can be eliminated from the governing equations.

The relative fluid displacement w can be extracted from $eq.$ (4.7.5):

$$w = \frac{1}{\omega^2 \rho_c(\omega)} \left(\nabla p_f - \rho_f \omega^2 u \right) \tag{4.7.16}$$

Feeding back $eq.$ (9.1.1.16) into $eq.$ (9.1.1.1):

$$-\rho_{av}\omega^2 u - \frac{\rho_f}{\rho_c(\omega)} \left(\nabla p_f - \rho_f \omega^2 u \right) - \nabla \cdot \sigma = 0 \tag{4.7.17}$$

Substituting the stress tensor and rearranging:

$$-\left(\rho_{av} - \frac{\rho_f^2}{\rho_c(\omega)} \right) \omega^2 u - \nabla \cdot \left(\sigma_d(u) - \alpha_B p_f I \right) = \frac{\rho_f}{\rho_c(\omega)} \nabla p_f \tag{4.7.18}$$

The next step is to divide $eq.$ (4.7.5) and take its divergence:

$$\omega^2 \nabla \cdot \left(\frac{\rho_f}{\rho_c(\omega)} u \right) + \omega^2 \nabla \cdot w + \nabla \cdot \left(-\frac{1}{\rho_c(\omega)} \right) \nabla p_f = 0 \tag{4.7.19}$$

Now a key parameter is introduced, Biot's modulus M, defined as:

$$\frac{1}{M} = \phi \mathcal{X}_f + \frac{\alpha_B - \phi}{K_d} (1 - \alpha_B) \tag{4.7.20}$$

Where $\mathcal{X}_f$ is the fluid's compressibility. For an incompressible fluid such as water, (Subchapter 4.2.2 - e), $\mathcal{X}_f = 0$. It can however be defined as:

$$\mathcal{X}_f = \frac{1}{\rho_f c_f^2} \tag{4.7.21}$$

With c_f being the sound speed in the considered fluid.

Combining the expressions for the volumetric strain $\varepsilon_{vol} = tr(\varepsilon) = \nabla \cdot u$ (Appendix A, 4) and fluid displacement w:

$$-\nabla \cdot w = \frac{p_f}{M} + \alpha_B \varepsilon_{vol} \tag{4.7.22}$$

$Eq.$ (4.7.19) becomes:

$$\omega^2 \nabla \cdot \left(\frac{\rho_f}{\rho_c(\omega)} u\right) - \omega^2 \left(\frac{1}{M} p_f + \alpha_B \varepsilon_{vol}\right) + \nabla \cdot \left(-\frac{1}{\rho_c(\omega)}\right) \nabla p_f = 0 \tag{4.7.23}$$

Finally, the two Biot's equations in u, p_f form, which will be the ones used in this work are:

$$-\omega^2 \left(\rho_{av} - \frac{\rho_f^2}{\rho_c(\omega)}\right) u - \nabla \cdot \left(\sigma_d(u) - \alpha_B p_f I\right) = \frac{\rho_f}{\rho_c(\omega)} \nabla p_f \tag{4.7.24}$$

$$-\frac{\omega^2}{M} p_f + \nabla \cdot -\frac{1}{\rho_c(\omega)} \left(\nabla p_f - \omega^2 \rho_f u\right) = \omega^2 \alpha_B \varepsilon_{vol} \tag{4.7.25}$$

4.7.1.3. Biot P-wave speeds

The first thing to do to derive P1 and P2 wave speeds from Biot's equations is to define the divergence of the stress tensor found in $eq.$ (4.7.14) for a longitudinal P-wave.

$$\nabla \cdot \sigma = \nabla \cdot \sigma_d - \nabla \cdot \left(\alpha_B p_f I\right) \tag{4.7.26}$$

For linear elastic isotropic material, which is the dry porous matrix,

$$\sigma_d = 2\mu\varepsilon + \lambda tr(\varepsilon) I \tag{4.7.27}$$

Where, λ and μ are the Lamé elastic parameters, derived from the dry matrix elastic bulk and shear moduli [58]:

$$\lambda = K_d - \frac{2G_d}{3} \tag{4.7.28}$$

$$\mu = G_d \tag{4.7.29}$$

With $tr(\varepsilon)$ being a scalar (Appendix A, 1) and constant Lamé parameters, the divergence of the drained stress tensor becomes (Appendix A, 2):

$$\nabla \cdot \sigma_d = 2\mu \nabla \cdot \varepsilon + \lambda \nabla \left(tr(\varepsilon)\right) \tag{4.7.30}$$

The divergence of the strain tensor $eq.$ (4.4.5) is (Appendix A, 3):

$$\nabla \cdot \varepsilon = \frac{1}{2}\left(\nabla^2 u + \nabla(\nabla \cdot u)\right) \tag{4.7.31}$$

The first term in $eq.$ (4.7.30) becomes:

$$2\mu\nabla \cdot \varepsilon = \mu\nabla^2 u + \mu\nabla(\nabla \cdot u) \tag{4.7.32}$$

The second term in $eq.$ (4.7.30) becomes (Appendix A, 4):

$$\lambda\nabla\big(tr(\varepsilon)\big) = \lambda\nabla(\nabla \cdot u) \tag{4.7.33}$$

Substituting into the drained stress tensor,

$$\nabla \cdot \sigma_d = \mu\nabla^2 u + (\mu + \lambda)\nabla(\nabla \cdot u) \tag{4.7.34}$$

A longitudinal plane wave is irrotational as it expands and compresses in the same direction as propagation, so the rotor of the displacement must be zero:

$$\nabla \times u = 0 \tag{4.7.35}$$

The drained term finally becomes (Appendix A, 5):

$$\nabla^2 u = \nabla(\nabla \cdot u) \tag{4.7.36}$$

$$\nabla \cdot \sigma_d = (2\mu + \lambda)\nabla(\nabla \cdot u) \tag{4.7.37}$$

The stress tensor for a longitudinal wave in poroelastic media is (Appendix A, 2):

$$\nabla \cdot \sigma = (2\mu + \lambda)\nabla(\nabla \cdot u) - \alpha_B \nabla p_f \tag{4.7.38}$$

The frequency domain treatment explained in Subchapter 4.1.1 can be extended to the spatial coordinates, to reduce spatial derivatives to algebraic formulations:

$$u(x,t) = Ue^{i(k_w x - \omega t)} \tag{4.7.39}$$

$$\frac{\partial}{\partial t} e^{i(kx-\omega t)} = -i\omega e^{i(k_w x - \omega t)} \tag{4.7.40}$$

$$\frac{\partial^2}{\partial t^2} e^{i(kx-\omega\ )} = -\omega^2 e^{i(k_w x - \omega t)} \tag{4.7.41}$$

$$\frac{\partial}{\partial x} e^{i(kx-\omega\ )} = ike^{i(k_w x - \omega t)} \tag{4.7.42}$$

In this context k_w $[rad/m]$ is the wave number, which is the spatial equivalent of ω. For a mono-dimensional wave:

$$\nabla \cdot u = \frac{\partial u}{\partial x} \tag{4.7.43}$$

$$\nabla(\nabla \cdot u) = \frac{\partial}{\partial x}\left(ikUe^{i(k_w x - \omega t)}\right) \tag{4.7.44}$$

$$\nabla(\nabla \cdot u) = -k_w^2 U \tag{4.7.45}$$

$Eq.$ (4.7.22) can then be used with the correlation found for longitudinal plane wave:

$$\nabla \cdot w = ik_w W \tag{4.7.46}$$

$$\nabla \cdot u = ik_w U \tag{4.7.47}$$

$$-ik_w W = \frac{p_f}{M} + \alpha_B ik_w U \tag{4.7.48}$$

$$p_f = -ik_w M(W + \alpha_B U) \tag{4.7.49}$$

From the previous equation the gradient of fluid pressure is extracted:

$$\nabla p_f = ik_w[-ik_w M(W + \alpha_B U)] \tag{4.7.50}$$

$$\nabla p_f = k_w^2 M(W + \alpha_B U) \tag{4.7.51}$$

The same rules apply to the stress tensor:

$$\nabla \cdot \sigma = (2\mu + \lambda)k_w^2 U - \alpha_B k_w^2 M(W + \alpha_B U) \tag{4.7.52}$$

The two Biot's equations $eq.$ (4.7.4) and $eq.$ (4.7.5) can be written as:

$$[(2\mu + \lambda + \alpha_B^2 M)k_w^2 - \rho_{av}\omega^2]U + \left[\alpha_B M k_w^2 - \rho_f \omega^2\right]W = 0 \tag{4.7.53}$$

$$\left[\alpha_B M k_w^2 - \rho_f \omega^2\right]U + [M k_w^2 - \rho_c \omega^2]W = 0 \tag{4.7.54}$$

Equation view can be simplified by introducing two new variables:

$$H = 2\mu + \lambda + \alpha_B^2 M \tag{4.7.55}$$

$$C = \alpha_B M \tag{4.7.56}$$

The matricial view of the derived system of equations is:

$$\begin{bmatrix} Hk_w^2 - \rho_{av}\omega^2 & Ck_w^2 - \rho_f \omega^2 \\ Ck_w^2 - \rho_f \omega^2 & Mk_w^2 - \rho_c \omega^2 \end{bmatrix} \begin{bmatrix} U \\ W \end{bmatrix} = 0 \tag{4.7.57}$$

To obtain non-trivial solutions the matrix determinant must be zero:

$$(Hk_w^2 - \rho_{av}\omega^2)(Mk_w^2 - \rho_c \omega^2) - \left(Ck_w^2 - \rho_f \omega^2\right)^2 = 0 \tag{4.7.58}$$

Sound speed c $[m/s]$ is finally introduced using the definitions of k which measures the number of wave cycles per unit distance and ω which measures the number of wave cycles per unit time:

$$c = \frac{\omega}{k_w} \tag{4.7.59}$$

$Eq.$ (4.7.58) is divided by k_w^4 to extract the squared wave speed:

$$(H - \rho_{av}c^2)(M - \rho_c c^2) - \left(C - \rho_f c^2\right)^2 = 0 \tag{4.7.60}$$

The resulting $Eq.$ (4.7.60) is a quadratic equation in c^2:

$$HM - H\rho_c c^2 - M\rho_{av}c^2 + \rho_{av}\rho_c c^4 - C^2 + 2C\rho_f c^2 - {\rho_f}^2 c^4 = 0 \tag{4.7.61}$$

$$\left(\rho_{av}\rho_c - {\rho_f}^2\right)c^4 - \left(H\rho_c + M\rho_{av} - 2C\rho_f\right)c^2 + (HM - C^2) = 0 \tag{4.7.62}$$

The final formula for the longitudinal wave speeds predicts a fast P1 wave, assigned to the + sign and a slow P2 wave, assigned to the − sign:

$$c^2 = \frac{\left(H\rho_c + M\rho_{av} - 2C\rho_f\right) \pm \sqrt{\left(H\rho_c + M\rho_{av} - 2C\rho_f\right)^2 - 4\left(\rho_{av}\rho_c - {\rho_f}^2\right)(HM - C^2)}}{2\left(\rho_{av}\rho_c - {\rho_f}^2\right)} \tag{4.7.63}$$

4.7.2. Acoustic Velocity

Acoustic velocity inside the fluid does not contribute to mass transfer: being a time-harmonic perturbation, its average on a period span is zero as explained in Subchapter 4.1.1, meaning that it does not contribute to the net solute transport. Its second-order effects, on the other hand, generate a steady acoustic streaming volumetric force so the actual value is needed. The interstitial acoustic fluid velocity amplitude can be derived from the time derivative in frequency domain of the relative fluid-solid displacement w, $Eq.$ (4.7.16):

$$v_{ac} = -\frac{\nabla p_f + (i\omega)^2\rho_f u}{i\omega\rho_c} \tag{4.7.64}$$

This acoustic velocity is a Darcy-like superficial velocity [73], the real acoustic velocity inside of the pores also known as seepage velocity can be defined as [74]:

$$\tilde{v} = -\left(\frac{\tau}{\phi}\right)\frac{\nabla p_f + (i\omega)^2\rho_f u}{i\omega\rho_c} \tag{4.7.65}$$

4.7.3. Solid Mechanics

The linear elastic equation is used to model the steel basket:

$$\rho_m \frac{\partial^2 u_m}{\partial t^2} = \nabla \cdot \sigma_m \tag{4.7.66}$$

Where, ρ_m, u_m and σ_m are the metal's density, displacement field and stress tensor respectively.

Using frequency domain, the equation then becomes:

$$-\rho_m\omega^2 u_m = \nabla \cdot \sigma_m \tag{4.7.67}$$

4.7.4. Linear Elastic Material's Wave Speeds

In linear elastic materials there are two types of sound waves: longitudinal (P) and shear (S). Both sound waves speeds can be calculated from the elastic properties of the material [27].

$$c_P = \sqrt{\frac{E(1-\nu)}{\rho(1-2\nu)(1+\nu)}} \tag{4.7.68}$$

$$c_S = \sqrt{\frac{E}{\rho(1+\upsilon)}} \tag{4.7.69}$$

4.7.5. Basket Boundary Conditions

On the boundary of the basket where the horn is applied, remembering the approximation of plane wave (Subchapter 4.2.2 - h), the peak pressure is calculated as [65]:

$$p_{peak} = \sqrt{2\rho_m c_p I_{sonic}} \tag{4.7.70}$$

Where, I_{sonic} is the sonic intensity that reaches the boundary, defined as:

$$I_{sonic} = \frac{P}{A_{sonic}} \tag{4.7.71}$$

In this system's geometry, horn application area A_{sonic} is:

$$A_{sonic} = \frac{1}{4} L\pi(D + 2\delta) \tag{4.7.72}$$

Where D is the steel basket's internal diameter and δ is the wall thickness.

P is the power that reaches the boundary. The boundary pressure is oscillating at the imposed frequency, so the force per unit area imposed at the boundary is:

$$F_A = -n \cdot p_{peak} e^{i\omega t} \tag{4.7.73}$$

Where n is the vector normal to the boundary surface. The final boundary condition is:

$$\sigma_s|_{horn\ boundary} \cdot n = F_A \tag{4.7.74}$$

The rest of the boundary is assumed to be immobile (Section 5-l), so the boundary condition is straightforward:

$$u_s|_{immobile\ boundary} = 0 \tag{4.7.75}$$

To close the theoretical section on the ultrasonic field modelling , coupling between the basket and poroelastic coffee matrix is needed. This model assumes that the porous matrix is coherent with the steel basket (Subchapter 4.2.2 - n), so:

$$u_m|_{boundary,internal} = u|_{boundary} \tag{4.7.76}$$

4.8. Acoustic Streaming

Acoustic streaming (AS) is the "generation of steady fluid motion resulting from the attenuation of the sound field within a fluid medium" [80], induced when ultrasound is applied. In a free liquid this mechanism is well understood: the acoustic wave carries momentum, and when the wave is attenuated by viscous absorption or scattered by solid boundaries, that momentum is deposited in the fluid as a body force that drives a mean flow superimposed on the zero-mean oscillation. Unlike cavitation, it requires no threshold pressure, produces no bubble nucleation, and generates no shock waves or microjets; instead it works continuously and gently, thinning the diffusion boundary layer at solid surfaces and replacing the concentration-depleted fluid adjacent to a dissolving particle with fresh solvent from the bulk. This makes acoustic streaming particularly relevant in extraction contexts where bubble formation is suppressed, such as inside a compacted packed bed, because the streaming body force is always present regardless of whether the cavitation threshold is reached [52][70]. AS in porous media results from viscous flow inhomogeneities, driven by the nonzero divergence of Reynolds stress due to kinetic energy fluctuations [23][51][80].

In the present work, a piezoelectric transducer coupled to the outer wall of the steel basket imposes harmonic elastic oscillations that propagate through the steel and excite coupled oscillatory motion of the solid coffee skeleton and the pore water, described by Biot's poroelastic theory. The acoustic field obtained is used to estimate the streaming-induced forcing responsible for the AS transport within the porous medium.

4.8.1. Reynolds Stress Tensor Definition

The Reynolds stress tensor is a mathematical representation used in fluid dynamics to account for the momentum transfer caused by fluctuations in a fluid. In oscillatory flows, such as those generated by ultrasound waves, the nonlinear interaction of the fluctuating velocity components gives rise to a non-zero time-averaged Reynolds stress tensor. The divergence of this tensor acts as a steady body force on the fluid, driving acoustic streaming.

The volumetric force generated by the nonlinear Reynolds stress tensor coming from an imposed acoustic field is defined as [23][51]:

$$\mathbb{f} = -\nabla \cdot (\langle \rho_f v_1 \otimes v_1 \rangle) \tag{4.8.1}$$

Where, v_1 is the real part of the oscillating acoustic velocity:

$$v_1 = \mathbb{R}\left(\tilde{v} e^{i\omega t}\right) \tag{4.8.2}$$

The part $v_1 \otimes v_1$ is the dyadic tensor of v_1, while $\langle \dots \rangle$ stands for the time average in a period span.

4.8.2. Volumetric Force 2D Complex Derivation

The following derivations will be for a 2D case (Subchapter 4.2.2 - k), but everything can be extended to the 3D case. Complex number properties reported in Appendix A are used to mathematically define the body force deriving from acoustic velocity attenuation, responsible for the generation of acoustic streaming.

The 2-D dyadic tensor in x, y coordinates is:

$$\begin{bmatrix} v_{1,x}v_{1,x} & v_{1,x}v_{1,y} \\ v_{1,y}v_{1,x} & v_{1,y}v_{1,y} \end{bmatrix} \tag{4.8.3}$$

The volumetric force can then be derived for x, y coordinates:

$$\mathbb{f}_x = -\left(\frac{\partial}{\partial x}\langle \rho_f v_{1,x}v_{1,x}\rangle + \frac{\partial}{\partial y}\langle \rho_f v_{1,x}v_{1,y}\rangle\right) \tag{4.8.4}$$

$$\mathbb{f}_y = -\left(\frac{\partial}{\partial x}\langle \rho_f v_{1,y}v_{1,x}\rangle + \frac{\partial}{\partial y}\langle \rho_f v_{1,y}v_{1,y}\rangle\right) \tag{4.8.5}$$

With the complex numbers properties found in Appendix A, 6, 7, 8 these equations can be generically written for i, j coordinates as:

$$v_{1,i} = \frac{1}{2}(\tilde{v}_i e^{i\omega t} + \tilde{v}_i^* e^{-i\omega t}) \tag{4.8.6}$$

$$v_i v_j = \frac{1}{2}\left(\tilde{v}_i e^{i\omega t} + \tilde{v}_i^* e^{-i\omega t}\right)\frac{1}{2}\left(\tilde{v}_j e^{i\omega t} + \tilde{v}_j^* e^{-i} \quad\right) \tag{4.8.7}$$

$$v_i v_j = \frac{1}{4}\left(\tilde{v}_i \tilde{v} e^{2i\omega t} + \tilde{v}_i \tilde{v}_j^* + \tilde{v}_i^* \tilde{v}_j + \tilde{v}_i^* \tilde{v}_j^* e^{-2i\omega t}\right) \tag{4.8.8}$$

The term $e^{-2i\omega t}$ has zero average on a period following the same logic explained in Subchapter 4.1.1 (just using a double angular frequency $\omega' = 2\omega$).

$$\langle v_i v_j \rangle = \frac{1}{4}\left(\tilde{v}_i \tilde{v}_j^* + \tilde{v}_i^* \tilde{v}_j\right) \tag{4.8.9}$$

This is the key step where appears that while the acoustic velocity has zero average during the span of a period, while its second-order effects, generated by the product of two first-order perturbation quantities, don't.

Finally, using property from Appendix A, 6:

$$\langle v_i v_j \rangle = \frac{1}{2}\mathbb{R}\left(\tilde{v}_i \tilde{v}_j^*\right) \tag{4.8.10}$$

$$\langle \rho_f v_i v_j \rangle = \frac{1}{2}\rho_f \mathbb{R}\left(\tilde{v}_i \tilde{v}_j^*\right) \tag{4.8.11}$$

The final definitions for the volumetric streaming force in x, y coordinates are:

$$\mathbb{f}_x = -\left[\frac{\partial}{\partial x}\left(\frac{1}{2}\rho_f \mathbb{R}(\tilde{v}_x \tilde{v}_x^*)\right) + \frac{\partial}{\partial y}\left(\frac{1}{2}\rho_f \mathbb{R}(\tilde{v}_x \tilde{v}_y^*)\right)\right] \tag{4.8.12}$$

$$\mathbb{f}_y = -\left[\frac{\partial}{\partial x}\left(\frac{1}{2}\rho_f \mathbb{R}(\tilde{v}_y \tilde{v}_x^*)\right) + \frac{\partial}{\partial y}\left(\frac{1}{2}\rho_f \mathbb{R}(\tilde{v}_y \tilde{v}_y^*)\right)\right] \tag{4.8.13}$$

4.8.3. Acoustic Streaming Flow

Once the volumetric acoustic streaming force is defined, the acoustic streaming steady state surface velocity components can be found by using $Eq.$ (4.5.10) derived from Brinkman's equation for fluid flow in porous media. The velocities retrieved for the x and y coordinates are used to determine the magnitude of the AS velocity:

$$v_{AS} = \sqrt{v_{AS,x}^2 + v_{AS,y}^2} \tag{4.8.14}$$

4.8.4. Boundary Condition

The boundary condition for the acoustic streaming porous flow is a simple no-slip at boundary:

$$v_{AS}|_{boundary} = 0 \tag{4.8.15}$$

Since the velocity depends only on the gradient of pressure and not on pressure itself, an infinite set of solutions for p can generate the same velocity field. To make the system uniquely solvable an additional condition on the pressure must be set. A pressure point constraint can be used to set a reference point:

$$p(x_p, y_p) = 0 \tag{4.8.16}$$

The chosen value does not affect the velocity field and is set on an arbitrary (x_p, y_p) point of the fluid's domain.

4.9. Model Closure

Right now, the extraction model and ultrasonic + acoustic streaming porous flow models are complete but separated. To quantify the effects of acoustic streaming in mass transfer enhancement the full superficial velocity is needed. The axial velocity is normal to the streaming velocity field, so the magnitude of the total superficial velocity can be calculated as [77]:

$$v_{tot} = \sqrt{v_{ax}^2 + v_{AS}^2} \tag{4.9.1}$$

To feed back this velocity inside of the 1D extraction model the surface average of v_{tot} is used:

$$v_{tot,avg.} = \frac{\int v_{tot}\, dS}{S} \tag{4.9.2}$$

The newly found $v_{tot,avg.}$ Is then fed back into $eq.(4.6.11)$ to determine the new enhanced external mass transfer coefficient to use in the extraction model. The final index will be the concentration percentage enhancement with respect to un-sonicated coffee:

$$X = 100\frac{C_{cup}|_{sonicated} - C_{cup}|_{un-sonicated}}{C_{cup}|_{un-sonicated}} \tag{4.9.3}$$

5 Model Parameters and Material Properties

5.1. Operative Parameters

Operative parameters of the espresso machine are key factors in determining the outcome of the extraction. The parameters used following general recommendations [3][82] are listed in the next table.

Table 5.1: Operative parameters

Variable	Description	Value	SI unit
T_{op}	Temperature	90	°C
p_{in}	Inlet pressure	8	atm
p_{out}	Outlet pressure	1	atm
t_{tot}	Extraction time	25	s

5.2. Coffee Bed Properties

5.2.1. Drained Matrix Properties

While there is no literature on elastic properties of compacted dry coffee grind matrices, these can be evaluated through the Hashin-Shtrikman bounds, which define upper and lower bounds for elastic properties of a mixture of isotropic elastic materials. The strictest situation happens at the upper bound, because the porous matrix would have more resistance to deformation. The upper bounds for bulk and shear moduli of the dry porous matrix are defined as [59]:

$$K_d = K_s + \frac{\phi}{-\frac{1}{K_s} + \frac{3(1-\phi)}{3K_s + 4G_s}} \tag{5.2.1}$$

$$G_d = G_s + \frac{\phi}{-\frac{1}{G_s} + \frac{6(1-\phi)(K_s + 2G_s)}{5G_s(3K_s + 4G_s)}} \tag{5.2.2}$$

Where K_s and G_s are the bulk and shear moduli of the solid non intra-particle porous material. Their relationships with Young's modulus and Poisson's ratio are:

$$K = \frac{E}{3(1-2v)} \tag{5.2.3}$$

$$G = \frac{E}{2(1+v)} \tag{5.2.4}$$

5.2.2. Derivation of Bed Properties From PSD

Some of the granular bed's properties must be derived from a sample PSD (Particle Size Distribution). The first step is to organize the data in volume brackets: a PSD gives the percentage of the volume under a certain size, while it is more useful to define diameters associated to volume brackets instead.

$$\Delta V(\%)_i = V(\%)_i - V(\%)_{i-1} \tag{5.2.5}$$

This introduces the problem of assigning the correct diameter to the volume bracket, so the geometric average between consecutive diameters is used:

$$d_{g,i} = \sqrt{d_i d_{i-1}} \tag{5.2.6}$$

Now all the necessary parameters can be estimated. One of the most important ones is Sauter's diameter $d_{3,2}$, defined as "the diameter of spherical objects that reflects the size of identical spherical objects of which the total surface energy is equal to the total surface energy of polysized spherical objects, while both systems have the same total area and total volume" [66]:

$$d_{3,2} = \frac{\sum_i n_i d_i^3}{\sum_i n_i d_i^2} \tag{5.2.7}$$

In the context of a discrete distribution like a PSD, Sauter's diameter is obtained by considering the proportionality between the particle number of a partition and the volume partition:

$$\Delta V(\%)_i \propto n_i d_{g,i}^3 \tag{5.2.8}$$

$$n_i \propto \frac{\Delta V(\%)_i}{d_{g,i}^3} \tag{5.2.9}$$

$$d_{3,2} = \frac{\sum_i d_{g,i}^3 \frac{\Delta V(\%)_i}{d_{g,i}^3}}{\sum_i d_{i,g}^2 \frac{\Delta V(\%)_i}{d_{g,i}^3}} \tag{5.2.10}$$

$$d_{3,2} = \frac{\sum_i \Delta V(\%)_i}{\sum_i \frac{\Delta V(\%)_i}{d_{g,i}}} \tag{5.2.11}$$

Mean diameter is useful when dealing with the difference between fine and coarse grains. It can be easily calculated as a weighted average:

$$d_{av} = \frac{\sum_i \Delta V(\%)_i d_{g,i}}{\sum_i \Delta V(\%)_i} \tag{5.2.12}$$

The last useful parameter β derives from the Rosin-Rammler distribution, defined as:

$$V(\%) = 1 - e^{-\left(\frac{d}{\alpha}\right)^{\beta}} \tag{5.2.13}$$

The linearization of $eq.(4.11.13)$ provides an easy way to obtain β via linear regression from PSD data:

$$ln[-\ln(1 - V(\%))] = \beta \ln(d) - \beta \ln(\alpha) \tag{5.2.14}$$

5.2.3. Derivation of Roasted Coffee Poisson's Module

While information on roasted coffee Young's elastic modulus is available, Poisson's ratio has not been evaluated. The only data available regards green coffee beans, with $\upsilon_g = 0.3$. An estimation can be made considering that during roasting coffee intra-particle porosity raises from 4% to about 40% [28]. Assuming the initial green bean porosity as negligible, a correlation for porous materials constructed by randomly positioned overlapping solid spheres [62]:

$$\upsilon_R = 0.14 + \left(1 - \frac{\phi_{intra}}{0.5}\right)^{1.22} (\upsilon_g - 0.14) \tag{5.2.15}$$

5.2.4. Coffee Properties from References

Many arabica coffee properties can be easily retrieved from literature. The following Table 5.2 reports the ones used in the present work.

Table 5.2: Coffee properties from references

Variable	Description	Value	SI unit	Reference
$\rho_{intrinsic}$	Intrinsic density	1337	kg/m^3	[30]
ϕ_{intra}	Intra-particle porosity	0.4	–	[28]
ϕ_{bed}	Granular bed porosity	0.18	–	[30]
Γ_0	Initial caffeine concentration	0.013	–	[69]
$\mathcal{D}$	Water-caffeine diffusivity 90 °C	$2.6 \cdot 10^{-9}$	m^2/s	[70]
h	Caffeine hindrance factor	10	–	[68]
Ψ	Coffee grain sphericity	0.79	–	[33]
E	Roasted coffee Young's modulus	4	MPa	[60]
υ_g	Green coffee Poisson's ratio	0.3	–	[61]
m	Volumetric partition coefficient	0.98	–	[69]

5.2.5. Coffee Properties from PSD

The particle size distribution (PSD) obtained from a domestic automatic espresso machine (De'Longhi Magnifica) exhibits a broad bimodal character, typical of consumer-grade grinders. The distribution is composed of a fines-dominated mode (~25 μm) and a coarse mode centered around ~800 μm, resulting in a relatively high heterogeneity compared to professional espresso grinding systems. Despite the presence of a significant coarse tail, the overall Sauter mean diameter (~123 μm) remains within the espresso range.

The Sauter's mean diameter is highly sensitive to the presence of ultrafine particles due to its surface-area weighting. As a result, even a small volumetric fraction of fines can significantly bias $d_{3,2}$ towards lower values. To avoid disproportionate influence of negligible tail contributions, a threshold-based filtering was applied,

excluding size classes contributing less than 1% to the cumulative volume, resulting in a more representative descriptor of the bulk particle population. The next table presents all relevant properties extrapolated from the PSD:

Table 5.3: Coffee properties from PSD

Variable	Description	Value	SI unit
$d_{3,2}$	PSD Sauter diameter	122.968	μm
β_{coarse}	Coarse fraction beta parameter	2.3297	–
d_{coarse}	Coarse fraction mean diameter	801.206	μm
d_{fines}	Fines fraction mean diameter	26.3616	μm
θ_{coarse}	Coarse fraction volumetric rate	0.7048	–
θ_{fines}	Fines fraction volumetric rate	0.2952	–

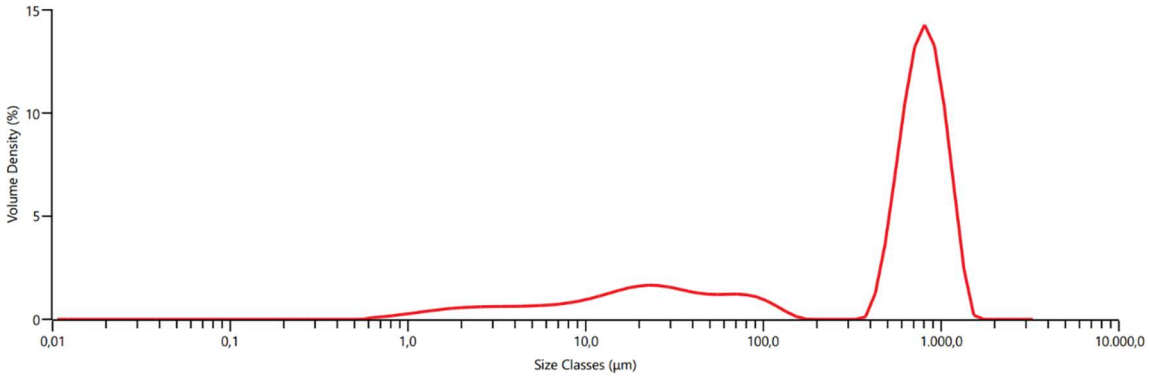

Figure 5.1: Considered particle size distribution (PSD) from Brasile arabica coffee grinded with De'Longhi Magnifica espresso machine grinder.

5.3. AISI 304 Steel Properties

AISI 304 stainless steel is the material of the espresso portafilter basket adopted in this work, as described in Subchapter 4.2.1. Its elastic properties influence the transmission of acoustic energy from the horn into the coffee bed through the basket wall and are therefore required as input to the solid mechanics sub-problem described in Subchapter 4.7.3.

Table 5.4: AISI 304 Steel properties retrieved from ANSYS Granta EduPack (v2021 R1)

Variable	Description	Value	SI unit	Reference
ρ_m	Steel Density	7850	kg/m^3	[72]
E_m	Steel Young's modulus	190	MPa	[72]
ν_m	Steel Poisson's ratio	0.27	–	[72]

5.4. Water Properties

Water properties do not change significantly in the chosen pressure range. The following adopted ones are at 90°C and 4 atm. The properties are derived from IAPWS IF97 standard formulation [71].

Table 5.5: Water properties

Variable	Description	Value	SI unit	Reference
ρ_f	Water density	965.4	kg/m^3	[71]
μ_f	Water dynamic viscosity	$3.14 \cdot 10^{-4}$	$Pa \cdot s$	[71]
c_f	Speed of sound in water	1553	m/s	[71]

5.5. Geometric Properties

The system present in this work uses a single-shot espresso portafilter basket, with dimensions reported in Table 5.6. Basket's thickness is object of the parametric study described in Chapter 6.

Table 5.6: Geometric properties

Variable	Description	Value	SI unit
D	Steel basket's internal diameter	0.046	m
L	Steel basket's height	0.01	m

6 Parametric Study and Numerical Approach

Since the geometry of the coffee matrix is defined by the basket's height and internal diameter, the focus of this work is a parametric study focused on basket thickness and applied power. The basket wall thickness was treated as a design parameter and varies between 0.4 mm and 0.7 mm. The upper limit is consistent with the dimensions reported for commercial precision espresso baskets, from which a wall thickness of approximately 0.68 mm can be geometrically inferred. The lower limit was selected to account for thinner sections that may result from deep-drawing manufacturing processes and to investigate the sensitivity of the system response to wall thickness variations. Ultrasonic power at horn-basket boundary varies between 50 to 200 W to represent the small-scale range of sonicators power available on the market. The nominal power of the sonicators is higher than the studied one due to electrical and coupling losses in the system.

The solution of the extraction model is obtained through a MATLAB® script written by the authors and run in version R2025b on the authors local PC. The ultrasonic extraction model was solved with COMSOL Multiphysics® Version 6.1 on the Politecnico di Milano cluster PC.

6.1. Extraction Model Numerical Solution

6.1.1. Equations Discretization

The convection-diffusion equations present in the extraction model (Subchapter 4.6) must be discretized to be solved in MATLAB®**.** The choice of Euler's backwards implicit scheme was made for stability reasons. Equations 4.6.8 and 4.6.9 can be written as:

$$\frac{q_i|_j^{n+1} - q_i|_j^n}{\Delta t} = a_i k_{c,i} \left(\frac{C|_j^{n+1}}{m} - q_i|_j^{n+1} \right) \quad \forall i \tag{6.1.1}$$

$$\phi \frac{C|_j^{n+1} - C|_j^n}{\Delta t} = u \frac{C|_j^{n+1} - C|_{j-1}^{n+1}}{\Delta z} + \sum_i (1-\phi)\left[\theta_i a_i k_{c,i}\left(\frac{C|_j^{n+1}}{m} - q_i|_j^{n+1}\right)\right] \quad (6.1.2)$$

Where n is the time step and j is the spatial step.

The equation for solids $eq.(6.1.1)$ can be rearranged to highlight a linear dependence on $C|_j^{n+1}$:

$$q_i|_j^{n+1} = \frac{q_i|_j^n + a_i k_{c,i} \Delta t \left(\frac{C|_j^{n+1}}{m}\right)}{1 + a_i k_{c,i} \Delta t} \quad \forall i \quad (6.1.3)$$

6.1.2. Error Evaluation

To keep track of the error introduced by the discretization, a total mass balance is introduced, alongside a percentage error indicator. The total mass of solute initially present in the system is:

$$m_{tot} = \rho_{bean}(1-\phi)\Gamma_0 V \quad (6.1.4)$$

The solute mass present in the entrapped liquid phase is:

$$m_{liquid} = \phi S \int_0^{z=L} C(t,z)\, dz \quad (6.1.5)$$

The remaining solute mass in the solid fraction is:

$$m_{solid,i} = (1-\phi) S \theta_i \int_0^{z=L} q_i(t,z)\, dz \quad (6.1.6)$$

$$m_{solid} = \sum_i m_{solid,i} \quad (6.1.7)$$

Finally, the mass leaving the system and entering the cup is:

$$m_{out} = v_{ax} S \int_0^t C(t, z=L)\, dt \quad (6.1.8)$$

The model keeps track of the total mass balance at every time step:

$$m_{tot} - \left(m_{liquid} + m_{solid} + m_{out}\right) = 0 \quad (6.1.9)$$

Finally, a percentage error can be introduced to keep track of the approximation introduced by the discretization and make sure it stays low:

$$err = \frac{m_{tot} - \left(m_{liquid} + m_{solid} + m_{out}\right)}{m_{tot}} \times 100 \quad (6.1.10)$$

6.1.3. Meshing

The spatial mesh of the extraction model has element size of $8.4034 \cdot 10^{-5}\, m$ allowing for 120 subdivisions of the 1 cm chamber height. The adopted time step is $0.0417\, s$.

With the implicit scheme described, the classical Courant and Diffusion numbers and their 1-D limit conditions ($Co < 1, Di < 0.5$) are not needed as the system is intrinsically stable as long as a solution is found for every time step. The reported spatial and temporal mesh sizes were chosen to keep the computational time low while making sure that the error stayed lower than 1 %.

6.1.4. Matlab® Code

Here is reported the simplified structure of the code developed by the authors to solve the convection-diffusion extraction problem.

Algorithm Coffee Extraction Model

```
Initialize physical parameters, geometry, and transport properties
Compute Darcy velocity, flow rate, and mass transfer coefficients
Discretize spatial domain x ∈ [0, H] into N_x nodes
Discretize time domain t ∈ [0, t_end] into N_t steps
Initialize concentration fields C (liquid), q (coarse), q1 (fines)
for each time step n = 1 to N_t − 1 do
    Impose boundary conditions at inlet: C(0) = 0, q(0) = 0, q1(0) = 0
    Store previous time-step solution: C^n, q^n, q1^n
    for each spatial node j = 2 to N_x do
        Compute transient mass transfer coefficients
        Compute overall mass transfer coefficients
        Solve nonlinear balance equation: find C_j^(n+1) using fzero function
        Update solid phase concentrations: q_j^(n+1), q1_j^(n+1)
    end for
    Compute outlet concentration and cumulative extracted mass
    Update mass balances
    Compute global conservation error
end for
Post-process results
```

6.1.5. PC Specs and Computing Time

MATLAB® simulations were carried out on an Acer Nitro 5 Pc with a Ryzen 7 5800H processor (8 cores, 16 threads), 8 GB of DDR4 ram, with each simulation taking under 3 s to complete.

6.2. Ultrasound Model Numerical Approach

6.2.1. Symmetry

The considered system is symmetric with respect to the diameter that splits the circle into a semicircle passing through the midpoint of the horn application boundary as shown in Figure 6.1. The materials are homogeneous and isotropic; hence a symmetry condition can be exploited to greatly reduce computational cost. The symmetry condition implies that no material crosses the symmetry plane. This can be done by imposing the following symmetry conditions at the symmetry axis boundary:

Poroelastic model

$$\begin{cases} u \cdot n|_{simmetry\ boundary} = 0 & (6.2.1) \\ w \cdot n|_{simmetry\ boundary} = 0 & (6.2.2) \end{cases}$$

Solid mechanics

$$u_s \cdot n|_{simmetry\ boundary} = 0 \quad (6.2.3)$$

Brinkman porous flow

$$v \cdot n|_{simmetry\ boundary} = 0 \quad (6.2.4)$$

Exploiting the symmetry condition, only one half of the domain is solved numerically. The full-field solution is subsequently reconstructed by symmetry, reflecting the results across the symmetry axis. This reduces the computational effort while preserving the accuracy of the physical model.

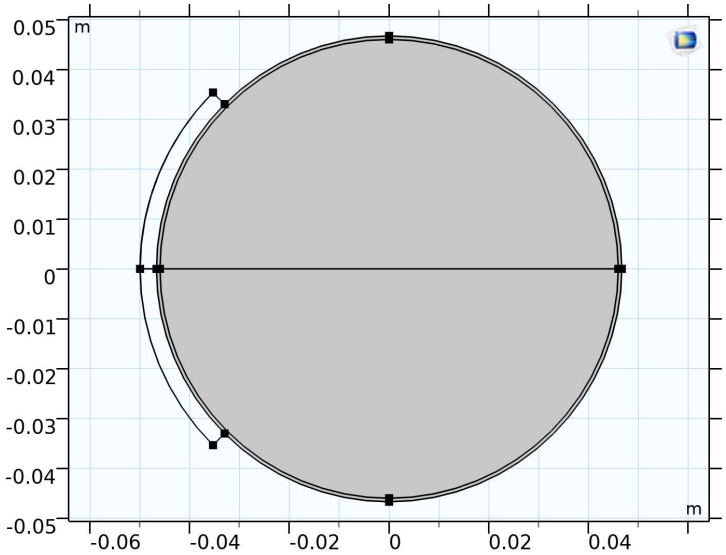

Figure 6.1: Entire 2-D geometry with symmetry axis. The added part on the left representing the horn application is just for visualization purpose

6.2.2. Meshing Limits

Strict mesh limits are necessary to correctly solve ultrasound transmission in both the metal and the coffee/water matrix. The main idea behind mesh limits is that the wave traveling inside the media should be sampled enough times per wavelength. In first-order discretization schemes, such as linear finite elements or first-order finite differences, the continuous displacement field is approximated using piecewise linear interpolation. The field is assumed to vary linearly within each element, while only nodal values are explicitly solved. This representation allows the continuous wavefield to be reconstructed approximately from discrete samples.

The recommended limit for poroelastic media is to have the mesh to sample the wavelength of the slowest wave at least 5 to 6 times [57]. As discussed in Subchapter 4.7.1.3, the slow P2 wave is the one to be used:

$$\lambda_{P2} = \frac{c_{P2}}{f} \tag{6.2.5}$$

$$h_m < \frac{\lambda_{P2}}{5-6} \tag{6.2.6}$$

The same is valid for linear elastic materials [57], where the slow wave is the shear S-wave:

$$\lambda_S = \frac{c_S}{f} \tag{6.2.7}$$

$$h_m < \frac{\lambda_S}{5-6} \tag{6.2.8}$$

An additional condition is that for thin structures at least two elements in thickness are needed this is necessary because respecting only condition (6.2.8) could lead to the formation of a mesh that has only one discretization element in thickness.

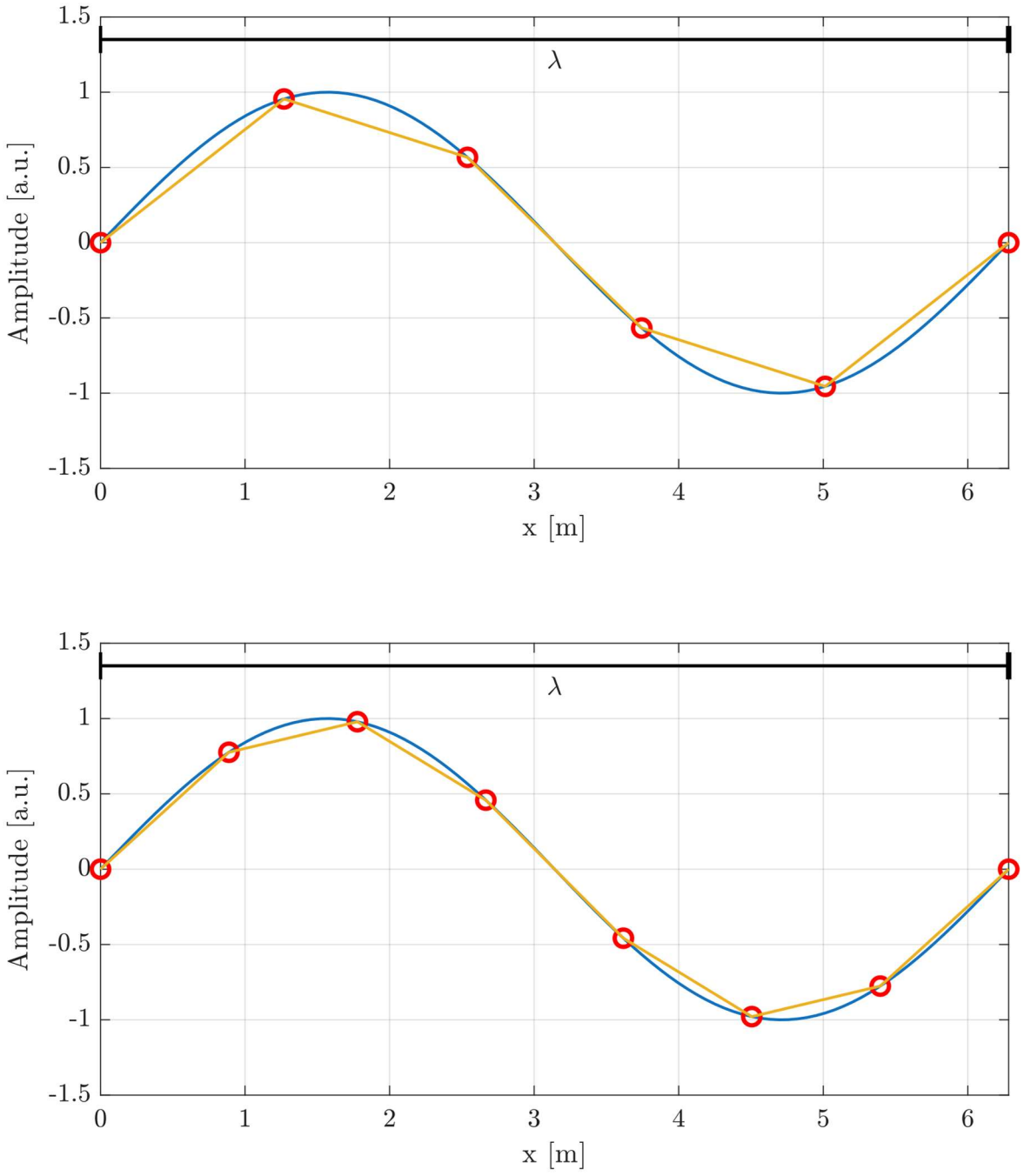

Figure 6.2: Schematic representation of a continuous wavefield and its first-order spatial discretization. The field is approximated using linear interpolation between discrete nodes values, resulting in a piecewise linear representation of the wave. First image has 6 samples per wavelength; second image has 8 samples per wavelength.

6.2.3. Meshing

The computational domain consists of a two-dimensional semi-circular geometry obtained by exploiting symmetry, which allows the simulation of half of the physical system and reduces computational cost while preserving accuracy. The mesh is composed of two distinct regions: (i) the internal porous medium region (coffee–water) and (ii) the surrounding metallic layer, whose thickness is treated as a geometric parameter.

The internal porous domain is discretized using a high-resolution unstructured triangular mesh, which is kept constant across all simulations. The mesh consists of 7,207,400 nodes and 14,405,630 triangular elements. Mesh quality is assessed using the skewness (element quality) metric, which measures the deviation of each element from its ideal shape. The quality metric is normalized between 0 and 1, where a value of 1 corresponds to an ideal element and 0 represents a degenerated element. Element quality is considered poor if the value sits below the 0.1 mark. The skewness-based quality indicator shows a minimum element quality of 0.5169 and an average value of 0.9711, indicating a high-quality mesh.

The external metallic layer is discretized using an unstructured triangular mesh generated with a free meshing approach. Unlike the porous region, this mesh is regenerated for each value of the metal thickness parameter, while maintaining the same meshing strategy and refinement criteria.

Table 6.1: Metal basket mesh statistics

Basket thickness	Mesh vertices	Triangles	Minimum element quality	Average element quality
0.4 mm	26673	46250	0.4675	0.7989
0.5 mm	26371	45879	0.4151	0.7941
0.6 mm	26375	46055	0.418	0.7937
0.7 mm	26124	45679	0.3948	0.791

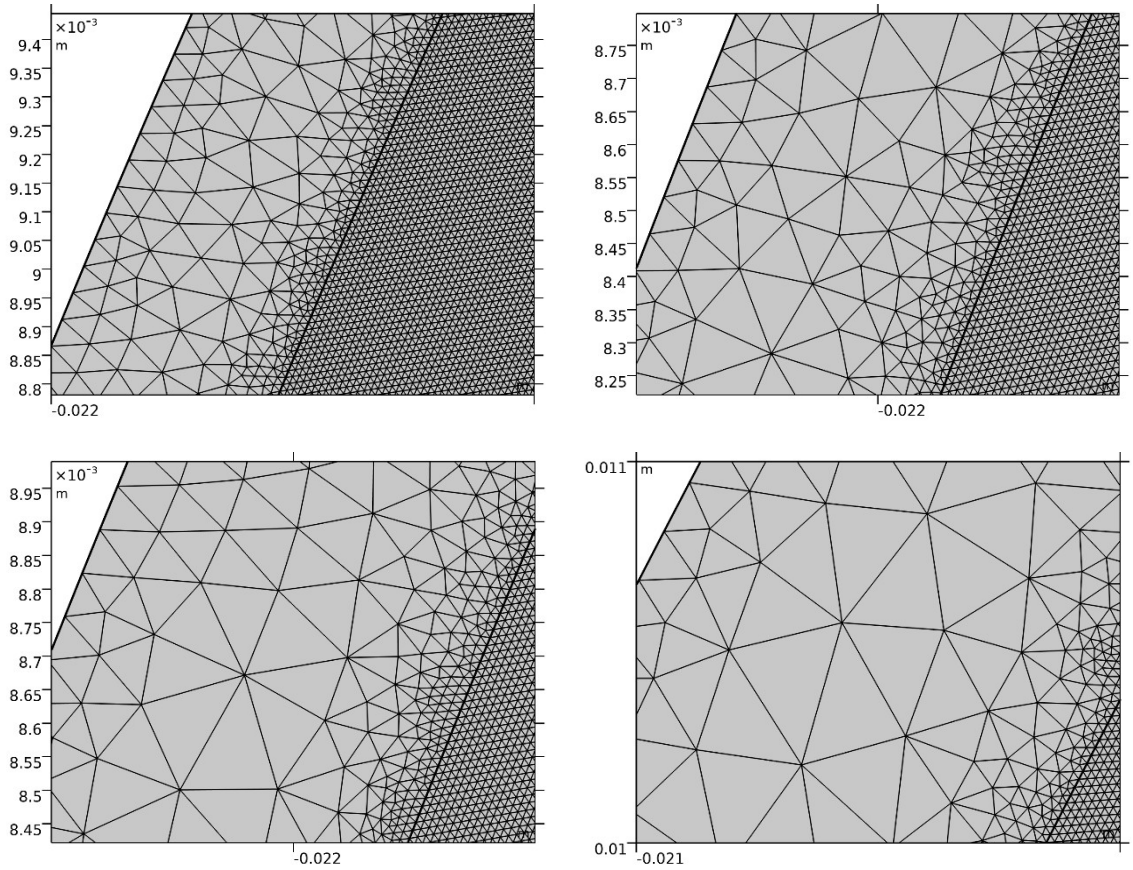

Figure 6.3: left-to-right, top-to-bottom zoomed meshes for 0.4 mm, 0.5 mm, 0.6 mm and 0.7 mm thicknesses respectively. Metal basket always has more than 10 elements on the thickness.

6.2.4. Solvers Configuration

The problem was solved using two different numerical setups in COMSOL Multiphysics®, corresponding to the acoustic (frequency-domain) and fluid flow (stationary) formulations.

For the frequency-domain acoustic problem, governed by Biot's poroelasticity theory, an iterative Krylov subspace solver was employed. Specifically, the linear system was solved using the Generalized Minimal Residual (GMRES) method. GMRES is a robust iterative algorithm designed for large, sparse, and non-symmetric linear systems. GMRES belongs to the class of Krylov subspace methods, which build an approximate solution in a low-dimensional space generated by successive matrix–vector products, avoiding explicit matrix factorization and making the method suitable for large sparse systems. It constructs an orthogonal basis of the Krylov subspace and minimizes the residual over this subspace at each iteration, making it particularly suitable for wave propagation problems where

direct solvers become computationally expensive. To enhance convergence, a geometric multigrid (GMG) preconditioner was used. Multigrid methods accelerate convergence by addressing errors at multiple spatial scales. In the geometric multigrid approach, the hierarchy of grids is explicitly defined based on the geometric structure of the problem. The finest mesh, corresponding to the one presented in Subchapter 6.2.3, is used to estimate a first solution, coarser meshes are progressively adopted to reduce the error in the finer mesh until it reaches a certain set threshold.

For the stationary fluid flow problem, described by the Brinkman equations in porous media, a segregated iterative solver was adopted. The system was decomposed into two coupled blocks: the velocity field and the pressure field, which were solved sequentially rather than simultaneously. This segregation improves computational efficiency and reduces memory requirements for large-scale systems. Each subproblem was solved using GMRES, combined with an algebraic multigrid (AMG) preconditioner. Unlike geometric multigrid, AMG does not require an explicit grid hierarchy; instead, it constructs coarse representations of the system directly from the matrix structure. The AMG preconditioner constructs a hierarchy of progressively coarser problems directly from the system matrix, based on the strength of the algebraic coupling between degrees of freedom. Unlike geometric multigrid methods, AMG does not rely on the underlying mesh topology or spatial coordinates. The velocity and pressure coupling was handled iteratively, with AMG preconditioning improving the conditioning of each subproblem and ensuring convergence of the overall segregated scheme.

6.2.5. PC Specs and Computing Time

COMSOL Multiphysics® numerical simulations were performed on a high-performance computing (HPC) cluster running CentOS 7. The computational node is equipped with two Intel Xeon E5-2680, each featuring 8 physical cores, for a total of 16 CPU cores (32 logical threads) per node. The system operates in a dual-socket NUMA configuration with 128 GB of shared RAM.

Due to the computational complexity of the finite element models, individual simulations required approximately 35 minutes if the GMG meshes were already present, 50 minutes if not. The simulations showed a peak memory usage of approximately 126 GB, i.e. nearly the full 128 GB RAM capacity limit of the computing node.

7 Results and Discussion

Before presenting and discussing the results, it is useful to report the values of the main parameters calculated and used throughout the analysis. The extraction results are first presented for the reference case, corresponding to espresso extraction without the application of ultrasound. Subsequently, a parametric study is discussed, focusing on the influence of two variables: the thickness of the metal basket and the ultrasonic power applied by the horn. The basket thickness varied between 0.4 and 0.7 mm, while the applied ultrasonic power at the boundary ranged from 50 to 200 W, with a frequency range of 20 – 40 kHz. Acoustic velocity and AS velocity fields are reported and extraction enhancement is calculated.

7.1. Intermediate Results

The following Table 7.1 reports useful intermediate calculated values of parameters used during the simulation.

Table 7.1: Derived intermediate values

Variable	Description	Value	SI unit
c_P	Metal P wave speed	5599.9	m/s
c_S	Metal S wave speed	4445.2	m/s
k	Permeability	$3.13 \cdot 10^{-15}$	m^2
p_{peak}	Peak pressure at boundary	6.92	MPa
r_h	Pore hydraulic radius	$2.86 \cdot 10^{-7}$	m
v_{ax}	Axial velocity	$7.06 \cdot 10^{-4}$	m/s
ρ_{bean}	Coffee bean density	802.2	kg/m^3
τ	Bed tortuosity	2.357	–

The main pore-flow determining parameter, permeability, results consistent with wet-matrix literature data, with Foster, J. et al. [45] reporting a value of $2.97 \cdot 10^{-1}\ m^2$. The swollen matrix pore diameter is calculated from the hydraulic radius: $d_{pore} = 4r_h$, with a result of $1.144\ \mu m$. This value may seem low in comparison to dry-matrix observations, reporting pore sizes in the order of tens of microns [83], but that can be explained by the fact that a 30-fold decrease in effective diameter happens due to swelling, as reported by Waszkiewicz, R. et al. [82]. It is important to note that Biot's wave speeds are affected by the frequency because of the presence of complex density shown in $eq.$ (4.7.6). P1 and P2 wave speeds will be reported later in Subchapter 7.2.

7.2. Espresso Extraction

Espresso extraction was first simulated without the contribution of the ultrasonic probe to verify the model and set a baseline case to confront later results, when ultrasounds are applied. Although the numerical model can handle multi-component extraction, the focus of this work is caffeine, as it is the main component used across literature to quantify the extraction quality. The single-shot espresso is prepared using 10.93 g of ground coffee, calculated from volumetric considerations.

$$V_{basket} = L\pi\frac{D^2}{4} \tag{7.2.1}$$

$$m_{coffee} = V_{basket}\rho_{bean}(1-\phi) \tag{7.2.2}$$

The coffee brew mass in cup is determined using the volumetric flowrate $Q\ [m^3/s]$ of the system, obtaining a value of 29.32 ml.

$$S = \pi\frac{D^2}{4} \tag{7.2.3}$$

$$Q = v_{ax}S \tag{7.2.4}$$

$$m_{cup} = \rho_f Q t \tag{7.2.5}$$

Brew ratio is defined as the mass of coffee grounds per mass of water used. It is a key indicator used in various coffee quality control charts [85], with values between 1:2 and 1:3 being considered standard for espresso coffee. It can be calculated as the ratio of the sum of the water mass in cup and the remaining water entrapped in the puck and the coffee mass, resulting in a ratio of 1:2.85.

$$BR = \frac{m_{cup} + \phi\rho_f V_{basket}}{m_{coffee}} \tag{7.2.6}$$

Caffeine cup concentration is calculated from $eq.$ (4.6.23), with a value of 2.1 mg/ml.

All these values fall within the ranges commonly reported for espresso coffee beverages [3], [81], suggesting that the model provides physically realistic predictions.

As expected, following Subchapter 1.4, fine particles show enhanced mass transfer of caffeine relative to coarse particles due to their larger specific surface area, related to their smaller diameter, as shown in $eq.(4.6.2)$. Coarse particles exhibit a near-linear extraction trend, while fine particles are quickly exhausted, resulting in a significant reduction in driving force despite a higher initial gradient. The resulting extraction profile of caffeine concentration in the outlet water exhibits an early peak, driven by rapid release from fine particles, followed by a descending tail governed by the slower extraction from coarse particles as fine particles start to be exhausted.

The cumulative caffeine mass in the cup follows a similar profile, showing rapid initial increase followed by a slower rate. The mass of caffeine in the cup at the end of extraction is 61.56 mg, with USDA (U.S. Department of Agriculture) reporting a value of 63 mg per single-shot espresso cup [86]. Percentage error for the baseline case sits under the 0.3 % mark, confirming that the mesh values reported in Subchapter 6.1.3 are suitable for maintaining the accuracy of the solution. Error varies with transport coefficients. The maximum error found for a total velocity contributing to external mass transfer of $0.01\ m/s$ is 0.956 %, still under the 1 % mark. This limit is not reached anyways as shown later in Subchapter 7.2.2.

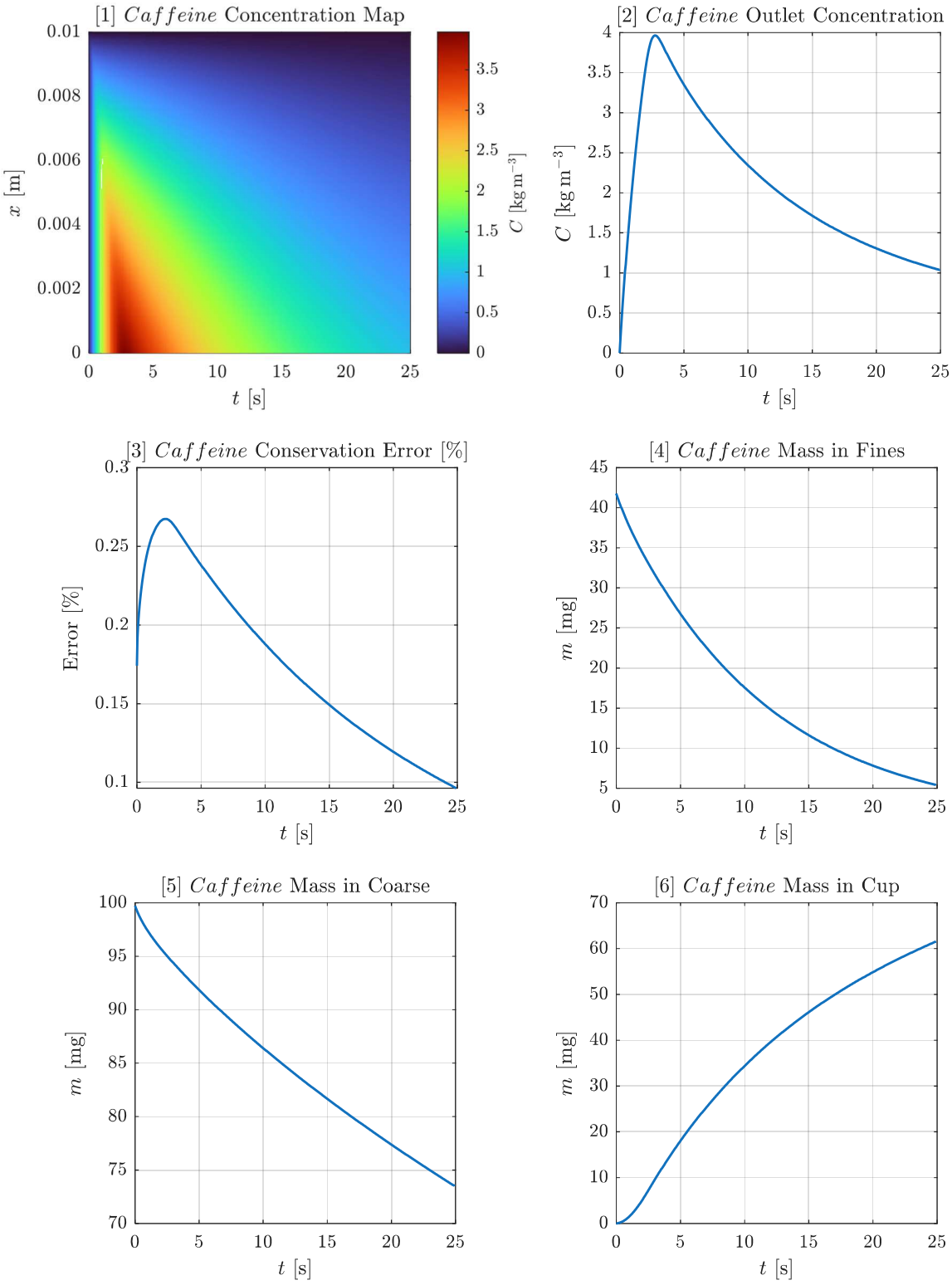

Figure 7.1: [1] Caffeine concentration at every time step along the z-axis. [2] Caffeine outlet concentration profile. [3] Percentage mass conservation error evolution in time [4] Remaining caffeine mass in fines fraction during extraction. [5] Remaining caffeine mass in coarse fraction during extraction. [6] Caffeine mass extracted inside of the cup.

7.3. Parametric Ultrasonic Fields Study

The parametric analysis was performed to investigate the influence of the metal basket thickness on the acoustic response of the porous medium and on the resulting acoustic streaming. Four basket thicknesses were considered, namely 0.4 mm, 0.5 mm, 0.6 mm and 0.7 mm. For each thickness, a frequency sweep between 20 kHz and 40 kHz was conducted and the frequency maximizing the area-averaged total velocity was identified. It is important to note that this study keeps the same geometry for all the simulations, meaning that the ultrasonic horn is always occupying 1/4th of the lateral area. One could argue that results may differ due to a difference in application area, as it turns out from $eq.(4.7.72)$, but the maximum difference (e.g. between the 0.4 mm case and the 0.7 mm case) is only 0.65 %, i.e. completely negligible.

The optimal frequencies were found to be 39996 Hz, 39513 Hz, 39514 Hz and 39006 Hz for basket thicknesses of 0.4 mm, 0.5 mm, 0.6 mm and 0.7 mm, respectively. Graphical representations of the peaks are available in Appendix B. Although a general decrease in the optimal frequency can be observed as the basket thickness increases, the frequency shift remains relatively small when compared to the substantial differences observed in the acoustic field distributions and in the resulting streaming response. In particular, the optimal frequencies corresponding to the 0.5 mm and 0.6 mm configurations differ by only 1 Hz, yet the associated acoustic velocity fields exhibit different spatial patterns. The primary effect of basket thickness is not just a shift in frequency response, but rather a modification of the spatial structure of the acoustic velocity field within the porous medium.

7.3.1. Model validity based on wavelengths

Once peak frequencies and sound velocities i.e. wavelengths are known, assumption (a) from Subchapter 4.2.2 regarding Biot's theory treatment of porous media as homogeneous and meshing conditions expressed by $eqs.(6.2.6), (6.2.8)$ can be verified.

Homogeneous media assumption reported in Subchapter 4.2.2 – (a), meaning that $\lambda_{P2} \gg d_{pore}$, is true for all considered configurations as shown in the following Table 7.2.

Table 7.2: Biot homogeneous media assumption verification

$\delta\ [mm]$	$f_{peak}\ [Hz]$	$c_{P2}\ [m/s]$	$\lambda_{P2}\ [\mu m]$	$\lambda_{P2}/d_{pore}\ [-]$
0.4	39996	3.9337	98.35	85.90
0.5	39513	3.9090	98.93	86.40
0.6	39514	3.9090	98.93	86.40
0.7	39006	3.8821	99.53	86.92

S-wave wavelengths for the metal basket domain are orders of magnitude higher than P2-wave wavelengths (10^{-1} m vs. 10^{-5} m), showing that, following $eq.$ (6.2.6) and $eq.$ (6.2.8), the meshing bottleneck is clearly the poroelastic domain.

Table 7.3: S-wave wavelengths in basket domain at peak frequencies.

$\delta\ [mm]$	$\lambda_S\ [m]$
0.4	0.111
0.5	0.112
0.6	0.112
0.7	0.114

For the poroelastic media, all the meshes respect the condition set by $eq.$ (6.2.6) as shown in Table 7.4.

Table 7.4: P2 wavelength to maximum mesh size and P2 wavelength to average mesh size ratios in poroelastic domain for all considered configurations at peak frequencies.

$\delta\ [mm]$	$\lambda_{P2}/\max(h_m)$	$\lambda_{P2}/avg\ (h_m)$
0.4	5.94	8.33
0.5	5.90	8.38
0.6	5.91	8.38
0.7	5.94	8.43

The metal basket wavelength-to-mesh size ratios are, as expected, way higher than the low limit imposed by $eq.$ (6.2.8).

Table 7.5: S wavelength to maximum mesh size and S wavelength to average mesh size ratios in metal basket domain for all considered configurations at peak frequencies.

$\delta\ [mm]$	$\lambda_S/\max\ (h_m)$	$\lambda_S/\text{avg}\ (h_m)$
0.4	731.34	1540.12
0.5	573.93	1243.23
0.6	511.05	1050.30
0.7	428.76	875.76

7.3.2. Thickness Influence on Velocities

The area-averaged acoustic velocity, acoustic streaming velocity and total velocity obtained at the respective optimal frequencies are summarized in Table 7.6.

Table 7.6: Area-averaged acoustic velocity, acoustic streaming velocity and total velocity obtained at 200 W and peak frequencies.

$\delta\ [mm]$	$v_{Ac.,avg.}\ [m/s]$	$v_{AS,avg.}\ [m/s]$	$v_{tot,avg.}\ [m/s]$
0.4	3.5951	0.0066853	0.0067808
0.5	3.7567	0.0023232	0.0026030
0.6	1.6395	0.0028790	0.0031847
0.7	1.5721	0.0007760	0.0011495

The first quantity is the area-average of the magnitude of the real part of acoustic velocity, defined as:

$$v_{Ac.} = \sqrt{[\mathbb{R}(\tilde{v}_x)]^2 + \left[\mathbb{R}(\tilde{v}_y)\right]^2} \tag{7.3.1}$$

From now on the label acoustic velocity has the definition reported in $eq.$ (7.2.1). Results show that the highest area-averaged acoustic velocity is obtained for the 0.5 mm basket, while significantly lower values are observed for the 0.6 mm and 0.7

mm thicknesses. The surface-averaged acoustic velocity does not have a monotone behaviour with respect to the thickness. This could be explained by the nature of the harmonically excited coupled system: variations in thickness simultaneously affect the mass, stiffness, and acoustic-mechanical coupling between the external metal basket and the porous medium. The transmission of acoustic motion could favor either the metal basket, the porous matrix or the entrapped fluid. Consequently, certain higher thickness values may promote a more efficient transfer of acoustic energy and momentum to the porous medium than smaller ones.

The acoustic streaming velocity exhibits a different behaviour. The highest streaming intensity is obtained for the 0.4 mm basket, whereas the 0.6 mm configuration produces a larger streaming velocity than the 0.5 mm case despite exhibiting an acoustic velocity approximately two times lower. This observation demonstrates that the magnitude of the acoustic field alone is not sufficient to explain the acoustic streaming intensity. This behaviour is consistent with the definition of the streaming body force in $eq.$ (4.8.1). In the present model, acoustic streaming is driven by the divergence of the acoustic Reynolds stress tensor, which depends on the spatial distribution of the acoustic velocity field. The generation of streaming is then influenced not only by the magnitude of the acoustic velocity, but also by its distribution throughout the Biot porous medium.

This interpretation is supported by the acoustic velocity fields obtained at optimal frequencies. The 0.4 mm case shows a highly heterogeneous field characterized by multiple localized regions of elevated velocity. Such distribution generates stronger Reynolds-stress divergences and consequently stronger AS. Consistently with the observations this configuration yields the largest acoustic streaming velocity among all cases.

The basket with 0.5 mm thickness generates the highest average acoustic velocity and the highest acoustic velocity peaks as seen in Figure 7.2, but considerably lower streaming velocity. Compared with the 0.4 mm case, the acoustic field appears to be more spatially distributed and less localized. Although the acoustic amplitude is larger, the resulting streaming intensity is reduced, indicating that increased acoustic velocity does not directly translate into enhanced acoustic streaming velocity.

Particularly interesting is the behaviour of the 0.6 mm configuration. Despite a substantial reduction in acoustic velocity with respect to the basket of 0.5 mm thickness, the surface-averaged streaming velocity increases from $2.32 \cdot 10^{-3}$ m/s to $2.88 \cdot 10^{-3}$ m/s. The corresponding acoustic field exhibits a more localized structure,

characterized by a double-lobed pattern concentrated around the central region of the domain. The observed acoustic velocity field is consistent with a more efficient generation of the streaming body force. The 0.6 mm case provides a more effective conversion of acoustic motion into streaming flow than the 0.5 mm configuration.

For the 0.7 mm basket thickness, both the acoustic and streaming velocities decrease significantly. The acoustic field becomes more regular and less intense, resulting in the weakest streaming response among the investigated configurations. This behaviour suggests that the increase in basket thickness beyond a certain value progressively reduces the effectiveness of the acoustic excitation in generating streaming within the porous medium.

An interesting observation is that the maximum acoustic streaming velocity consistently develops within the central region of the domain, similarly to the acoustic velocity. This suggests that the central region acts as a preferential zone for acoustic energy and momentum accumulation within the poroelastic medium: momentum contributions originating from different regions appear to interact most effectively in this area, leading to enhanced AS velocities.

For the 0.4 mm, 0.5 mm and 0.6 mm configurations, the streaming velocity is several times larger than the baseline v_{ax} contribution. Consequently, the total velocity is primarily governed by acoustic streaming. A different situation is observed for the 0.7 mm case, where the acoustic streaming velocity becomes comparable to the baseline velocity. In this case, the total velocity is influenced by both contributions.

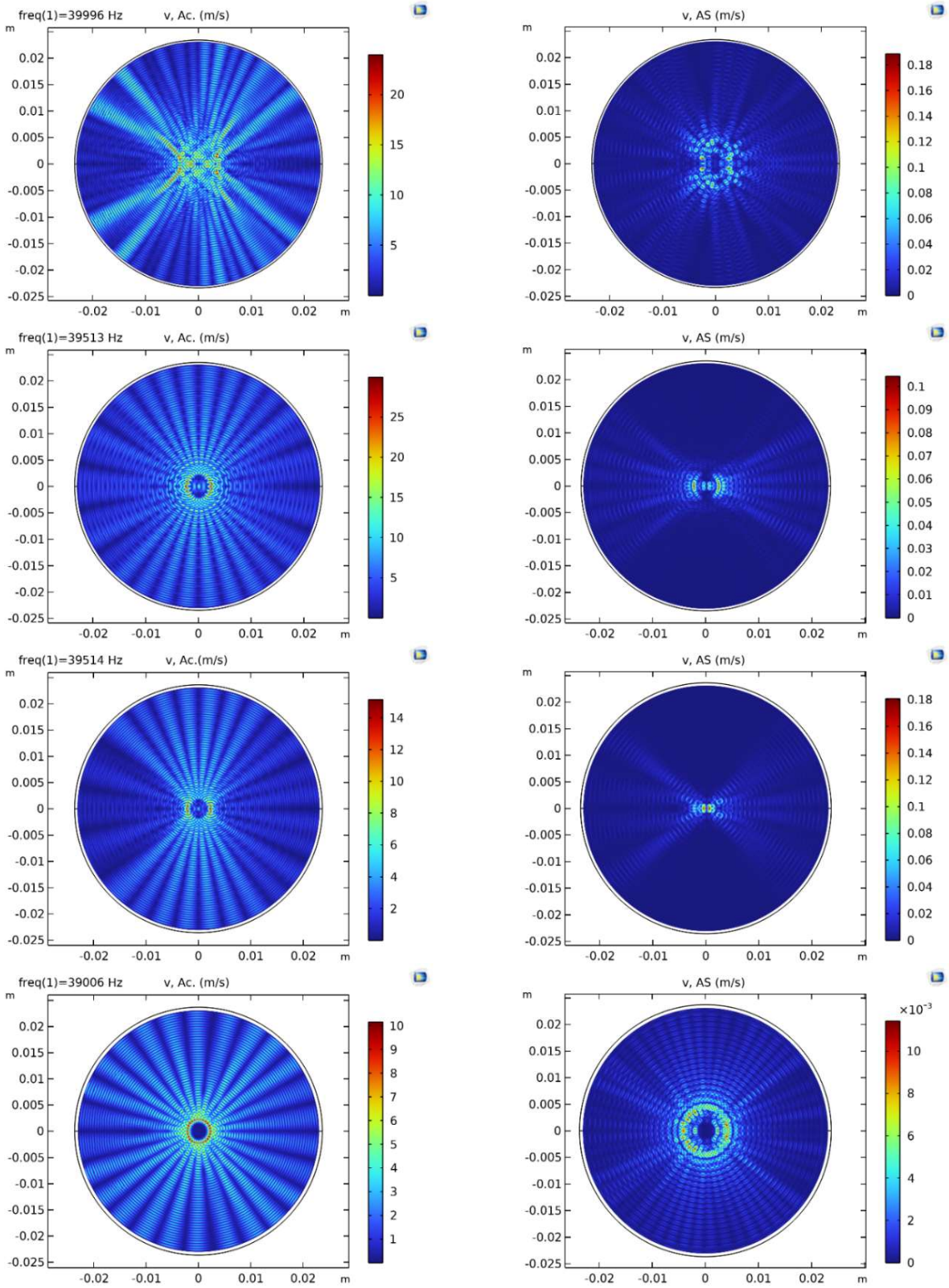

Figure 7.2: From top-to-bottom acoustic velocity and acoustic streaming velocity fields obtained respectively for basket thicknesses of 0.4 mm, 0.5 mm, 0.6 mm and 0.7 mm with applied power of 200 W

7.3.3. Laminar Flow Assumption Validity

The study was then focused on the role of acoustic power in acoustic streaming generation. As reported in figures in Appendix C, the spatial distribution does not vary with applied power: velocities obtained at 200 W are then maximum velocities. Table 7.7 reports the maximum total pore velocities obtained at optimal frequency at maximum power of 200 W, confirming the laminar flow hypothesis made in Subchapter 4.4.2 – (d), with $Re_P < 10$. The maximum total pore velocity is related to the total superficial velocity [74]:

$$v_{max.} = \max\left(\frac{\tau}{\phi} v_{tot.}\right) \tag{7.3.2}$$

Table 7.7: Laminar flow assumption verification, $Re_P < 10$.

$\delta\ [mm]$	$v_{max.}\ [m/s]$	Re_P
0.4	2.471	8.69
0.5	1.368	4.81
0.6	2.475	8.70
0.7	0.151	0.53

7.3.4. Boundary Horn Power Influence on Velocities

The excitation pressure amplitude was imposed according to $eq.(4.7.70)$ which implies that the peak acoustic pressure scales with the square root of the power P. Since the Biot acoustic problem is linear, the acoustic velocity field is expected to scale proportionally to said square root. As expected, this behaviour was confirmed numerically, as the area-averaged acoustic velocity was found to vary linearly with $\sqrt{P}$, with $R^2 = 1$ for all investigated configurations, as shown in Figure 7.3.

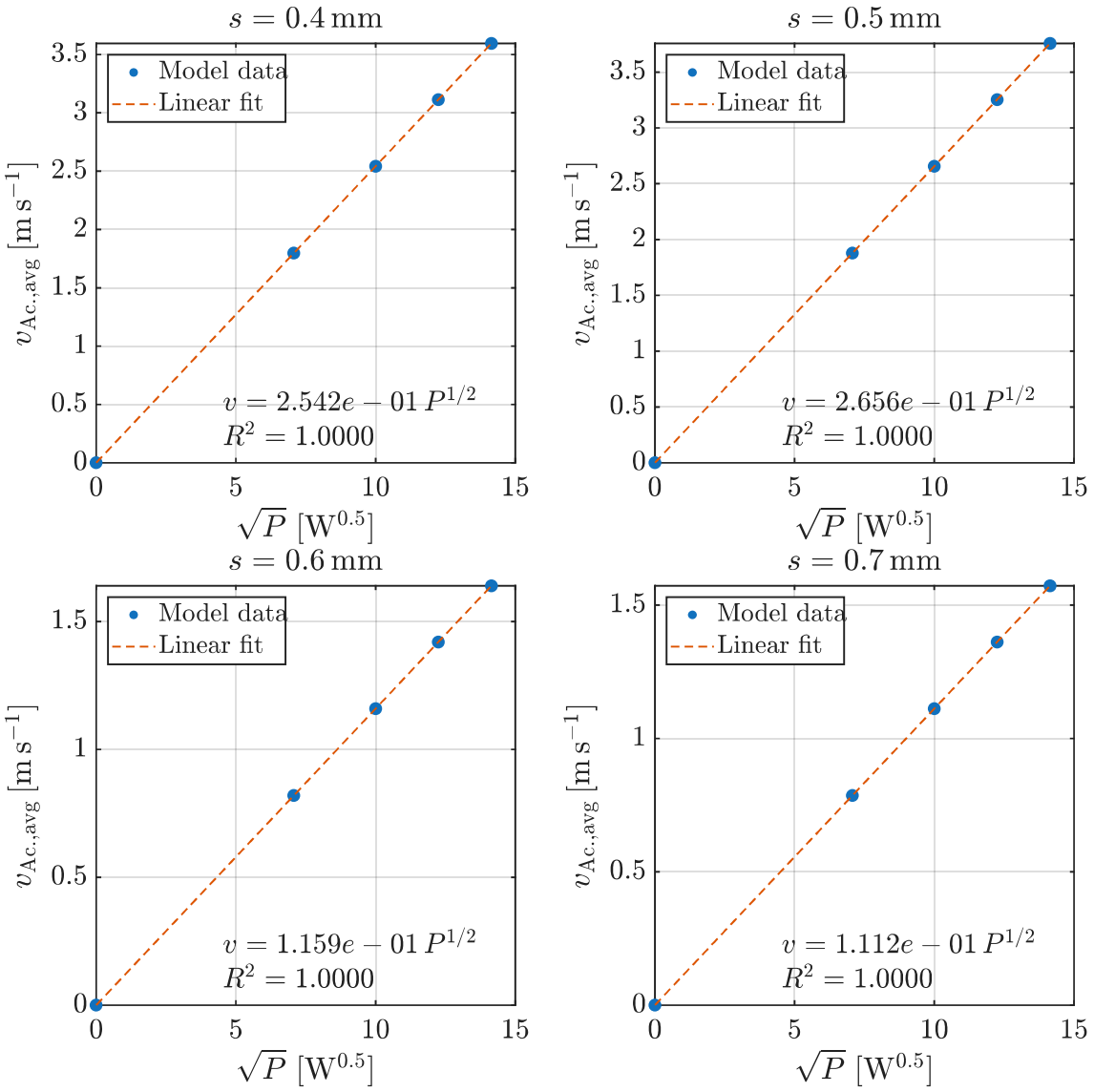

Figure 7.3: Linear regressions for surface averaged acoustic velocity magnitude vs. horn boundary power, showing the correct expected behaviour for all the four configurations

Streaming velocity has a different behaviour than acoustic velocity. Because the acoustic Reynolds stress tensor depends quadratically on the acoustic velocity due to the dyadic definition in *eq.* (4.8.1), the resulting streaming body force scales linearly with the applied power. Due to the linear nature of the Brinkman equations, the acoustic streaming velocity was also found to vary linearly with power. As expected, all linear regressions show $R^2 = 1$ once again, as shown in Figure 7.4.

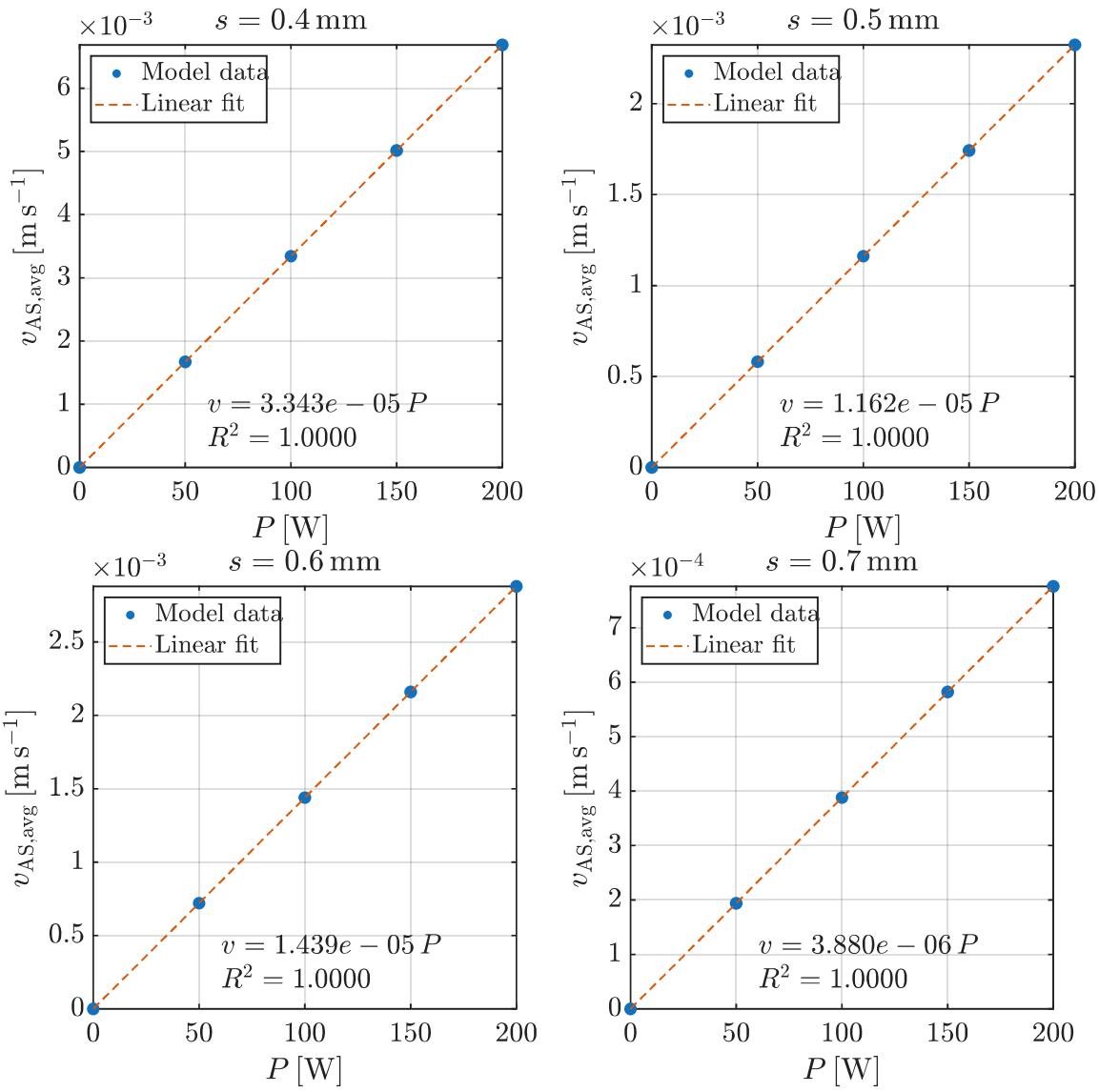

Figure 7.4: Linear regressions for surface averaged AS velocity vs. horn boundary power, showing the correct expected behaviour for all the four configurations

Lastly, total velocity does not show a direct linear correlation with applied power even if it is related to AS velocity due to its definition in *eq.* (4.9.1). This can be clearly seen at 0.7 mm thickness: acoustic streaming velocity is in the same order of axial velocity so neither of them dominates. In the other three cases AS velocity predominates on axial velocity, making the relation quasi-linear.

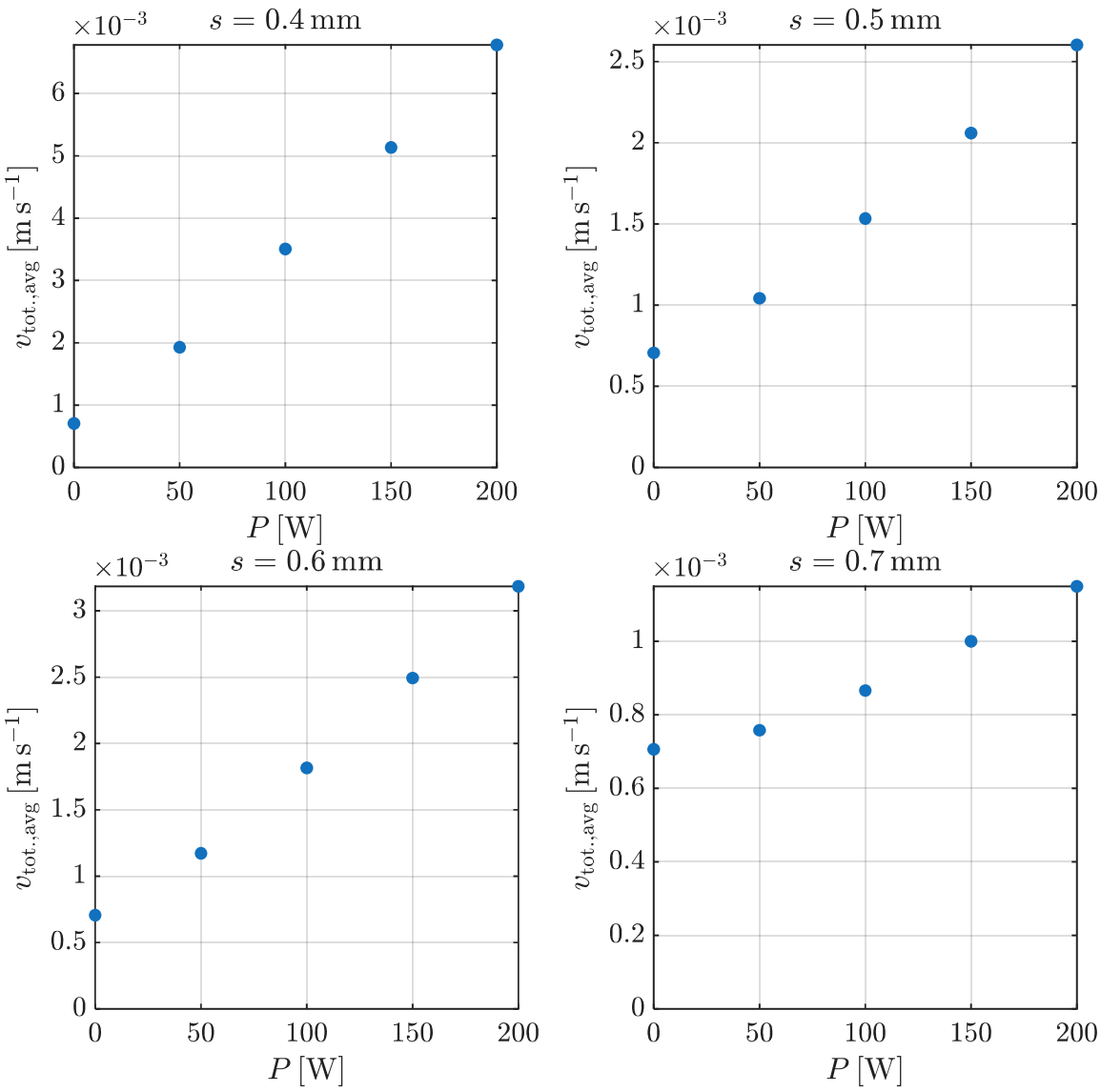

Figure 7.5: Area-averaged total velocity nonlinear relation with applied power

7.4. Ultrasound-Assisted Extraction of Espresso Coffee

As expressed by the mass transfer correlations in *eq.* (4.6.11), total superficial velocity affects the net solute transport from the solids surface to the fluid bulk: the higher the velocity the better the transport. Resulting surface averaged total velocities are used inside the extraction model to determine the new external transport coefficients under ultrasonic effect. The resulting caffeine concentration in cup is then used as indicator and confronted with the baseline case presented in Subchapter 7.1. UAE allows better extraction performance, i.e. higher solutes concentrations in cup, maintaining the same brew ratio, coffee quantity and cup

volume, as axial velocity stays unaffected by ultrasound. Extraction percentage enhancement, determined with *eq*. (4.9.3) is reported in the following Table 7.8.

Table 7.8: Caffeine extraction percentage enhancement obtained at the tested thicknesses and powers

	$\delta = 0.4\ mm$	$\delta = 0.5\ mm$	$\delta = 0.6\ mm$	$\delta = 0.7\ mm$
$P = 0\ W$	0 %	0 %	0 %	0 %
$P = 50\ W$	12.90 %	5.91 %	7.46 %	1.18 %
$P = 100\ W$	17.55 %	10.60 %	12.33 %	3,26 %
$P = 150\ W$	19.78 %	13.50 %	15.11 %	5.35 %
$P = 200\ W$	21.17 %	15.45 %	16.91 %	7.21 %

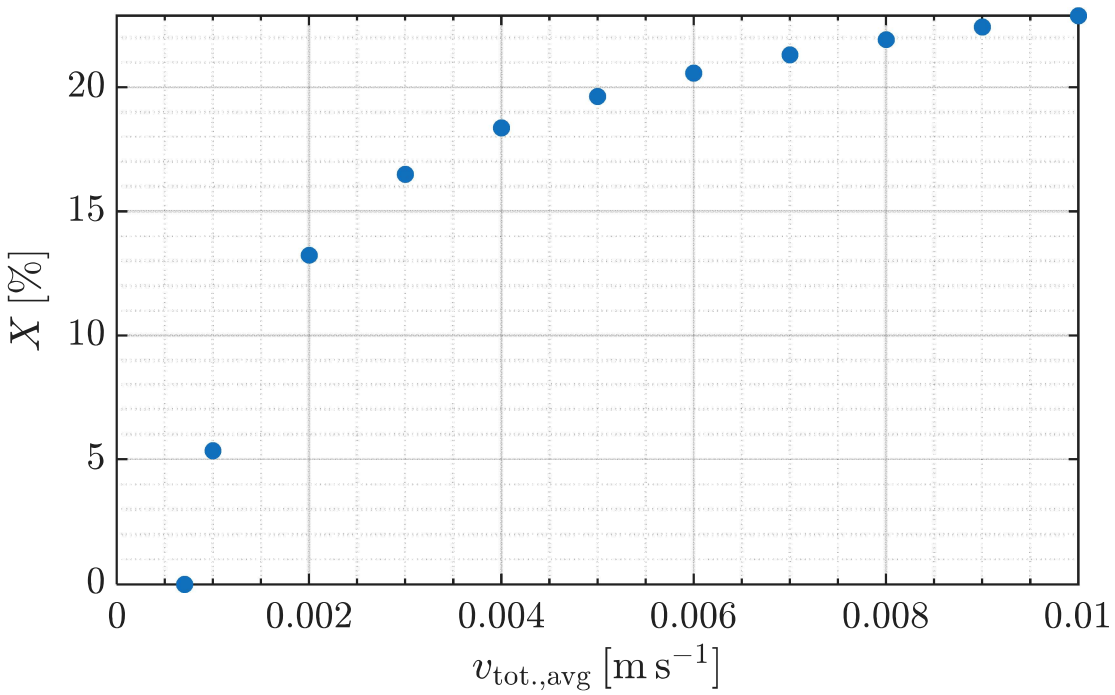

Figure 7.9: Extraction percentage enhancement as function of the surface-averaged total velocity.

Extraction enhancement tends to slow down as higher AS velocity is generated in the extraction liquid, as shown in Figure 7.9. This is due to the nature of the system itself: the more the solute extraction, the less the driving force. A higher initial extraction peak is mainly driven by fine particles, which are subsequently exhausted more rapidly than in the baseline case, resulting in a faster decline in

extraction performance. At the same time, an enhancement of extraction is also observed in the coarse fraction, indicating an overall intensification of the process, consistent with the extraction mechanism.

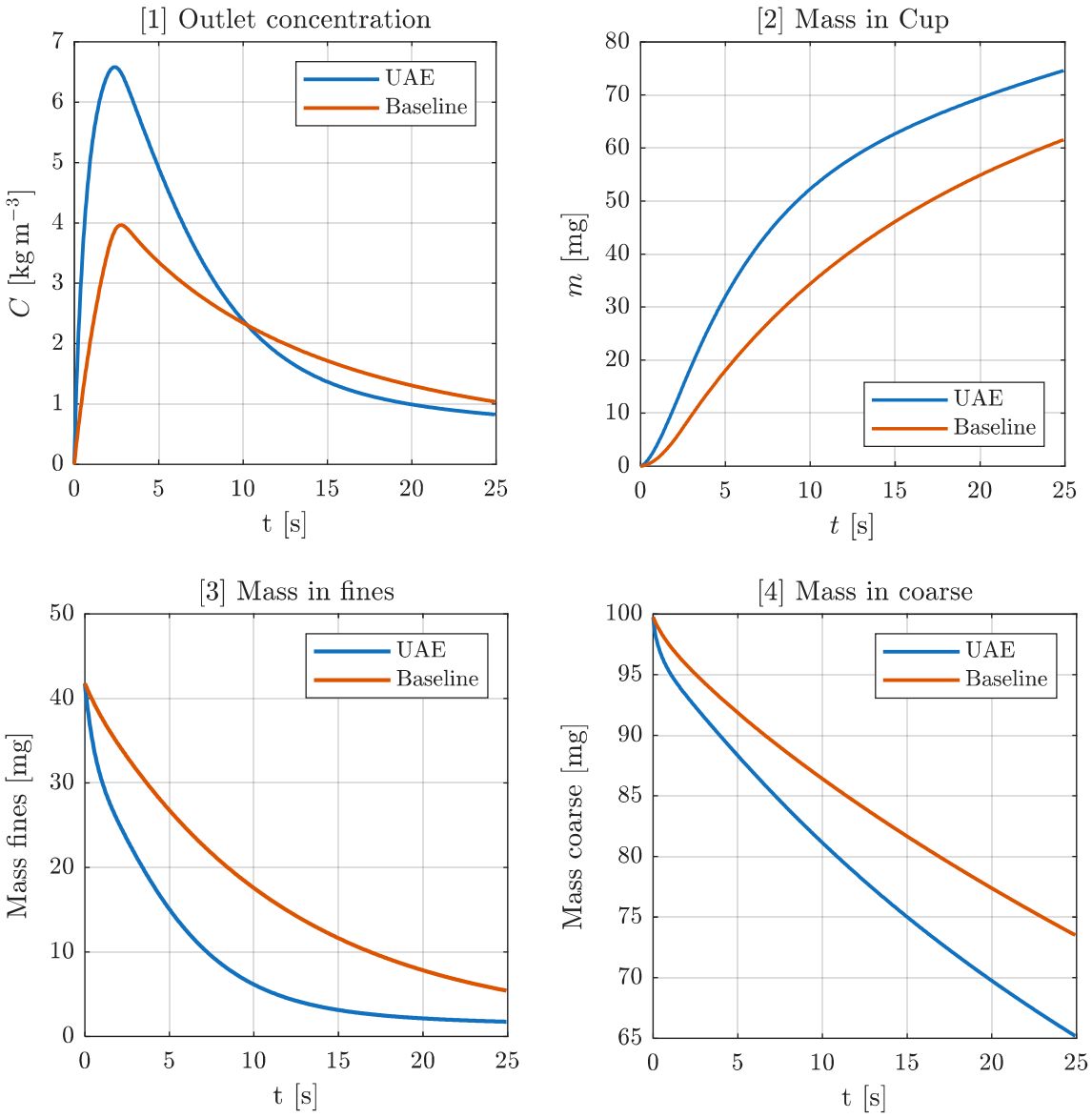

Figure 7.10: Comparison between baseline case and best-scenario (0.4 mm thickness, 200 W of power) case for [1] outlet water caffeine concentration [2] cumulative mass of caffeine in cup [3] remaining caffeine mass in fine particles [4] remaining caffeine mass in coarse particles.

Figure 7.10 is used to visually compare the baseline case and the best-scenario UAE case obtained with a basket thickness of 0.4 mm and an applied power of 200 W. Initially extraction rates, i.e. curve slopes are higher for the UAE case. After the 10 s mark an inversion trend in the fines extraction rate can be observed, while coarse particles extraction curves almost reach the same slope by the end of extraction. This

explains why initial extraction is better in the UAE case while the tail is higher for the baseline case. Nonetheless Figure 7.10-[2] is clear: for the sonicated case at the 10 s mark more than 50 mg of caffeine are already present in the cup, the 60 mg target is reached before 15 s, leaving more than 10 s for over-extraction. Compared with Chiu, S. et al. [23] experimental results for espresso-style cold brew extraction at full basket load ($BLP = 100\%$), the obtained results show consistency being in the same order of magnitude. In their study a 100 W of nominal power sonicator connected to a horn was used, obtaining a caffeine extraction enhancement of around 8-10 %, like results reported here for 100 W and lower (mechanical and coupling losses should be accounted for).

8 Conclusion and Future Developments

8.1. Conclusions

The focus of this thesis was the study of espresso coffee extraction enhancement via ultrasound. First, an isothermal extraction model capable of handling different particle sizes was developed through liquid and solids mass balance equations. This would be used to quantify the actual extraction enhancement. Then Biot's poroelasticity theory was adopted to describe the propagation of ultrasound in a porous matrix filled with fluid, for the determination of pore acoustic velocities. Second-order effects from acoustic velocity generate the acoustic streaming body force which, when used in simplified Brinkman equations for fluid flow in porous media, originates the superficial acoustic streaming velocity. Acoustic streaming is finally used to determine the new, enhanced external mass transfer coefficient to be used inside of the extraction model to then make comparisons and determine extraction enhancement. A parametric study is finally conducted, first identifying the frequencies that maximize the total velocity in the range of 20-40 kHz and then looking at the effect of basket thickness and applied power on acoustic streaming and consequently extraction performance.

Variation in applied power shows the most predictable results: due to the nature of the equations used throughout this work, acoustic streaming velocity scales linearly with the boundary horn power while acoustic velocity scales linearly with the square root of said power. These are direct consequences of the simplification of harmonic plane wave at the border, where $p_{peak} \propto \sqrt{P}$. Interestingly, the spatial distribution of acoustic velocity and consequently the one of acoustic streaming velocity does not depend on the applied power, allowing for an independent study on basket thicknesses and the spatial patterns generated.

The best performance is at 0.4 mm, with a surface averaged acoustic streaming superficial velocity of 0.0067 m/s and extraction enhancement of 21.17 % at 200 W

of boundary power. The best performance is at 0.4 mm of thickness, with a surface averaged acoustic streaming superficial velocity of 0.0067 m/s and extraction enhancement of 21.17 % at 200 W of boundary power. Pore acoustic velocity is the second highest when compared to the other three thicknesses, sitting at 3.59 m/s on average. The spatial distribution is the least uniform, showing multiple localized regions of elevated acoustic velocity. The combination of high acoustic velocity and low uniformity is what should be looked after, generating powerful Reynolds stress and consequently high AS velocities.

The case at 0.5 mm 200 W, despite having the best result in surface averaged pore acoustic velocity (3.76 m/s), falls under both 0.4 mm and 0.6 mm, with an average AS velocity of 0.0023 m/s and an extraction enhancement of 15.45 %. This result is explained by the fact that this geometry shows the most uniform acoustic velocity spatial distribution pattern.

The configuration at 0.6 mm and 200 W is the second best, with an extraction enhancement of 16.91 % with a surface averaged pore acoustic velocity of 1.64 m/s and an AS average velocity of 0.0029 m/s. This really shows the importance of having a favorable acoustic velocity spatial pattern: despite having the second-worst acoustic velocity values, this case is the second best in terms of extraction performance.

Finally, at 0.7 mm 200 W the situation is different, with extraction enhancement spiraling down to just 7.21 %. Low values of area-averaged acoustic velocity and acoustic streaming velocity are obtained, at 1.57 m/s and 0.00078 m/s respectively.

Overall, the results indicate that the influence of the external metal basket thickness cannot be exclusively interpreted in terms of acoustic velocity amplitude. While the 0.5 mm basket produces the highest acoustic velocity, it does not maximize acoustic streaming. Conversely, the 0.6 mm configuration generates stronger streaming despite a significantly lower acoustic velocity. Results shown throughout Chapter 7 demonstrate that the effectiveness of acoustic streaming generation is governed by both the spatial organization of the acoustic field and its amplitude rather than its amplitude alone. The expression of AS is a balance between the acoustic velocity amplitude and its special distribution. Optimization of acoustic streaming in porous media should focus not only on maximizing acoustic velocity i.e. maximizing the energy transfer from the sonicator probe to the entrapped water, but also on identifying field distributions that efficiently generate acoustic streaming.

As shown in Subchapter 7.3, although an increase in pore velocity is essential for enhancing mass transfer, the extraction process exhibits diminishing returns. As the pore velocity increases, the incremental improvement in extraction efficiency progressively decreases, meaning that once the optimal geometric configuration is identified, pushing the applied power over a certain threshold provides minimal results.

8.2. Future Developments

This final section reports what parts of the present work the authors think could be improved and worked on, starting from the extraction model and continuing with the ultrasound transmission model.

The extraction model developed in this thesis adopts a one-dimensional formulation along the axial direction of the bed, neglecting radial concentration gradients and assuming plug flow. A first possible extension of this model is to include axial dispersion by introducing a Péclet-number-dependent term as the dispersion coefficient. It would capture the broadening of the concentration front thanks to flow heterogeneity and channeling, effects described as significant at low superficial velocity (typical of espresso extraction) by Cameron et al. and Foster et al. [44][45]. The transition from a 1D to a full 3D extraction model can be adopted as the second extension. This new configuration would be able to solve the radial heterogeneity issue in both the flow field, including channeling along the basket walls, and the porosity distribution. A third extension can involve the pre-infusion phase. In the present configuration, the bed is considered to have been saturated with pure water from the beginning, as documented in Subchapter 4.2.2-(g). Modelling the wet moving front during the pre-infusion phase would extend the framework's applicability to the entire process, providing a more complete initial condition for the extraction dynamics, while also allowing the modelling of the evolution of swelling-dependent parameters such as bed permeability and pore diameter.

The ultrasound part of the model is probably the one with the most interesting improvement possibilities. From a numerical point of view, in the ultrasonic model, the most immediate improvement is the introduction of a second, coarser mesh that solves the Brinkman equations separately from the finer mesh used to solve the Biot poroelastic theory. The introduction of a mesh modelled at a length scale of the streaming problem, typically an order of magnitude coarser, would reduce the memory usage and computational time of the sub-problem, without sacrificing accuracy. A second, essential direction for future developments is the modelling of the ultrasonic probe and horn geometry, rather than applying a uniform boundary

pressure condition to the basket wall determined under harmonic plane wave assumption. The mechanics of the contact between the horn and the basket, together with the acoustic impedance mismatch at each interface of the transmission chain, sonicator, horn and basket wall, introduce frequency-dependent power losses that the actual formulation doesn't include. Characterising these losses would allow to compare, with precision, the acoustic power emitted against the nominal power of the sonicator. The natural consequence of the horn geometry modelling would be the transition from the 2D to the 3D acoustic model, because the horn design could be covering the basket side not uniformly. However, a fully coupled time-domain 3D model of the coupled porelastic-streaming extraction problem would be computationally too heavy to meet the minimum mesh requirements for the Biot P2 slow-wave. Considering a bed height of 1 cm and an average mesh size of 1.2×10^{-5} m, the additional necessary layers would be around 800-850, reaching a maximum memory usage of around 100 TB of RAM, which would be inaccessible. The challenge then becomes the translation of an accurate 3D model for the sonicator-horn-basket coupling in 2D terms. Finally, a more systematic analysis of the system basket-bed's resonance behaviour should be conducted. In Chapter 7, the parametric study reveals that the relationship between the entering frequency and the streaming velocity is non-monotonic and dependent on the basket thickness, indicating the presence of structural and acoustic resonances whose frequencies vary with the bed properties. Understanding if and how mechanical resonance is linked with actual extraction performance enhancement through an accurate resonance study (e.g. eigenfrequency study) would allow for easier identification of optimal working frequencies.

Lastly, attention must be paid to the fact that the sonicated system discussed during this work is producing a cup with different characteristics than the un-sonicated case. Future studies should focus on geometries and parameters that allow extraction of an identical brew, with the objective of reducing the coffee usage.

Bibliography

[1] Córdoba, N., Pataquiva, L., Osorio, C., Moreno, F. L. M., & Ruiz, R. Y. (2019). Effect of grinding, extraction time and type of coffee on the physicochemical and flavour characteristics of cold brew coffee. Scientific Reports, 9, 8440. https://doi.org/10.1038/s41598-019-44886-w

[2] International Coffee Organization (ICO). (2023). Annual Review 2022–23: Coffee Report and Outlook. ICO, London. https://www.ico.org/

[3] Illy, A., & Viani, R. (Eds.). (2005). Espresso Coffee: The Science of Quality (2nd ed.). Elsevier Academic Press. ISBN: 978-0-12-369370-5.

[4] Moroney, K. M., Lee, W. T., O'Brien, S. B. G., Suijver, F., & Marra, J. (2015). Modelling of coffee extraction during brewing using multiscale methods: An experimentally validated model. Chemical Engineering Science, 137, 216–234. https://doi.org/10.1016/j.ces.2015.06.003

[5] Monteiro, M. C., & Farah, A. (2012). Chlorogenic acids in Brazilian Coffea arabica cultivars from various consecutive crops. Food Chemistry, 134(1), 611–614. https://doi.org/10.1016/j.foodchem.2012.02.118

[6] Moroney, K. M., Lee, W. T., O'Brien, S. B. G., Suijver, F., & Marra, J. (2019). Analysing extraction uniformity from porous coffee beds using mathematical modelling and computational fluid dynamics approaches. PLOS ONE, 14(7), e0219906. https://doi.org/10.1371/journal.pone.0219906

[7] Farah, A. (2012). Coffee constituents. In Y.-F. Chu (Ed.), Coffee: Emerging Health Effects and Disease Prevention (pp. 21–58). Wiley-Blackwell. https://doi.org/10.1002/9781119949893.ch2

[8] Fujioka, K., & Shibamoto, T. (2008). Chlorogenic acid and caffeine contents in various commercial brewed coffees. Food Chemistry, 106(1), 217–221. https://doi.org/10.1016/j.foodchem.2007.05.091

[9] Clifford, M. N. (2000). Chlorogenic acids and other cinnamates – nature, occurrence, dietary burden, absorption and metabolism. Journal of the Science of Food and Agriculture, 80(7), 1033–1043. https://doi.org/10.1002/(SICI)1097-0010(20000515)80:7<1033::AID-JSFA595>3.0.CO;2-T

[10] Caporaso, N., Genovese, A., Canela, M. D., Civitella, A., & Sacchi, R. (2014). Neapolitan coffee brew chemical analysis in comparison to espresso, moka and American brews. Food Research International, 61, 152–160. https://doi.org/10.1016/j.foodres.2014.01.020

[11] Semmelroch, P., & Grosch, W. (1996). Studies on character impact odorants of coffee brews. Journal of Agricultural and Food Chemistry, 44(2), 537–543. https://doi.org/10.1021/jf9505988

[12] Drewnowski, A., & Gomez-Carneros, C. (2000). Bitter taste, phytonutrients, and the consumer: a review. American Journal of Clinical Nutrition, 72(6), 1424–1435. https://doi.org/10.1093/ajcn/72.6.1424

[13] Martins, S. I. F. S., Jongen, W. M. F., & van Boekel, M. A. J. S. (2001). A review of Maillard reaction in food and implications to kinetic modelling. Trends in Food Science & Technology, 11(9–10), 364–373. https://doi.org/10.1016/s0924-2244(01)00022-x

[14] Belitz, H.-D., Grosch, W., & Schieberle, P. (2009). Food Chemistry (4th ed., pp. 270–277). Springer. https://doi.org/10.1007/978-3-540-69934-7

[15] Sanz, C., Maeztu, L., Zapelena, M. J., Bello, J., & Cid, C. (2002). Profiles of volatile compounds and sensory analysis of three blends of coffee: influence of different proportions of Arabica and Robusta and influence of roasting coffee with sugar. Journal of the Science of Food and Agriculture, 82(8), 840–847. https://doi.org/10.1002/jsfa.1110

[16] Cussler, E. L. (2009). Diffusion: Mass Transfer in Fluid Systems (3rd ed.). Cambridge University Press.

[17] Baggenstoss, J., Poisson, L., Kaegi, R., Perren, R., & Escher, F. (2008). Coffee roasting and aroma formation: Application of different time-temperature conditions. Journal of Agricultural and Food Chemistry, 56(14), 5836–5846. https://doi.org/10.1021/jf800327j

[18] Schenker, S., Handschin, S., Frey, B., Perren, R., & Escher, F. (2000). Pore structure of coffee beans affected by roasting conditions. Journal of Food Science, 65(3), 452–457. https://doi.org/10.1111/j.1365-2621.2000.tb16026.x

[19] Mo, C., Johnston, R., Navarini, L., Liverani, F. S., & Ellero, M. (2023). Exploring the link between coffee matrix microstructure and flow properties using combined X-ray microtomography and smoothed particle hydrodynamics simulations. Scientific Reports, 13, 15803. https://doi.org/10.1038/s41598-023-42380-y

[20] Chemat, F., Rombaut, N., Sicaire, A.-G., Meullemiestre, A., Fabiano-Tixier, A.-S., & Abert-Vian, M. (2017). Ultrasound assisted extraction of food and natural

products. Mechanisms, techniques, combinations, protocols and applications. A review. Ultrasonics Sonochemistry, 34, 540–560. https://doi.org/10.1016/j.ultsonch.2016.06.035

[21] Shen, L., Pang, S., Zhong, M., Sun, Y., Qayum, A., Liu, Y., Rashid, A., Xu, B., Liang, Q., Ma, H., & Ren, X. (2023). A comprehensive review of ultrasonic assisted extraction (UAE) for bioactive components: Principles, advantages, equipment, and combined technologies. Ultrasonics Sonochemistry, 101, 106646. https://doi.org/10.1016/j.ultsonch.2023.106646

[22] Zhai, X., Yang, M., Zhang, J., Zhang, L., Tian, Y., Li, C., Bao, L., Ma, C., & Abd El-Aty, A. M. (2022). Feasibility of ultrasound-assisted extraction for accelerated cold brew coffee processing. Frontiers in Nutrition, 9, 849811. https://doi.org/10.3389/fnut.2022.849811

[23] Chiu, S. H., Naliyadhara, N., Bucknall, M. P., Thomas, D. S., Smyth, H. E., Nadolny, J. M., Kalantar-Zadeh, K., & Trujillo, F. J. (2024). Coffee brewing sonoreactor for reducing the time of cold brew from several hours to minutes while maintaining sensory attributes. Ultrasonics Sonochemistry, 106. https://doi.org/10.1016/j.ultsonch.2024.106885

[24] Lee, Y., & Lee, K.-G. (2025). Effects of ultrasound treatment on physicochemical, sensory, and structural properties of cold brew coffee. Ultrasonics Sonochemistry, 119, 107401. https://doi.org/10.1016/j.ultsonch.2025.107401

[25] Zamanipoor, M. H., Zare, M., de Vries, J. W., & Bhatt, P. (2020). Brewing coffee? – Ultra-sonication has clear beneficial effects on the extraction of key volatile aroma components and triglycerides. Ultrasonics Sonochemistry, 60, 104796. https://doi.org/10.1016/j.ultsonch.2019.104796

[26] Huamaní-Meléndez, V. J., & Darros-Barbosa, R. (2018). High intensity ultrasound assisted decaffeination process of coffee beans in aqueous medium. Journal of Food Science and Technology, 55(12), 4901–4908. https://doi.org/10.1007/s13197-018-3424-3

[27] Beaudor, M., Vauchel, P., Pradal, D., Aljawish, A., & Phalip, V. (2023). Comparing the efficiency of extracting antioxidant polyphenols from spent coffee grounds using an innovative ultrasound-assisted extraction equipment versus conventional method. Chemical Engineering and Processing – Process Intensification, 188, 109358. https://doi.org/10.1016/j.cep.2023.109358

[28] Pittia, P., Sacchetti, G., Mancini, L., Voltolini, M., Sodini, N., Tromba, G., & Zanini, F. (2011). Evaluation of Microstructural Properties of Coffee Beans by Synchrotron X-Ray Microtomography: A Methodological Approach. Journal of Food Science, 76(2). https://doi.org/10.1111/j.1750-3841.2010.02009.x

[29] Al-Shemmeri, M., Fryer, P., Farr, R., & Lopez-Quiroga, E. (2024). Development of coffee bean porosity and thermophysical properties during roasting. Journal of Food Engineering, 378, 112096. https://doi.org/10.1016/j.jfoodeng.2024.112096

[30] Corrochano, B. R., Melrose, J. R., Bentley, A. C., Fryer, P. J., & Bakalis, S. (2015). A new methodology to estimate the steady-state permeability of roast and ground coffee in packed beds. Journal of Food Engineering, 150, 106–116. https://doi.org/10.1016/j.jfoodeng.2014.11.006

[31] Ellero, M., & Navarini, L. (2019). Mesoscopic modelling and simulation of espresso coffee extraction. Journal of Food Engineering, 263, 181–194. https://doi.org/10.1016/j.jfoodeng.2019.05.038

[32] Smrke, S., Eiermann, A., & Yeretzian, C. (2024). The role of fines in espresso extraction dynamics. Scientific Reports, 14, 5612. https://doi.org/10.1038/s41598-024-55831-x

[33] Vaca Guerra, M., Harshe, Y. M., Fries, L., Rothberg, S., Palzer, S., & Heinrich, S. (2023). Influence of particle size distribution on espresso extraction via packed bed compression. Journal of Food Engineering, 340, 111301. https://doi.org/10.1016/j.jfoodeng.2022.111301

[34] Vaca Guerra, M., Harshe, Y. M., Fries, L., Payan Lozada, J., Atxutegi, A., Palzer, S., & Heinrich, S. (2024). Modelling the extraction of espresso components as dispersed flow through a packed bed. Journal of Food Engineering, 368, 111913. https://doi.org/10.1016/j.jfoodeng.2023.111913

[35] Spiro, M., Toumi, R., & Kandiah, M. (1989). The kinetics and mechanism of caffeine infusion from coffee: the hindrance factor in intra-bean diffusion. Journal of the Science of Food and Agriculture, 46(3), 349–356. https://doi.org/10.1002/jsfa.2740460313

[36] Spiro, M., & Chong, Y.-Y. (1997). The kinetics and mechanism of caffeine infusion from coffee: the temperature variation of the hindrance factor. Journal of the Science of Food and Agriculture, 74(3), 416–420. https://doi.org/10.1002/(SICI)1097-0010(199707)74:3<416::AID-JSFA868>3.0.CO;2-0

[37] Jaganyi, D., Vanmare, J., & Clark, T. (1999). Kinetic study of mineral ion extraction from Kenyan Arabica coffee. Journal of the Science of Food and Agriculture, 79(2), 323–326. https://doi.org/10.1002/(SICI)1097-0010(199902)79:2<323::AID-JSFA201>3.0.CO;2-E

[38] Jaganyi, D., & Madlala, S. P. (2000). Kinetics of coffee infusion: a comparative study on the extraction kinetics of mineral ions and caffeine from several types of medium roasted coffees. Journal of the Science of Food and Agriculture, 80(1), 85–

90. https://doi.org/10.1002/(SICI)1097-0010(20000101)80:1<85::AID-JSFA489>3.0.CO;2-#

[39] Beverly, D., Lopez-Quiroga, E., Farr, R., Melrose, J., Bakalis, S., & Fryer, P. J. (2020). Modelling mass and heat transfer in multiphase coffee aroma extraction. Industrial & Engineering Chemistry Research, 59(24), 11099–11112. https://doi.org/10.1021/acs.iecr.0c01153

[40] Kuhn, M., Lang, S., Bezold, F., Minceva, M., & Briesen, H. (2017). Time-resolved extraction of caffeine and trigonelline from finely ground espresso coffee with varying process parameters. Journal of Food Engineering, 206, 37–47. https://doi.org/10.1016/j.jfoodeng.2017.03.002

[41] Spiro, M., & Selwood, R. M. (1984). The kinetics and mechanism of caffeine infusion from coffee: the effect of particle size. Journal of the Science of Food and Agriculture, 35(8), 915–924. https://doi.org/10.1002/jsfa.2740350817

[42] Zanoni, B., Pagliarini, E., & Peri, C. (1992). Modelling the aqueous extraction of soluble substances from ground roasted coffee. Journal of the Science of Food and Agriculture, 58(2), 275–279. https://doi.org/10.1002/jsfa.2740580217

[43] Espinoza-Pérez, J. D., Vargas, A., Robles-Olvera, V. J., Rodríguez-Jimenes, G. C., & García-Alvarado, M. A. (2007). Mathematical modelling of caffeine kinetic during solid–liquid extraction of coffee beans. Journal of Food Engineering, 81(1), 72–78. https://doi.org/10.1016/j.jfoodeng.2006.10.011

[44] Cameron, M. I., Morisco, D., Hofstetter, D., Uman, E., Wilkinson, J., Kennedy, Z. C., Fontenot, S. A., Lee, W. T., Hendon, C. H., & Foster, J. M. (2020). Systematically improving espresso: Insights from mathematical modelling and experiment. Matter, 2(3), 631–648. https://doi.org/10.1016/j.matt.2019.12.019

[45] Foster, J. M., Lee, W. T., Moroney, K. M., Prjamkov, D., Salamon, M., Smith, A., Petrassem-de-Sousa, J., & Vynnycky, M. (2025). Dynamics of liquid infiltration into an espresso bed using time-resolved micro-computed tomography: insights from experiment and modelling. Physics of Fluids, 37(1), 013383. https://doi.org/10.1063/5.0245167

[46] Dukhan, N., Bagci, O., & Ozdemir, M. (2014). Experimental flow in various porous media and reconciliation of Forchheimer and Ergun relations. Experimental Thermal and Fluid Science, 57, 425–433. https://doi.org/10.1016/j.expthermflusci.2014.06.011

[47] Wadsworth, F. B., Vasseur, J., Zhang, J., Dobson, K. J., Gagné, J., Buckland, H. M., Coumans, J. P., Heap, M. J., Theurel, A., Kendrick, J. E., Lavallée, Y., & Hendon, C. H. (2026). A model for the permeability of coffee pucks validated using X-ray

computed micro-tomography. Royal Society Open Science, 13(4), 252031. https://doi.org/10.1098/rsos.252031

[48] Elsanoose, A., Abobaker, E., Khan, F., Rahman, M. A., Aborig, A., & Butt, S. D. (2022). Characterization of a non-Darcy flow and development of new correlation of non-Darcy coefficient. Energies, 15(20), 7616. https://doi.org/10.3390/en15207616

[49] Gan, F. S., Zhou, J. Q., Wang, L., Li, C., Jiang, X. Y., & Zhu, Y. (2025). Global inertial permeability for non-Darcian flow in porous media with different shape configurations. Journal of Hydrology, 662, 133807. https://doi.org/10.1016/j.jhydrol.2025.133807

[50] Waszkiewicz, R., Bajor, Ł., Merzel, F., Makowski, M. P., Drozd, M., Szymczak, P., & Lisicki, M. (2025). Under pressure: poroelastic regulation of flow in espresso brewing. arXiv:2512.21528. https://doi.org/10.48550/arXiv.2512.21528

[51] Raghavan, R. (2018). Theory for acoustic streaming in soft porous matter and its applications to ultrasound-enhanced convective delivery. Journal of Therapeutic Ultrasound, 6, 6. https://doi.org/10.1186/s40349-018-0114-6

[52] Sieber, A. B., Preso, D. B., & Farhat, M. (2022). Dynamics of cavitation bubbles near granular boundaries. Journal of Fluid Mechanics, 947, A39. https://doi.org/10.1017/jfm.2022.698

[53] Andrews, E. D., Fernández Rivas, D., & Peters, I. R. (2023). Bubble collapse near porous plates. Journal of Fluid Mechanics, 962, A11.

[54] Lingle, T. R. (2011). The Coffee Brewing Handbook: A Systematic Guide to Coffee Preparation (2nd ed.). Specialty Coffee Association of America.

[55] Gloess, A. N., Schönbächler, B., Klopprogge, B., D'Ambrosio, L., Chatelain, K., Bongartz, A., Strittmatter, A., Rast, M., & Yeretzian, C. (2013). Comparison of nine common coffee extraction methods: instrumental and sensory analysis. European Food Research and Technology, 236(4), 607–627. https://doi.org/10.1007/s00217-013-1917-x

[56] Nishiyama, N., & Yokoyama, T. (2017). Permeability of porous media: Role of the critical pore size. *Journal of Geophysical Research: Solid Earth*, *122*(9), 6955–6971. https://doi.org/10.1002/2016JB013793

[57] *Acoustics Module User's Guide*. (2024). www.comsol.com/blogs

[58] *Structural Mechanics Module User's Guide*. (2024). www.comsol.com/blogs

[59] Yan, F., & Han, D.-H. (2011). *Theoretical validation of fluid substitution by Hashin-Shtrikman bounds*. http://library.seg.org/

[60] de Oliveira e Silva, M., Gomes, F. C., & da Rosa, S. D. V. F. (2017). Ultrasonic pulse technique for evaluation of mechanical damage in processed coffee beans. *Semina:Ciencias Agrarias*, *38*(5), 3007–3018. https://doi.org/10.5433/1679-0359.2017v38n5p3007

[61] Tinoco, H. A., Buitrago-Osorio, J., Perdomo-Hurtado, L., Lopez-Guzman, J., Ibarra, C. A., Rincon-Jimenez, A., Ocampo, O., & Berrio, L. v. (2022). Experimental Assessment of the Elastic Properties of Exocarp–Mesocarp and Beans of Coffea arabica L. var. Castillo Using Indentation Tests. *Agriculture (Switzerland)*, *12*(4). https://doi.org/10.3390/agriculture12040502

[62] Uhlířová, T., & Pabst, W. (2020). Poisson's ratio of porous and cellular materials with randomly distributed isometric pores or cells. *Journal of the American Ceramic Society*, *103*(12), 6961–6977. https://doi.org/10.1111/jace.17139

[63] *Porous Media Flow Module User's Guide*. (2024). www.comsol.com/blogs

[64] Orosco, J., & Friend, J. (2022). Modelling fast acoustic streaming: Steady-state and transient flow solutions. *Physical Review E*, *106*(7). https://doi.org/10.1103/PhysRevE.106.045101

[65] Mat-Shayuti, M. S., Tuan Ya, T. M. Y. S., Abdullah, M. Z., Md Yusop, N., Kamarrudin, N., Myo Thant, M. M., & Che Daud, M. F. (2020). Simulations of different power intensity inputs towards pressure, velocity & cavitation in ultrasonic bath reactor. *South African Journal of Chemical Engineering*, *34*, 57–62. https://doi.org/10.1016/j.sajce.2020.06.002

[66] Kowalczuk, P. B., & Drzymala, J. (2016). Physical meaning of the Sauter mean diameter of spherical particulate matter. *Particulate Science and Technology*, *34*(6), 645–647. https://doi.org/10.1080/02726351.2015.1099582

[67] Alopaeus, V. (2000). Mass-transfer calculation methods for transient diffusion within particles. *AIChE Journal*, *46*(12), 2369–2372. https://doi.org/10.1002/aic.690461205

[68] Roman Corrochano, B. (2017). *ADVANCING THE ENGINEERING UNDERSTANDING OF COFFEE EXTRACTION*.

[69] Paglia, U. (2026). *Multi-Scale Modelling of Coffee Extraction: from DEM-LBM Microstructure to 1D Macro-Scale Simulation MASTER DEGREE IN FOOD ENGINEERING*.

[70] Jaganyi, D., Vanmare, J., & Clark, T. (1997). Equilibrium and kinetic study of caffeine and mineral ion extraction from coffee. In *S.Afr.J.Chem* (Vol. 50, Issue 4).

[71] Holmgren, M. (2006). *X STEAM FOR MATLAB*. www.x-eng.com.

[72] ANSYS, Inc. (2026). Granta EduPack (v2021 R1). Materials database. ANSYS.

[73] Silin, D. B., Korneev, V. A., Goloshubin, G. M., & Patzek, T. W. (2004). *A HYDROLOGIC VIEW ON BIOT'S THEORY OF POROELASTICITY*.

[74] Epstein, N. (1989), On tortuosity and the tortuosity factor in flow and diffusion through porous media, Chemical Engineering Science (Vol. 44, Issue 3). https://doi.org/10.1016/0009-2509(89)85053-5

[75] Irvine, T. (2000). *FORMULAS FOR CALCULATING THE SPEED OF SOUND Revision G*.

[76] Bouzidi, Y., & Schmitt, D. R. (2009). Measurement of the speed and attenuation of the Biot slow wave using a large ultrasonic transmitter. *Journal of Geophysical Research: Solid Earth*, *114*(8). https://doi.org/10.1029/2008JB006018

[77] Yao, Y., Yang, K., Zhang, W., & Liu, S. (2014). Parametric study on silica gel regeneration by hot air combined with ultrasonic field based on a semi-theoretic model. *International Journal of Thermal Sciences*, *84*, 86–103. https://doi.org/10.1016/j.ijthermalsci.2014.05.005

[78] Muller, P. B., & Bruus, H. (2015). Theoretical study of time-dependent, ultrasound-induced acoustic streaming in microchannels. *Physical Review E - Statistical, Nonlinear, and Soft Matter Physics*, *92*(6). https://doi.org/10.1103/PhysRevE.92.063018

[79] Kimura, M. (2024). Introduction to Biot's theory of poroelastic wave propagation. In *Acoustical Science and Technology* (Vol. 45, Issue 1, pp. 9–15). Acoustical Society of Japan. https://doi.org/10.1250/ast.e23.39

[80] Merabet, N. H., & Kerboua, K. (2025). Acoustic streaming: modelling and simulation. *Modelling and Simulation of Sono-Processes: Fundamental and Semiempirical Approaches for Ultrasound-Assisted Processes and Sonochemistry*, 59–70. https://doi.org/10.1016/B978-0-443-23651-8.00004-8

[81] Genovese, A., Caporaso, N., & Baiano, A. (2025). The Impact of Brewing Methods on the Quality of a Cup of Coffee. In *Beverages* (Vol. 11, Issue 5). Multidisciplinary Digital Publishing Institute (MDPI). https://doi.org/10.3390/beverages11050125

[82] Waszkiewicz, R., Myck, F., Białas, Ł., Puciata-Mroczynska, M., Dzikowski, M., Szymczak, P., & Lisicki, M. (2026). *Under pressure: poroelastic regulation of flow in espresso brewing*. http://arxiv.org/abs/2512.21528

[83] X-ray Microscopic Examination of Espresso Powder Porosity (2023). Microphotonics. https://www.microphotonics.com/x-ray-microscopic-examination-espresso-powder-porosity/

[84] Giacomini, J., Khamitova, G., Maponi, P., Vittori, S., & Fioretti, L. (2020). Water flow and transport in porous media for in-silico espresso coffee. *International Journal of Multiphase Flow*, *126*. https://doi.org/10.1016/j.ijmultiphaseflow.2020.103252

[85] Guinard, J. X., Frost, S., Batali, M., Cotter, A., Lim, L. X., & Ristenpart, W. D. (2023). A new Coffee Brewing Control Chart relating sensory properties and consumer liking to brew strength, extraction yield, and brew ratio. *Journal of Food Science*, *88*(5), 2168–2177. https://doi.org/10.1111/1750-3841.16531

[86] U.S. Department of Agriculture, Agricultural Research Service. FoodData Central. (1996). https://www.usda.gov/

A Appendix A

1) The trace of a matrix $tr(A)$ is defined as the sum of the elements on its main diagonal:

$$A = \begin{bmatrix} A_{1,1} & \cdots & A_{1,n} \\ \vdots & \ddots & \vdots \\ A_{n,1} & \cdots & A_{n,n} \end{bmatrix}$$

$$tr(A) = A_{1,1} + A_{2,2} + A_{3,3} + \cdots + A_{n,n}$$

2) The divergence of a scalar s multiplied by the identity matrix I is equal to the gradient of the scalar:

$$sI = \begin{bmatrix} s & 0 & 0 \\ 0 & s & 0 \\ 0 & 0 & s \end{bmatrix}$$

$$\nabla \cdot (sI) = \begin{bmatrix} \frac{\partial}{\partial x} & \frac{\partial}{\partial y} & \frac{\partial}{\partial z} \end{bmatrix} \begin{bmatrix} s & 0 & 0 \\ 0 & s & 0 \\ 0 & 0 & s \end{bmatrix} = \begin{bmatrix} \frac{\partial s}{\partial x} \\ \frac{\partial s}{\partial y} \\ \frac{\partial s}{\partial z} \end{bmatrix} = \nabla s$$

3) The stress tensor can be expressed in index notation:

$$\varepsilon_{ij} = \left(\frac{\partial u_i}{\partial x_j} + \frac{\partial u_j}{\partial x_i} \right)$$

The divergence of the stress tensor is:

$$(\nabla \cdot \varepsilon)_i = \frac{\partial \varepsilon_{ij}}{\partial x_j} = \frac{1}{2} \frac{\partial}{\partial x_j} \left(\frac{\partial u_i}{\partial x_j} + \frac{\partial u_j}{\partial x_i} \right) = \frac{1}{2} \left(\frac{\partial^2 u_i}{\partial x_j^2} + \frac{\partial^2 u_i}{\partial x_j \partial x_i} \right)$$

$$\frac{\partial^2 u_i}{\partial x_j^2} = (\nabla^2 u)_i \qquad \frac{\partial^2 u_i}{\partial x_j \partial x_i} = [\nabla(\nabla \cdot u)]_i$$

$$\nabla \cdot \varepsilon = \frac{1}{2}(\nabla^2 u + \nabla(\nabla \cdot u))$$

4) The trace operator is the sum of the elements on the main diagonal of a matrix. By looking at the definition of the deformation tensor, its trace equals the divergence of the displacement vector field:

$$\varepsilon = \begin{bmatrix} \frac{\partial u_x}{\partial x} & \frac{1}{2}\left(\frac{\partial u_x}{\partial y} + \frac{\partial u_y}{\partial x}\right) & \cdots \\ \cdots & \frac{\partial u_y}{\partial y} & \cdots \\ \cdots & \cdots & \frac{\partial u_z}{\partial z} \end{bmatrix}$$

$$\nabla \cdot u = \frac{\partial u_x}{\partial x} + \frac{\partial u_y}{\partial y} + \frac{\partial u_z}{\partial z}$$

$$tr(\varepsilon) = \nabla \cdot u$$

5) The Laplacian of a vector u is by definition:

$$\nabla^2 u = \nabla(\nabla \cdot u) - \nabla \times (\nabla \times u)$$

6) The real part of a complex number z can be expressed as half of the sum of z and its conjugate z^*:

$$\mathbb{R}(z) = \frac{1}{2}(z + z^*)$$

7) With complex numbers, the conjugate of the product is equal to the product of the conjugates:

$$(AB)^* = A^* B^*$$

8) The conjugate of $e^{i\theta}$ is $e^{-i\theta}$:

$$(e^{i\theta})^* = e^{-i\theta}$$

9) The double dot product between a fourth-order tensor C and a second-order tensor ε in 3D is defined as:

$$(C:\varepsilon)_{ij} = \sum_{k=1}^{3}\sum_{l=1}^{3} C_{ijkl}\varepsilon_{kl}$$

B Appendix B

Appendix B reports the graphs representing the identification of surface-averaged total velocity peaks through parametric analysis. Identified peaks were confirmed by scanning the surrounding ± 1 *Hz* interval.

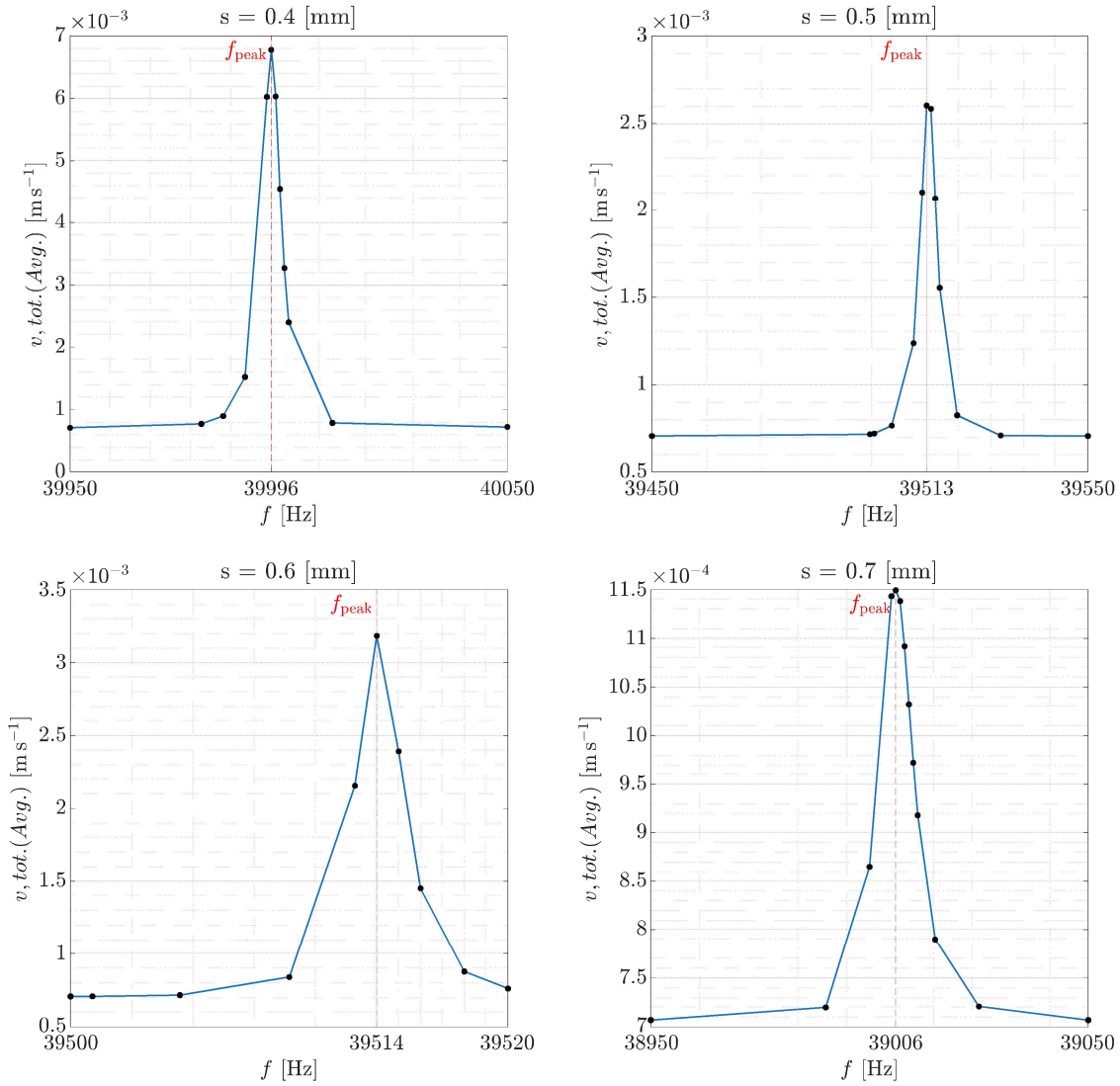

Figure B1: Parametric investigation of surface averaged total velocity as function of frequency for all thicknesses at 200 W of applied power. Resulting narrow peaks are verified by checking ± 1 Hz.

C Appendix C

Appendix C reports all the figures regarding pore acoustic velocity and acoustic streaming superficial velocity fields retrieved from COMSOL Multiphysics®. The spatial distribution of the fields does not vary with applied power.

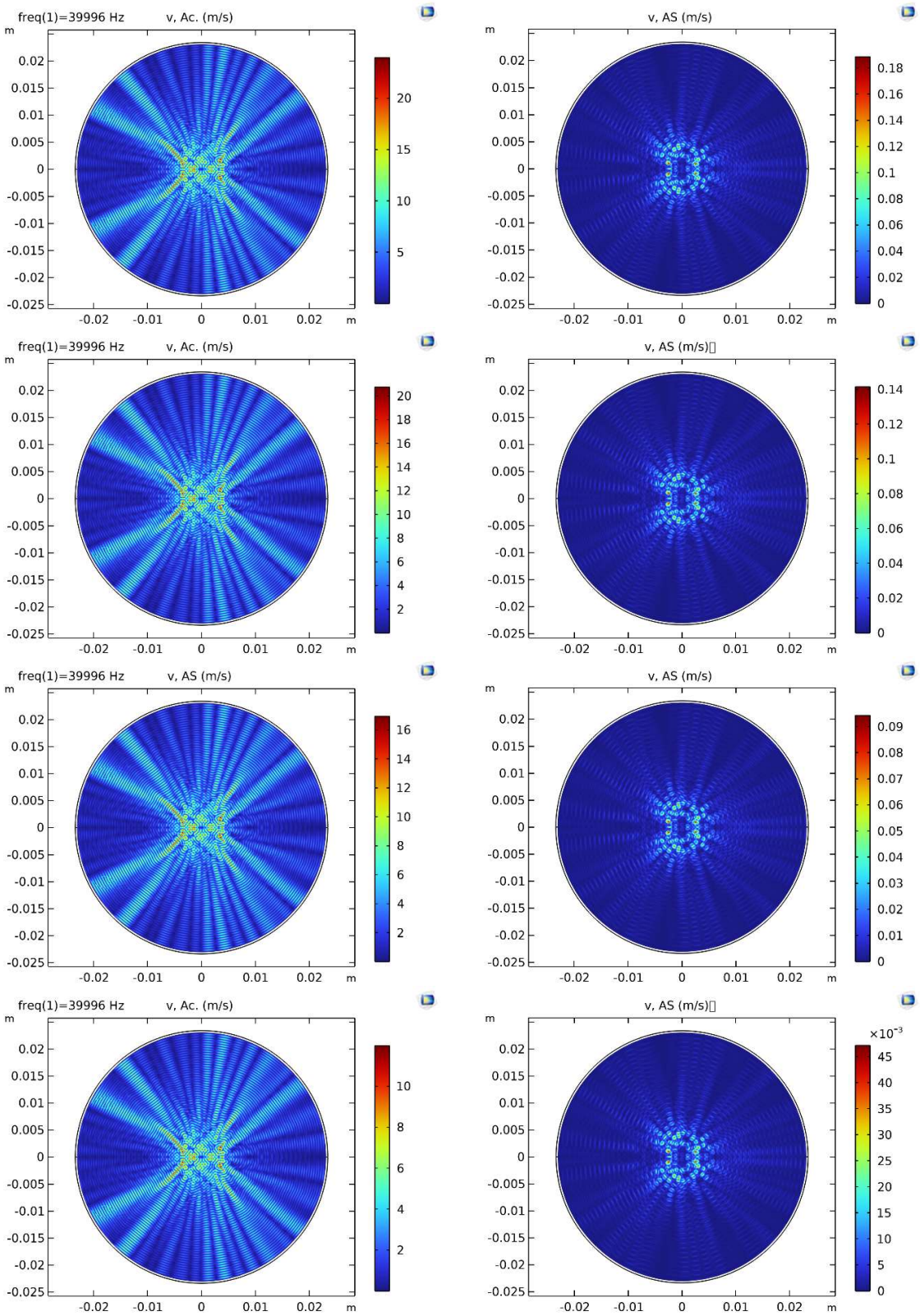

Figure C1: 0.4 mm thickness acoustic velocity and acoustic streaming superficial velocity fields for 200, 150, 100 and 50 W of power respectively (top-to-bottom)

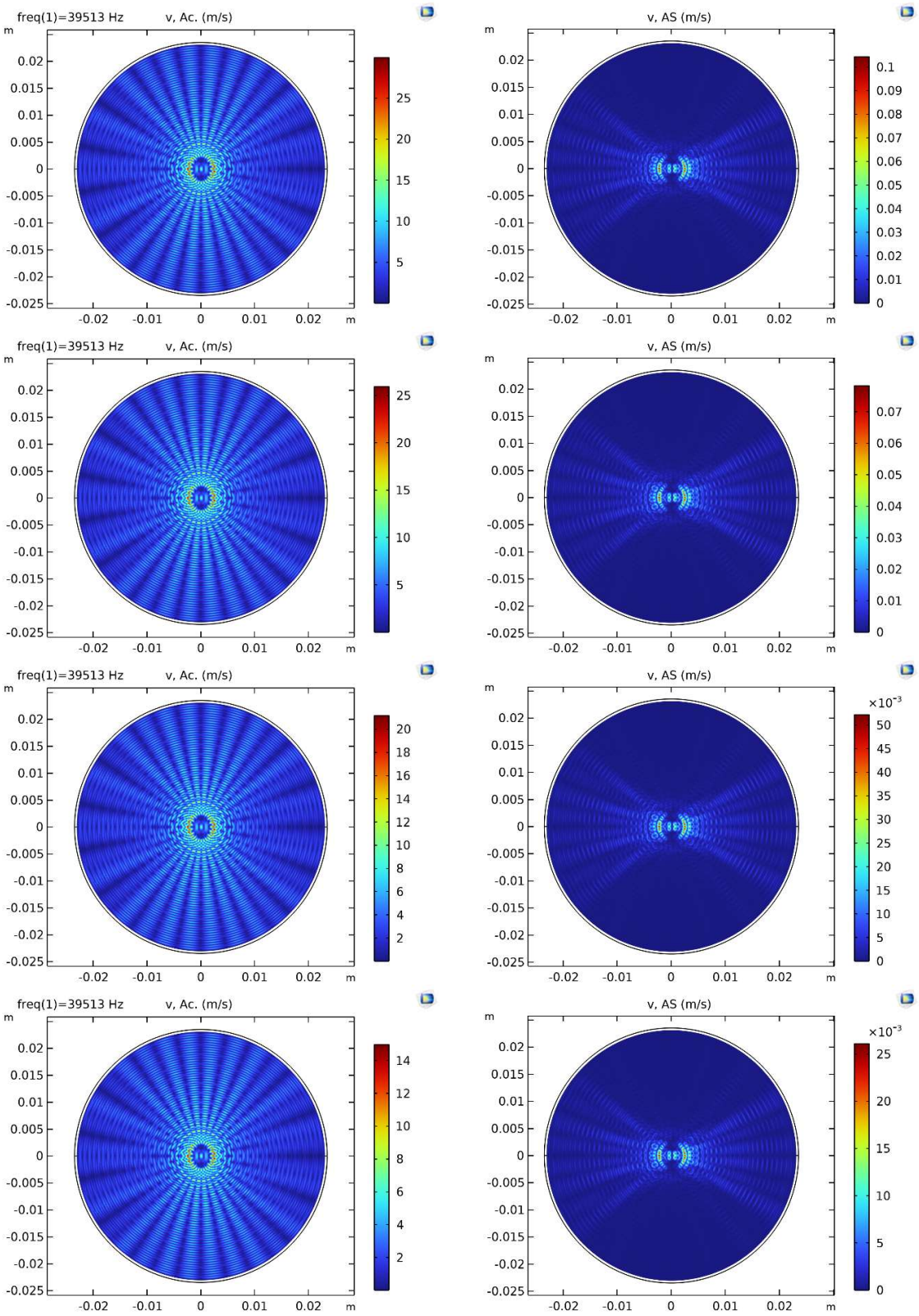

Figure C2: 0.5 mm thickness acoustic velocity and acoustic streaming superficial velocity fields for 200, 150, 100 and 50 W of power respectively (top-to-bottom)

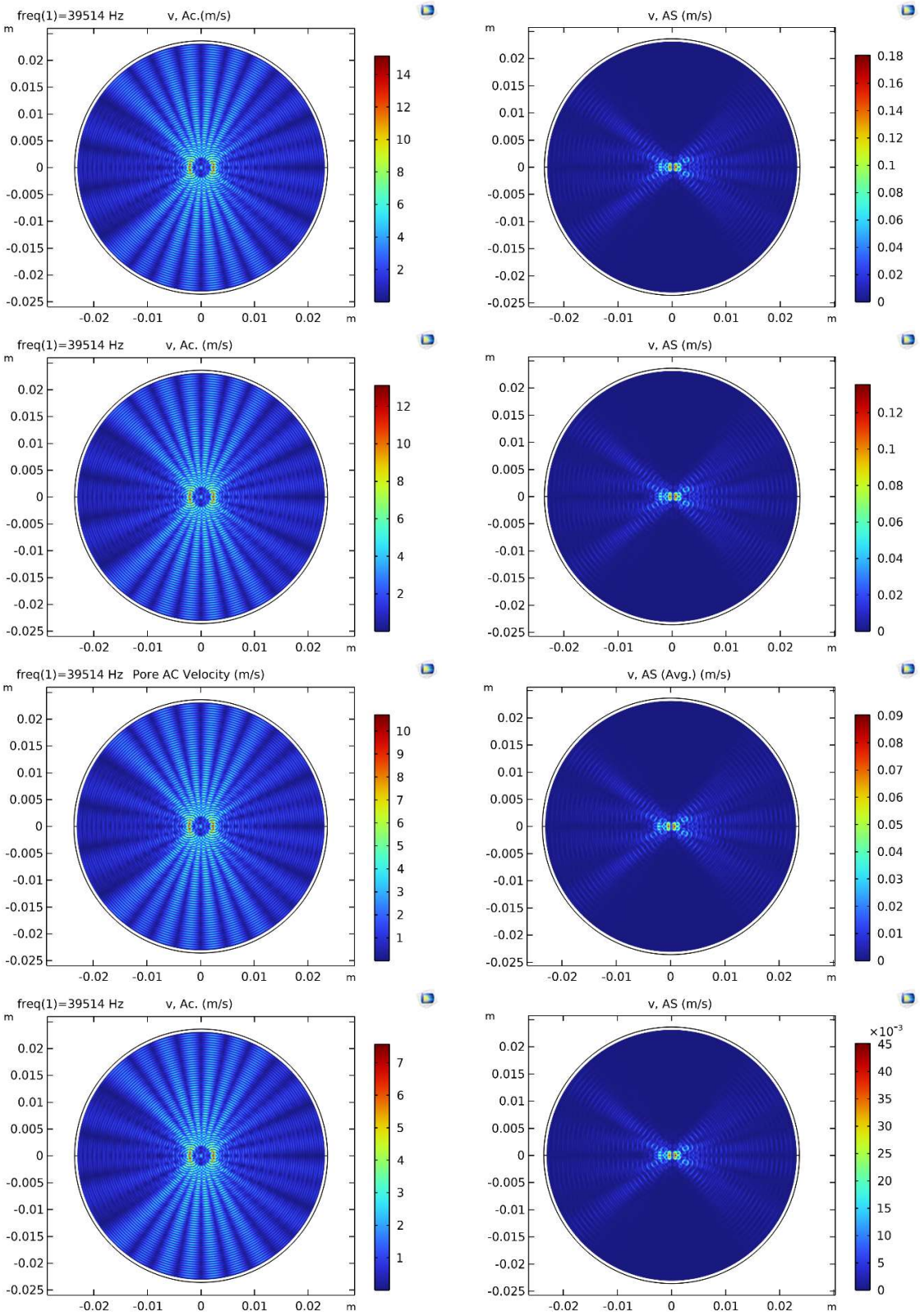

Figure C3: 0.6 mm thickness acoustic velocity and acoustic streaming superficial velocity fields for 200, 150, 100 and 50 W of power respectively (top-to-bottom)

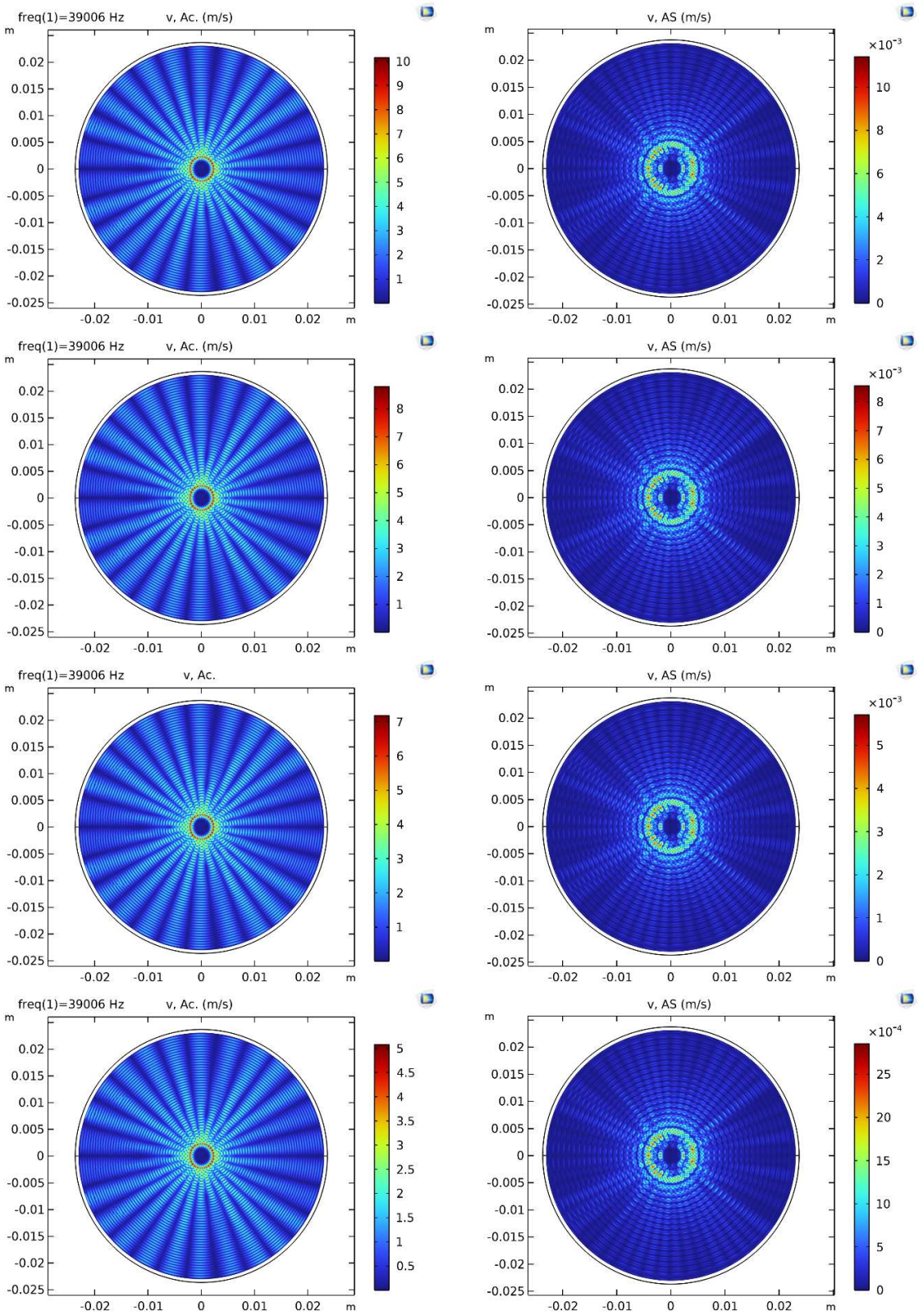

Figure C4: 0.7 mm thickness acoustic velocity and acoustic streaming superficial velocity fields for 200, 150, 100 and 50 W of power respectively (top-to-bottom)

List of symbols

8.3. Latin letters

Variable	Description	SI unit
$\boldsymbol{a}$	Area-to-volume ratio	$1/m$
$\boldsymbol{A_{part}}$	Particle surface area	m^2
$\boldsymbol{A_{sonic}}$	Sonication area	m^2
$\boldsymbol{BR}$	Brew ratio	–
$\boldsymbol{C}$	Liquid bulk concentration	kg/m^3
$\boldsymbol{c}$	Longitudinal Biot poroelastic media sound speed	m/s
$\boldsymbol{C_{cup}}$	Solute concentration in cup	kg/m^3
$\boldsymbol{c_{el}}$	Elastic properties tensor	Pa
$\boldsymbol{c_f}$	Sound speed in fluid	m/s
$\boldsymbol{c_P}$	Longitudinal sound speed	m/s
$\boldsymbol{c_S}$	Shear sound speed	m/s
$\boldsymbol{d}$	Particle diameter	m
$\boldsymbol{\mathcal{D}}$	Molecular diffusivity of solute in fluid	m^2/s
$\boldsymbol{D}$	Basket internal diameter	m
$\boldsymbol{d_{3,2}}$	Sauter's diameter	m
$\boldsymbol{\mathcal{D}_{eff}}$	Effective diffusivity	m^2/s
$\boldsymbol{E}$	Young's modulus	Pa
$\boldsymbol{err}$	Mass conservation percentage error	%
$\mathbb{f}$	Volumetric force	N/m^3
$\boldsymbol{f}$	Frequency	Hz
$\boldsymbol{F_A}$	Force per unit area	N/m^2

$\boldsymbol{Fo}$	Fourier's number	$-$
$\boldsymbol{f_R}$	Viscous transition reference frequency	Hz
$\boldsymbol{g}$	Gravitational acceleration	m/s^2
$\boldsymbol{G}$	Shear modulus	Pa
$\boldsymbol{G_d}$	Dry porous matrix shear modulus	Pa
$\boldsymbol{G_s}$	Solid shear modulus	Pa
$\boldsymbol{h}$	Hindrance factor	$-$
$\boldsymbol{I}$	Identity matrix	$-$
$\boldsymbol{I_{sonic}}$	Sonic intensity	W/m^2
$\boldsymbol{k}$	Permeability	m^2
$\boldsymbol{K}$	Bulk modulus	Pa
$\boldsymbol{k_c}$	Total mass transfer coefficient	m/s
$\boldsymbol{K_d}$	Dry porous matrix bulk modulus	Pa
$\boldsymbol{k_{external}}$	External mass transfer coefficient	m/s
$\boldsymbol{k_{internal}}$	Internal mass transfer coefficient	m/s
$\boldsymbol{K_s}$	Solid bulk modulus	Pa
$\boldsymbol{L}$	Porous bed height	m
$\boldsymbol{m}$	Volumetric partition coefficient	$-$
$\boldsymbol{M}$	Biot's modulus	Pa
$\boldsymbol{m_{coffee}}$	Total coffee mass	kg
$\boldsymbol{m_{cup}}$	Mass of coffee brew	kg
$\boldsymbol{m_{liquid}}$	Mass of solute in entrapped liquid	kg
$\boldsymbol{m_{out}}$	Mass of solute exiting the system	kg
$\boldsymbol{m_{solid}}$	Remaining solute mass in solids	kg
$\boldsymbol{m_{tot}}$	Total mass of solute in the system	kg

$\boldsymbol{p}$	Fluid pressure	Pa
$\boldsymbol{P}$	Applied power	W
$\boldsymbol{p_f}$	Pore fluid pressure	Pa
$\boldsymbol{p_{in}}$	Inlet water head pressure	Pa
$\boldsymbol{p_{out}}$	Outlet water pressure	Pa
$\boldsymbol{p_{peak}}$	Peak acoustic pressure	Pa
$\boldsymbol{q}$	Bulk concentration of solid phase	kg/m^3
$\boldsymbol{Q}$	Volumetric flowrate	m^3/s
$\boldsymbol{Q_m}$	Brinkman equations source/sink term	kg/m^3s
$\boldsymbol{q_{sup}}$	Superficial concentration of solid phase	kg/m^3
$\boldsymbol{r}$	Particle radius	m
$\boldsymbol{r_H}$	Hydraulic pore radius	m
$\boldsymbol{r_{pore}}$	Pore radius	m
$\boldsymbol{S}$	Basket cross-section area	m^2
$\boldsymbol{Sh}$	Sherwood's number	$-$
$\boldsymbol{t}$	Time	s
$\boldsymbol{T_{op}}$	Operative temperature	℃
$\boldsymbol{t_{tot}}$	Total extraction time	s
$\boldsymbol{u}$	Porous matrix displacement	m
$\boldsymbol{u_m}$	Metal basket displacement	m
$\boldsymbol{v}$	Velocity	m/s
$\boldsymbol{\tilde{v}}$	Porous acoustic velocity	m/s
$\boldsymbol{v_1}$	Real part of porous acoustic velocity	m/s
$\boldsymbol{v_{Ac.}}$	Real part of superficial acoustic velocity amplitude	m/s
$\boldsymbol{v_{AS}}$	Superficial acoustic streaming velocity magnitude	m/s

$\boldsymbol{V_{basket}}$	Basket internal volume	m^3
$\boldsymbol{v_{ax}}$	Axial superficial velocity	m/s
$\boldsymbol{v_{max.}}$	Maximum pore fluid velocity	m/s
$\boldsymbol{V_{part}}$	Particle volume	m^3
$\boldsymbol{v_{tot}}$	Total superficial velocity magnitude	m/s
$\boldsymbol{w}$	Relative fluid-porous matrix displacement	m
$\boldsymbol{X}$	Percentage extraction enhancement	%

8.4. Greek letters

Symbol	Description	SI unit
$\boldsymbol{\alpha}$	Rosin-Rammler parameter	$-$
$\boldsymbol{\alpha_B}$	Biot-Willis coefficient	$-$
$\boldsymbol{\beta}$	Rosin-Rammler parameter	$-$
$\boldsymbol{\beta_{coarse}}$	Rosin-Rammler parameter (coarse fraction)	$-$
$\boldsymbol{\Gamma_0}$	Initial mass fraction of solute in solids	kg_{solute}/kg_{bean}
$\boldsymbol{\delta}$	Basket wall thickness	m
$\boldsymbol{\delta_v}$	Viscous boundary layer depth	m
$\boldsymbol{\varepsilon}$	Deformation	$-$
$\boldsymbol{\lambda}$	Lamé parameter	Pa
$\boldsymbol{\lambda_p}$	Empiric permeability parameter	$-$
$\boldsymbol{\lambda_{slow}}$	Slow wave wavelength	m
$\boldsymbol{\mu}$	Shear modulus in Lamé form	Pa
$\boldsymbol{\mu_f}$	Fluid dynamic viscosity	$Pa \cdot s$

$\boldsymbol{\nu_f}$	Fluid kinematic viscosity	m^2/s
$\boldsymbol{\rho_{av}}$	Average density of poroelastic media	kg/m^3
$\boldsymbol{\rho_{bean}}$	Roasted bean density	kg/m^3
$\boldsymbol{\rho_c}$	Biot complex density	kg/m^3
$\boldsymbol{\rho_f}$	Fluid density	kg/m^3
$\boldsymbol{\rho_{intrinsic}}$	Intrinsic coffee density	kg/m^3
$\boldsymbol{\rho_m}$	Metal density	kg/m^3
$\boldsymbol{\sigma}$	Stress tensor	Pa
$\boldsymbol{\sigma_d}$	Dry porous matrix stress tensor	Pa
$\boldsymbol{\sigma_m}$	Metal basket stress tensor	Pa
$\boldsymbol{\tau}$	Bed tortuosity	$-$
$\boldsymbol{\upsilon}$	Poisson's ratio	$-$
$\boldsymbol{\phi}$	Bed porosity	$-$
$\boldsymbol{\phi_{intra}}$	Intra-particle porosity	$-$
$\boldsymbol{\chi_f}$	Fluid compressibility	$1/Pa$
$\boldsymbol{\psi}$	Particle sphericity	$-$
$\boldsymbol{\omega}$	Angular frequency	rad/s